MORB’s… pétrogenèse

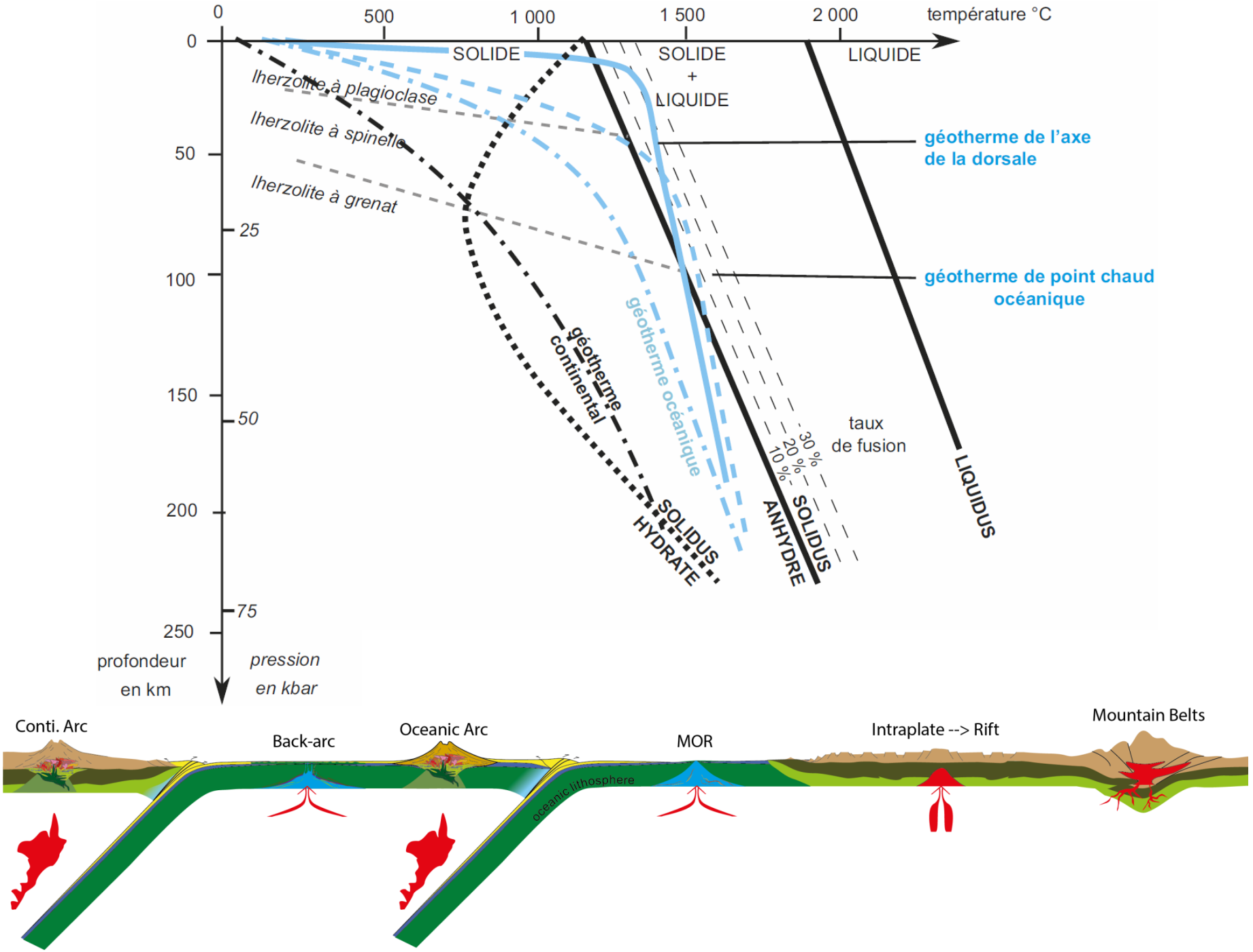
0
500
1 000
1 500
2 000
température °C
0
50
100
150
200
250
25
50
75
profondeur
en km
pression
en kbar
SOLIDE
SOLIDE
+
LIQUIDE
LIQUIDE
lherzolite à plagioclase
lherzolite à spinelle
lherzolite à grenat
géotherme de l'axe
de la dorsale
géotherme de point chaud
océanique
géotherme
continental
géotherme océanique
SOLIDUS
HYDRATE
SOLIDUS
ANHYDRE
LIQUIDUS
taux
de fusion
30 %
20 %
10 %
Conti. Arc
Back-arc
Oceanic Arc
MOR
Intraplate --> Rift
Mountain Belts
oceanic lithosphere

Mid-Ocean Ridge Basalts (MORB)

Les MORB sont la forme dominante du volcanisme actif sur terre:

MORB: 20 km^3/yr
OIB: 2 km^3/yr
Arc: 6 km^3/yr

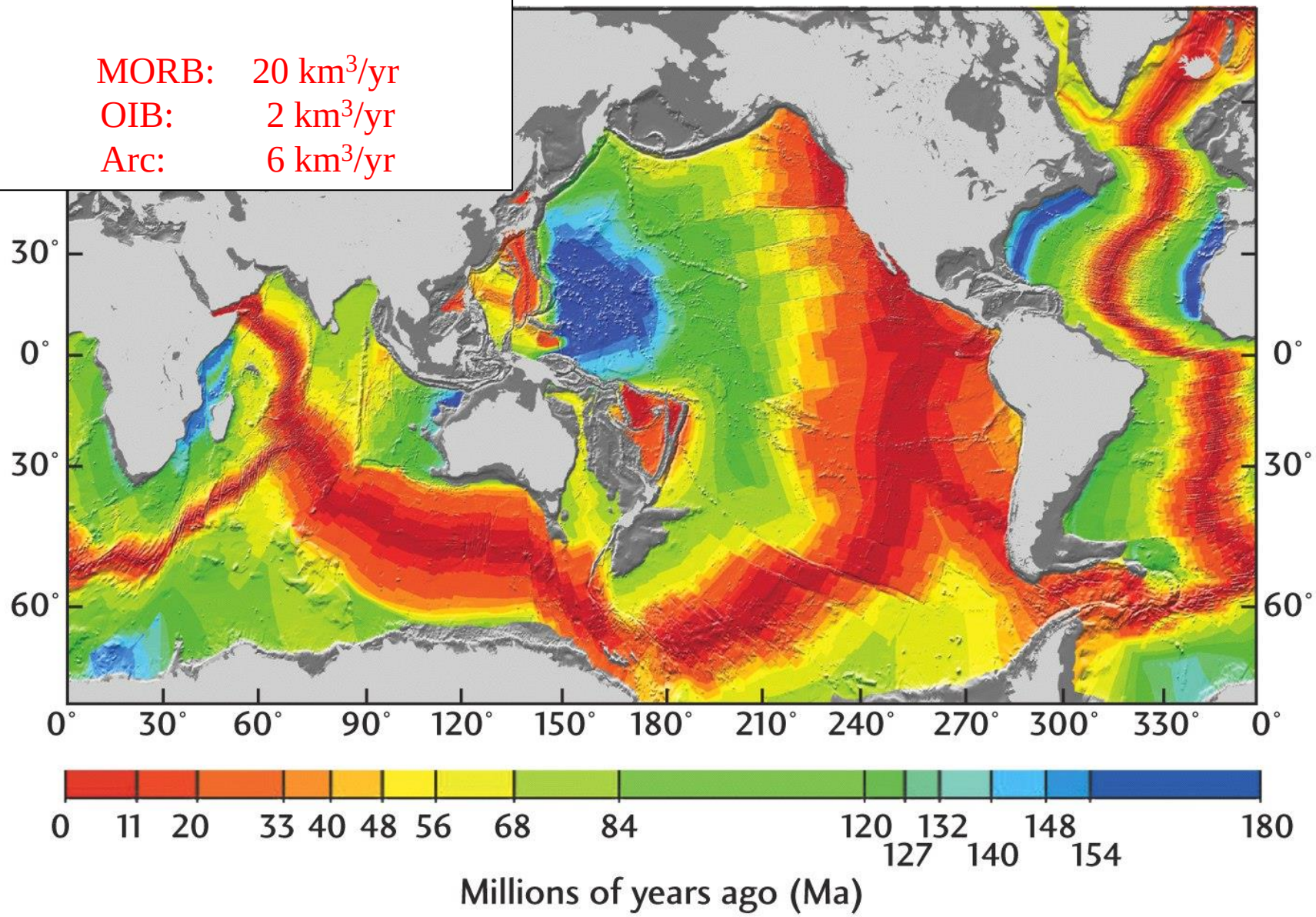

Structure de la Lithosphere Océanique

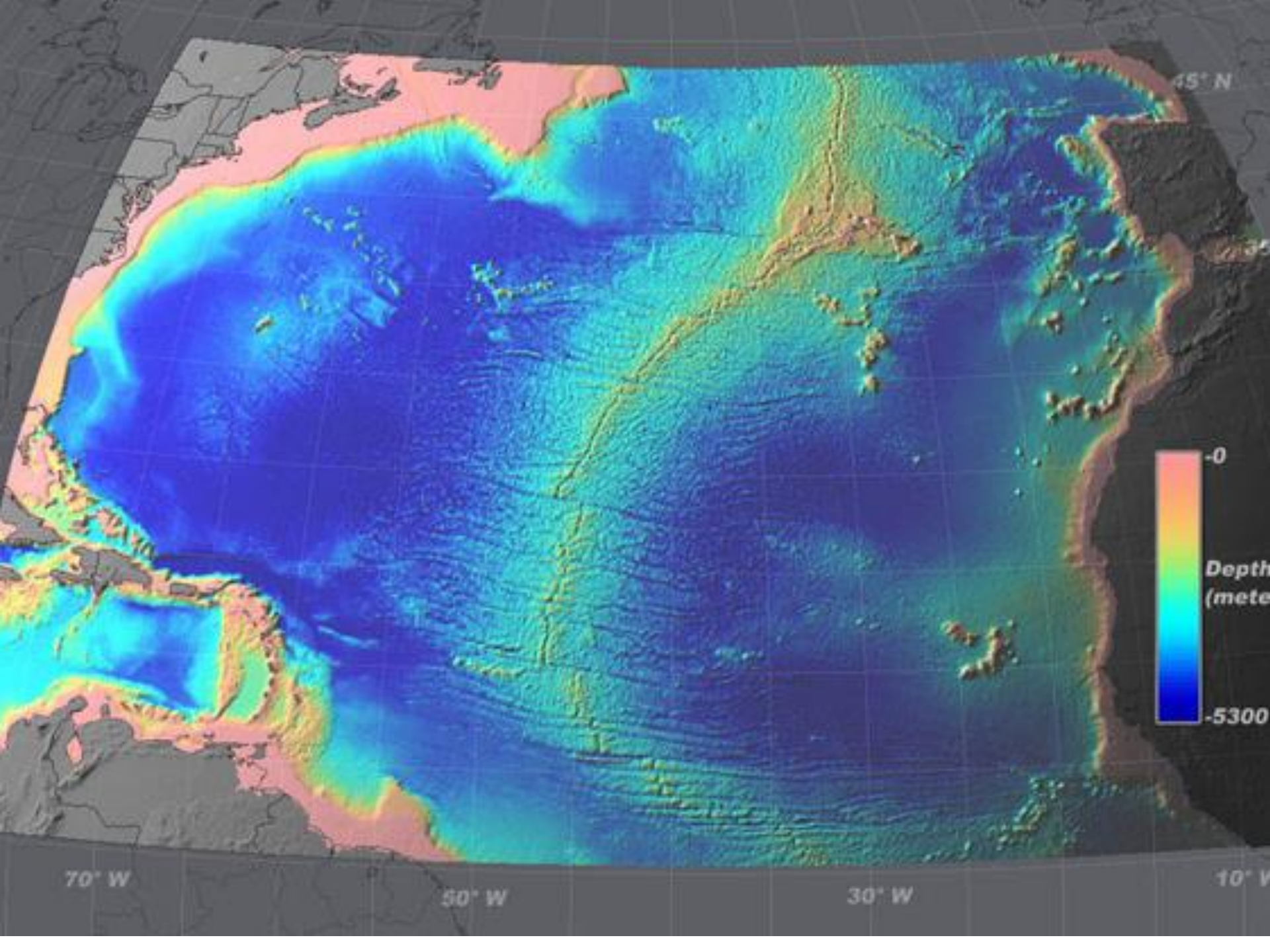
45° N
-0
Depth
(mete
-5300
70° W
50° W
30° W

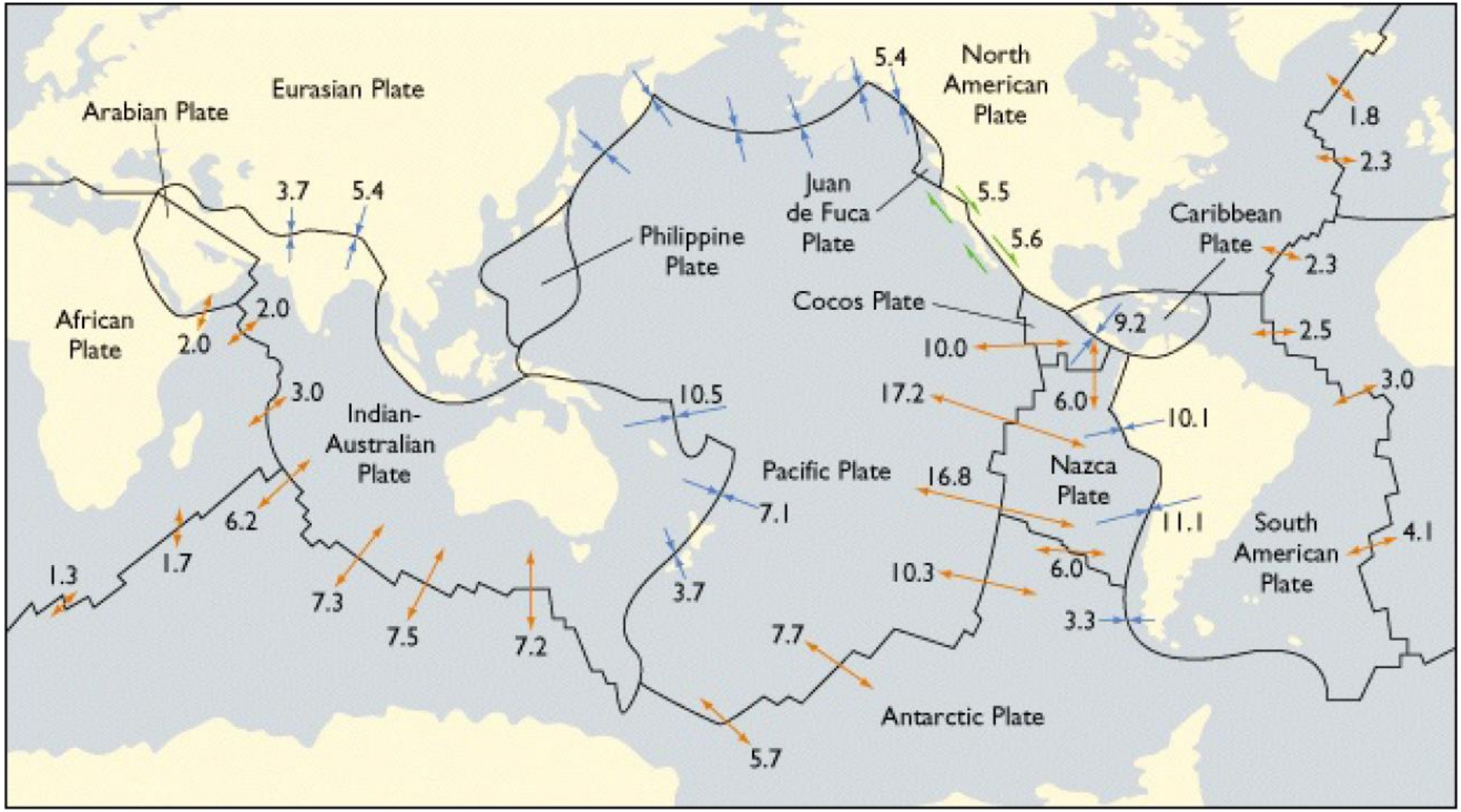
Eurasian Plate
Arabian Plate
North American Plate
Philippine Plate
Juan de Fuca Plate
Caribbean Plate
Cocos Plate
African Plate
Indian-Australian Plate
Pacific Plate
Nazca Plate
South American Plate
Antarctic Plate
5.4
1.8
2.3
3.7
5.4
5.5
5.6
2.3
2.0
2.0
9.2
2.5
10.0
3.0
10.5
17.2
6.0
10.1
16.8
7.1
11.1
4.1
6.2
1.7
1.3
10.3
6.0
7.3
7.5
7.2
3.7
3.3
7.7
5.7

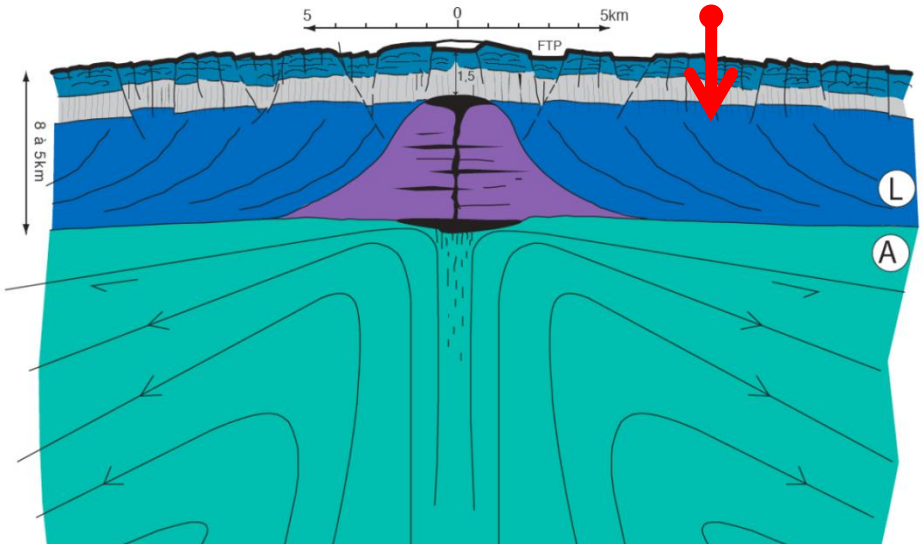

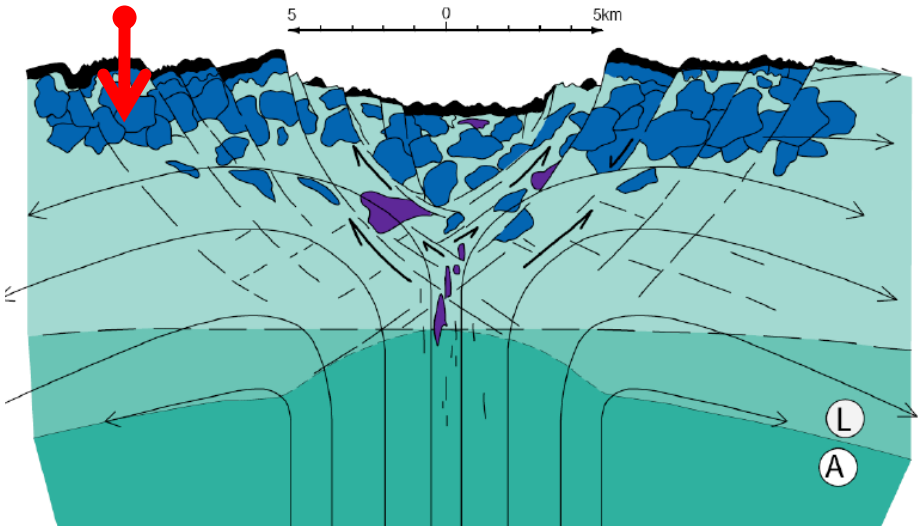

Rapide: Pacifique (Oman)

Croûte continue / Homogène

Chambre magmatique permanente

Lente: Atlantique (Chenaillet)

Croûte discontinue / Hétérogène

Chambres magmatiques intermittentes

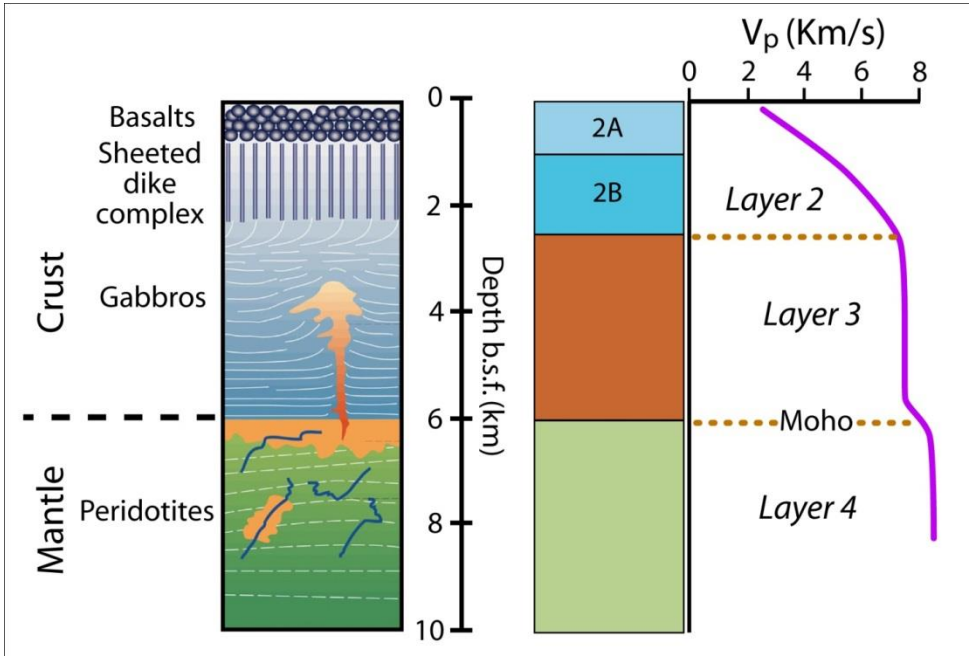

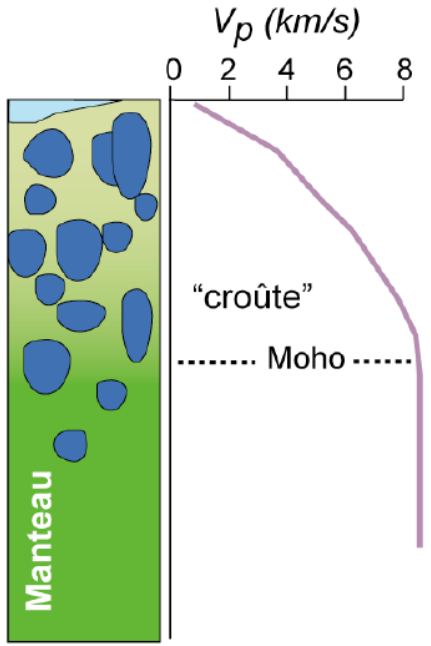

B - Croûte composite

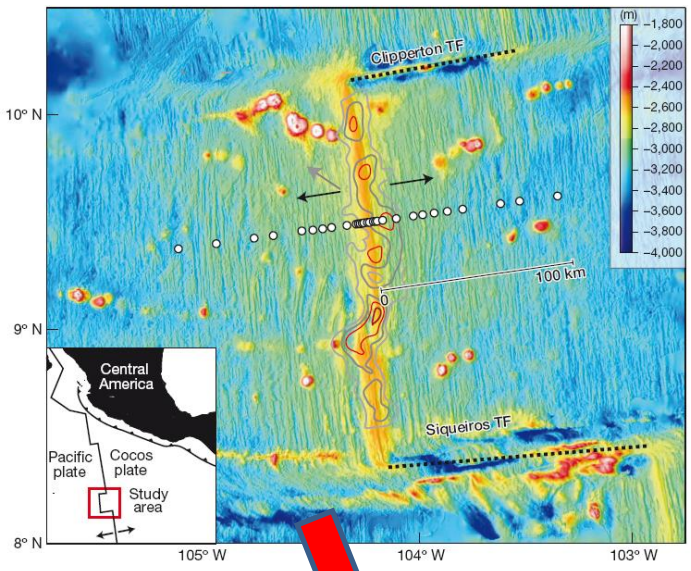

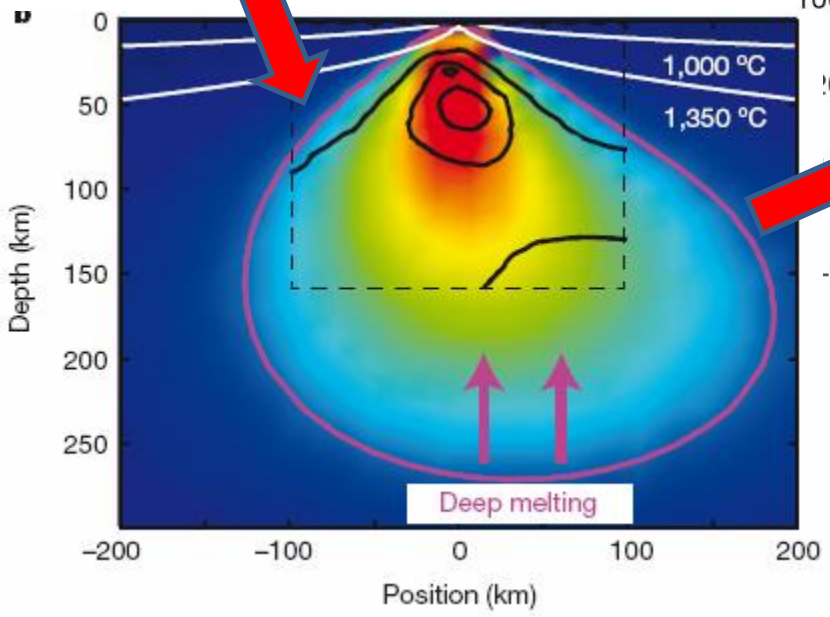

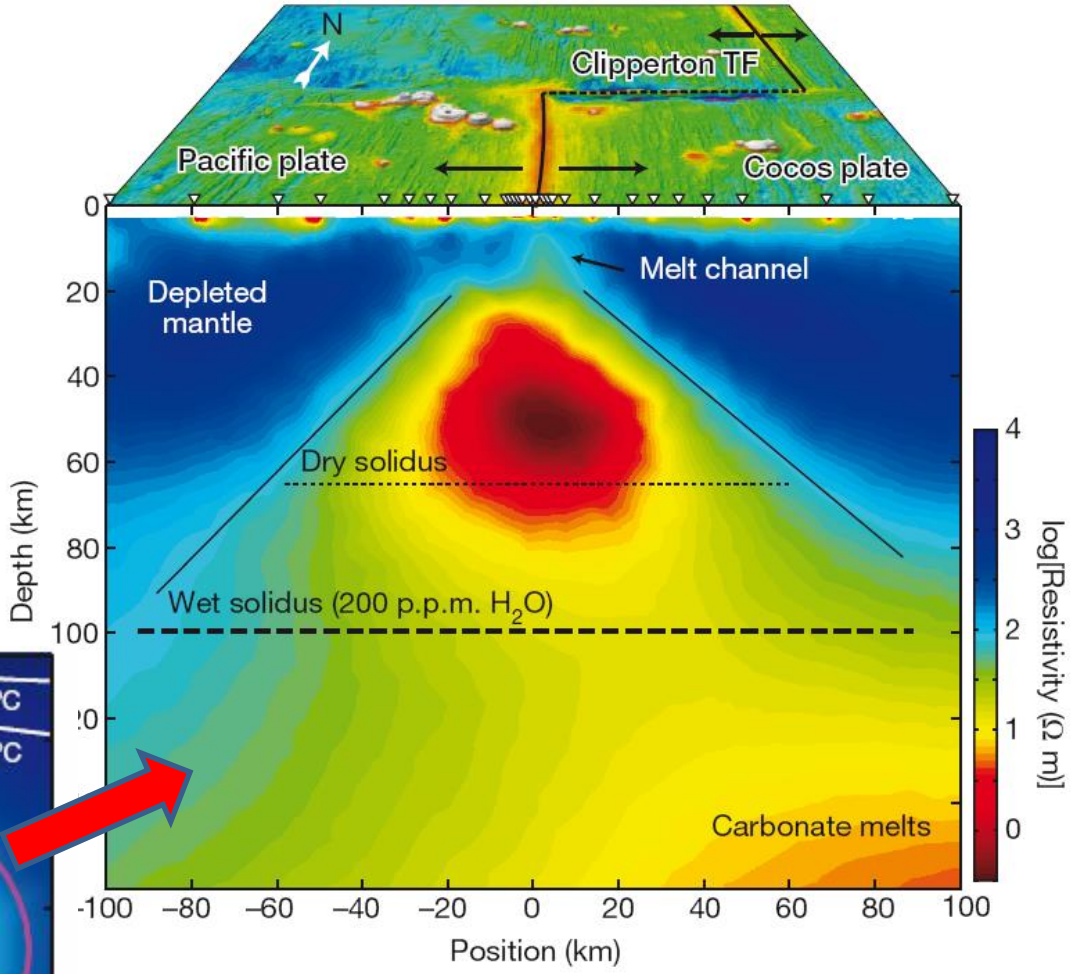

Key et al., 2013; Nature

Lentille magmatique supérieure

~100% liquide

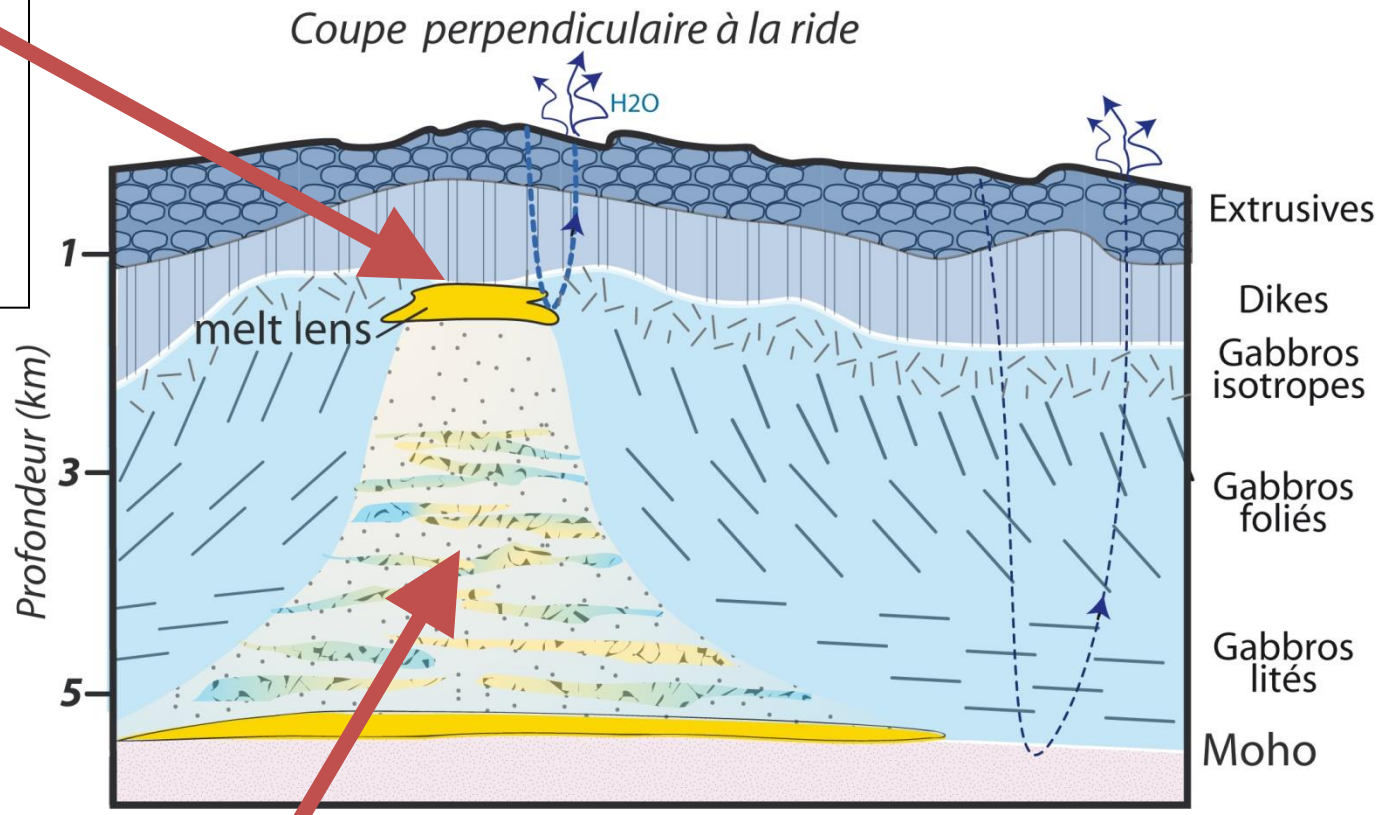

Chambre magmatique principale

< 20 % liquide

France et al., 2009

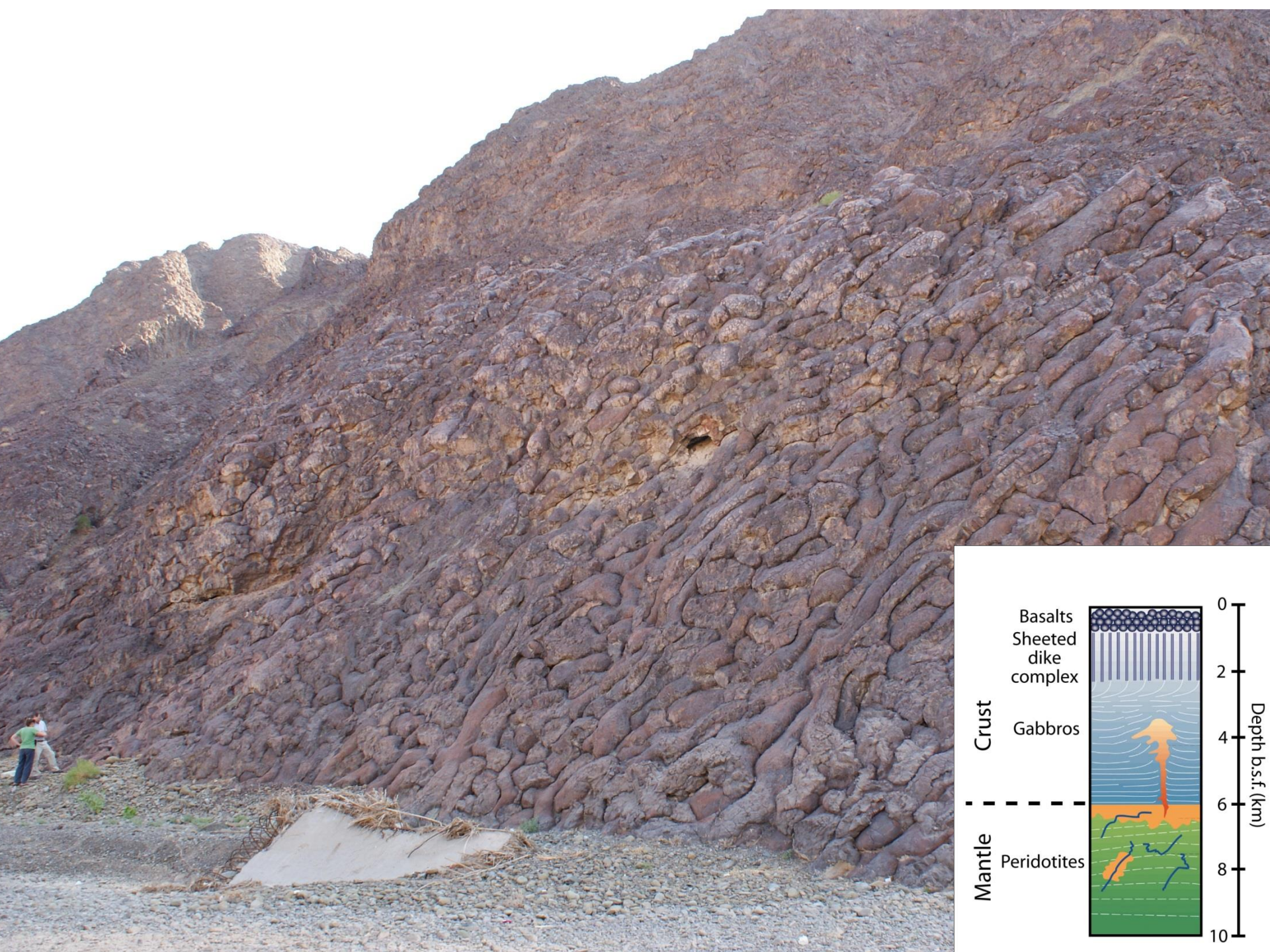
Basalts
Sheeted dike complex
Gabbros
Crust
Mantle
Peridotites
0
2
4
6
8
10
Depth b.s.f. (km)

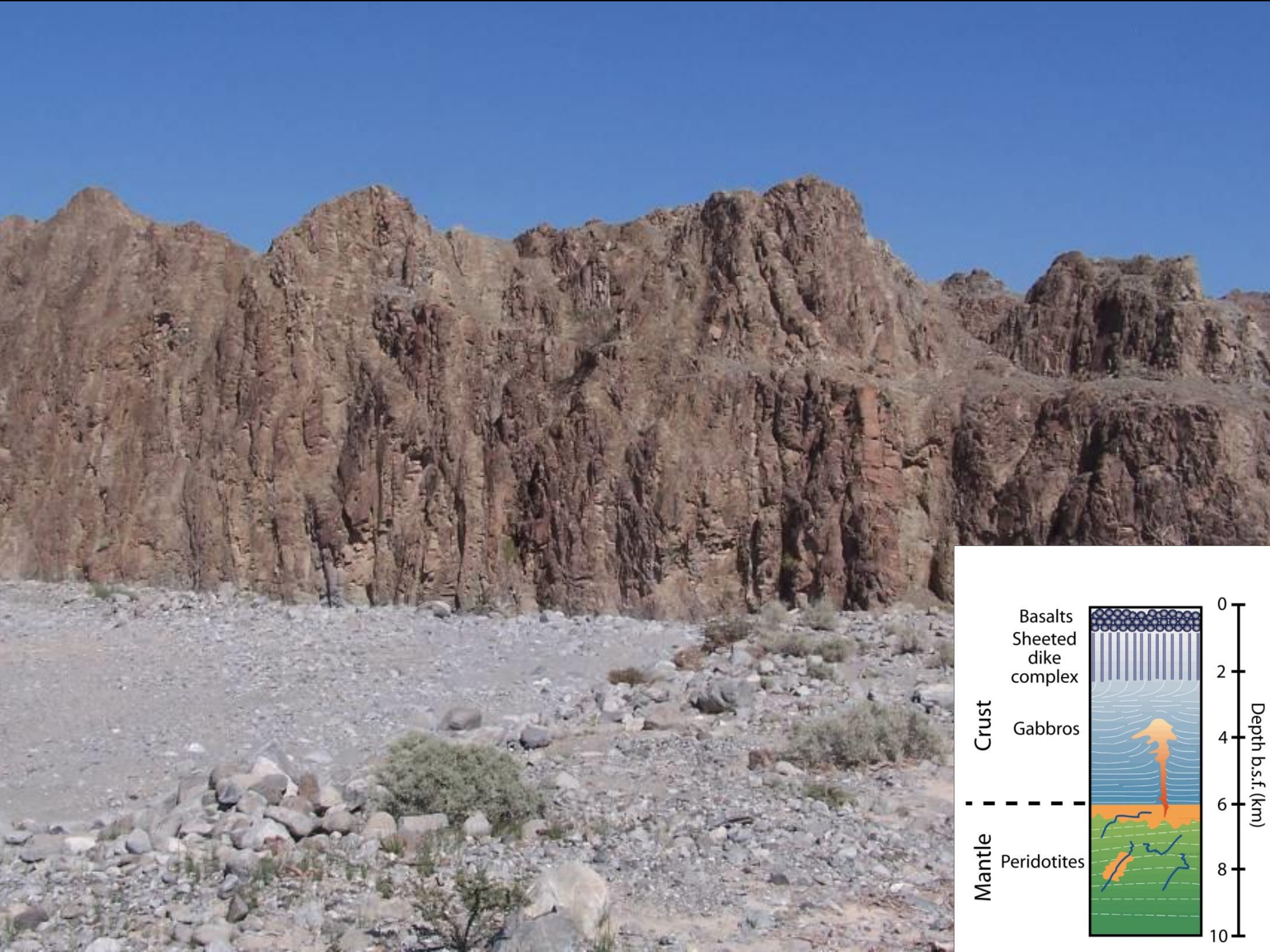
Basalts
Sheeted dike complex
Gabbros
Crust
Mantle
Peridotites
0
2
4
6
8
10
Depth b.s.f. (km)


Basalts
Sheeted dike complex
Gabbros
Crust
Mantle
Peridotites
0
2
4
6
8
10
Depth b.s.f. (km)

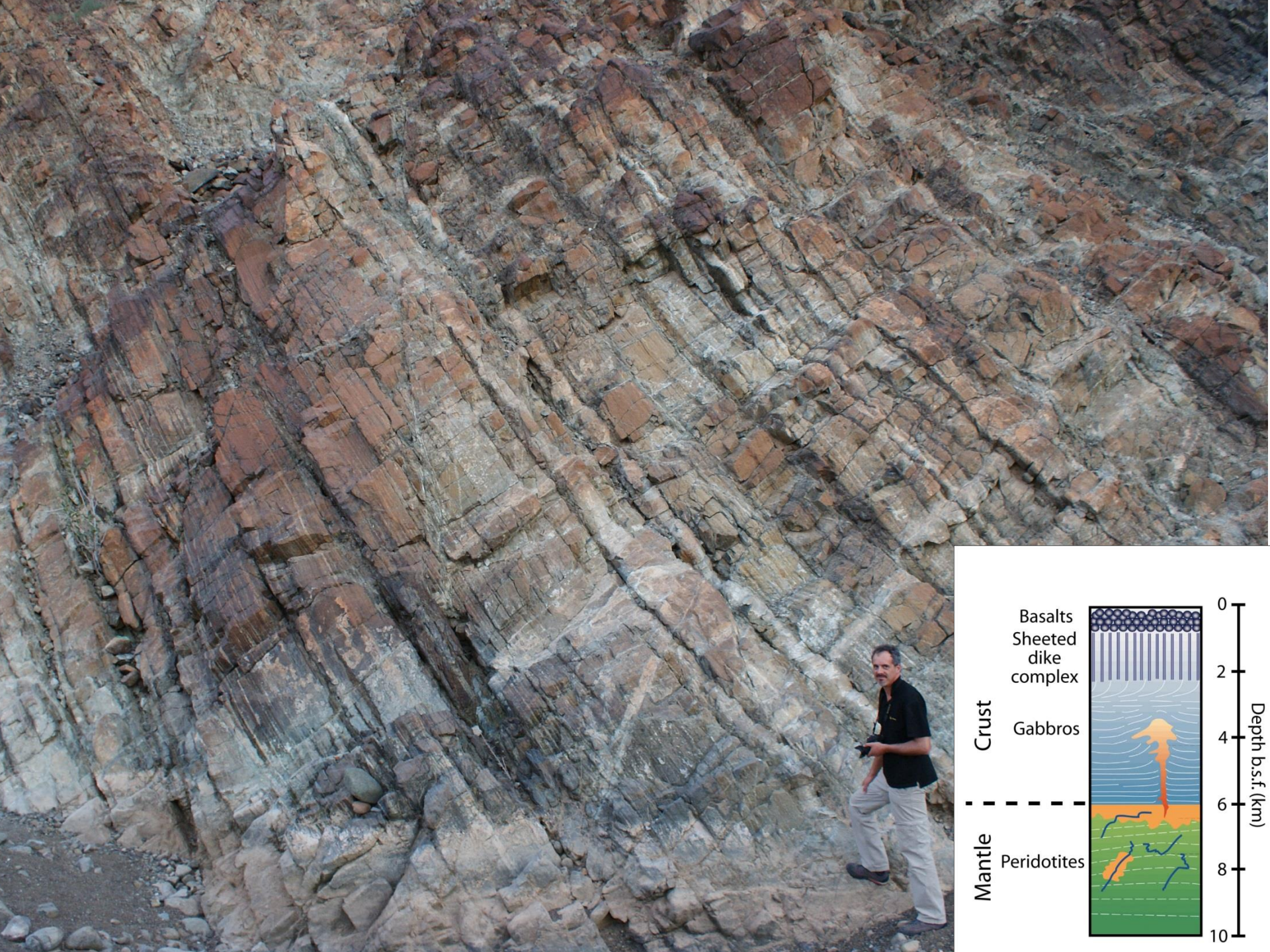
Basalts
Sheeted dike complex
Gabbros
Peridotites
Crust
Mantle
0
2
4
6
8
10
Depth b.s.f. (km)

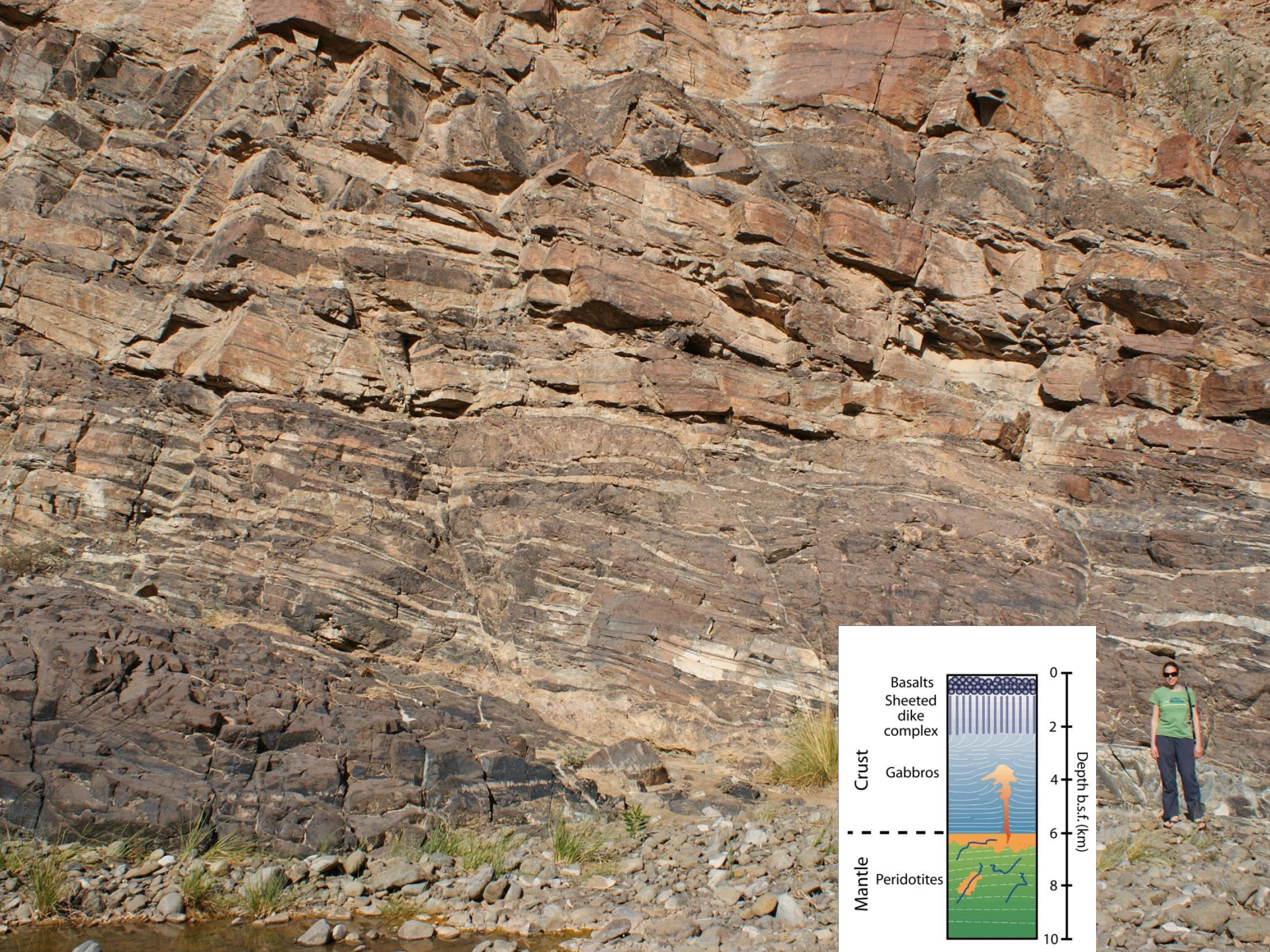
Basalts
Sheeted dike complex
Gabbros
Peridotites
Crust
Mantle
0
2
4
6
8
10
Depth b.s.f. (km)

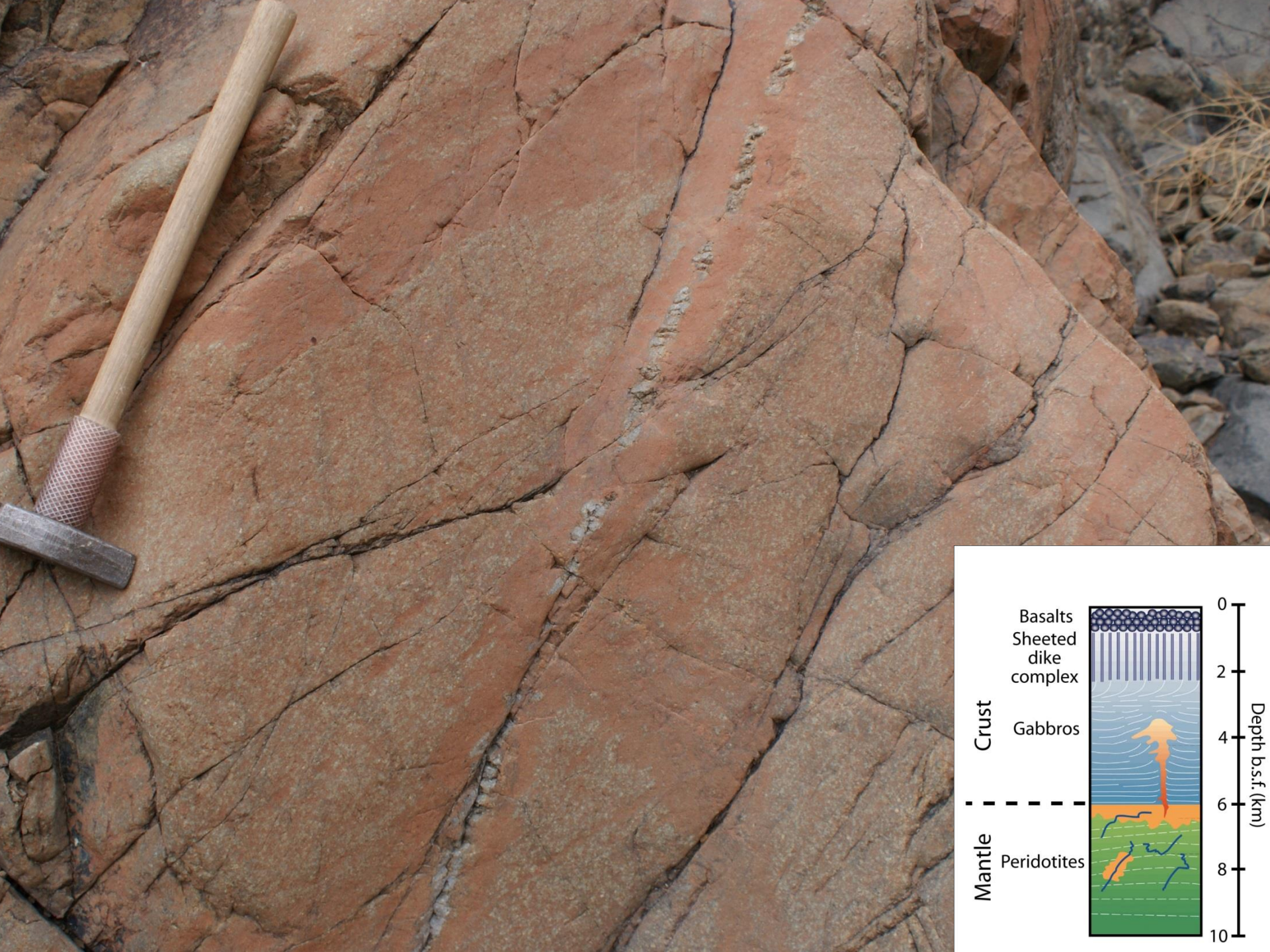
Basalts
Sheeted dike complex
Gabbros
Crust
Mantle
Peridotites
0
2
4
6
8
10
Depth b.s.f. (km)

MORB: Caractéristiques

Les basaltes des dorsales océaniques (MORB) ont des compositions assez homogènes

⇒ *tholéiites à olivine*

- 49-52 % SiO_2
- 6-10 % MgO

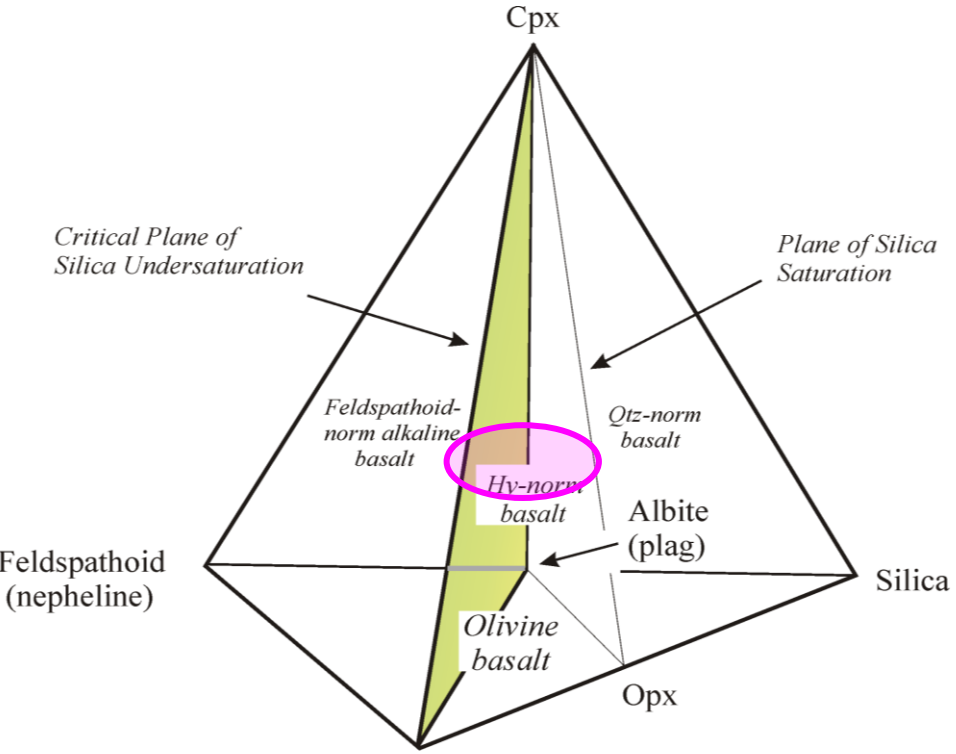

Picrites *(MgO > 12 wt.%)*

Assez rare, laves très porphyritic (olivine megacrysts Fo 91)

Basaltes à olivine *(MgO = 10 - 12 wt.%)*

Basaltes Porphyritic, (Ol Pheno > Plag. Pheno)
Principalement le long de l'axe de la dorsale.

Basaltes Ol-Plagio. *(MgO ≤10 wt.%).*

Basaltes Porphyritic, (Plag. Pheno > Ol Pheno)
Commun sur les flans de l'axe

Basaltes Plagio. *(Al_2O_3 ≥ 19 wt.%)*

Laves très porphyritic (Plag. megacrysts An 90), suremt cumulatif

Basaltes Plag. Cpx. *(MgO ≤7 wt.%)*

Basaltes Aphyric peu de cpx et plag. Pas d'ol.
Souvent en diabase

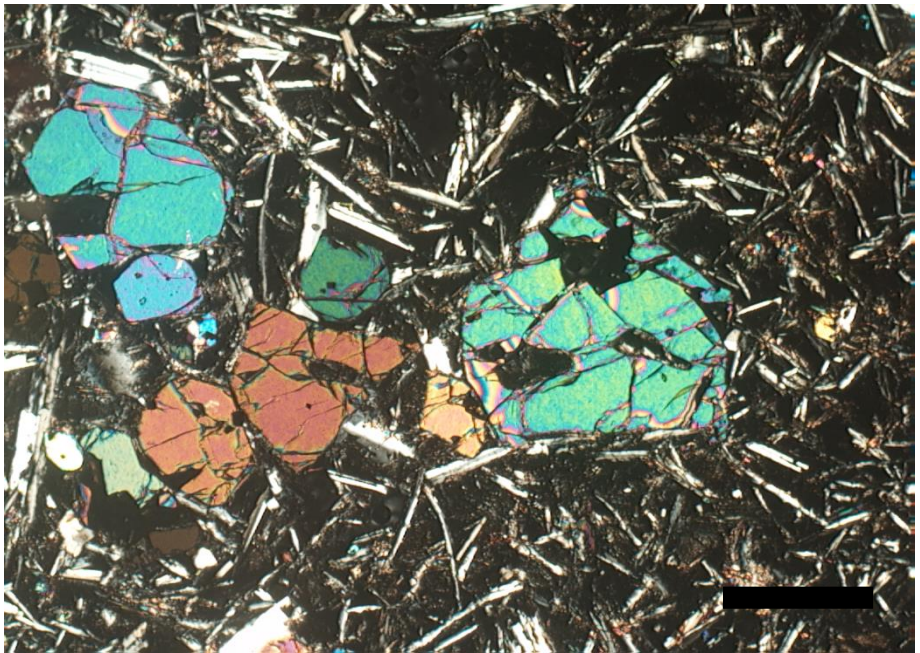

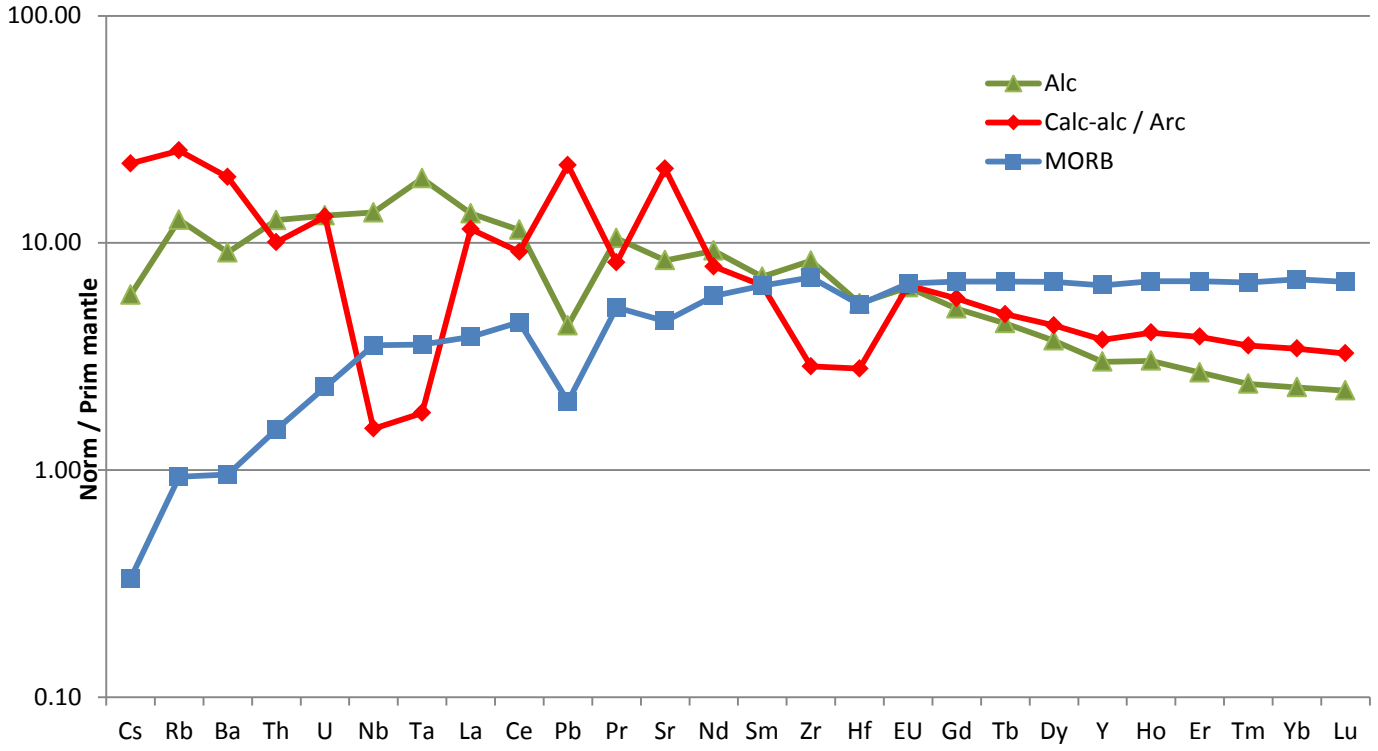
100.00
10.00
1.00
0.10
Norm / Prim mantle
Alc
Calc-alc / Arc
MORB
Cs Rb Ba Th U Nb Ta La Ce Pb Pr Sr Nd Sm Zr Hf EU Gd Tb Dy Y Ho Er Tm Yb Lu

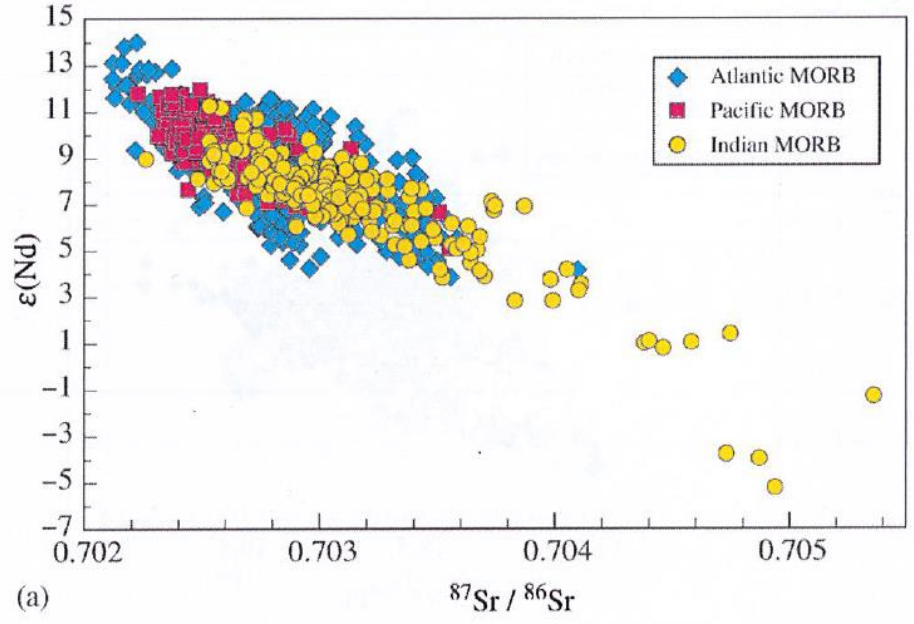
Atlantic MORB
Pacific MORB
Indian MORB
ε(Nd)
15 13 11 9 7 5 3 1 −1 −3 −5 −7
0.702 0.703 0.704 0.705
$^{87}Sr / ^{86}Sr$
(a)

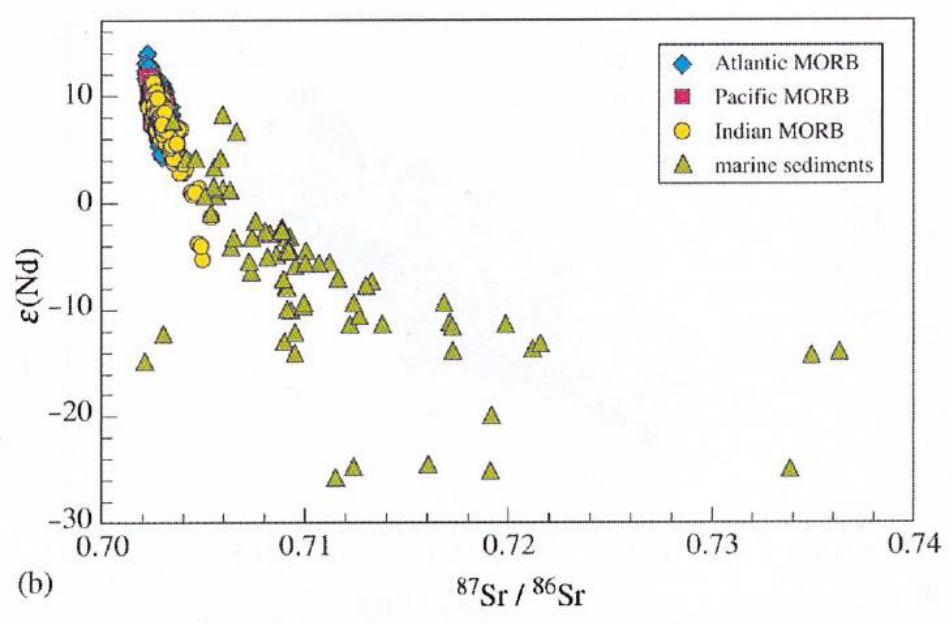
Atlantic MORB
Pacific MORB
Indian MORB
marine sediments
ε(Nd)
10 0 −10 −20 −30
0.70 0.71 0.72 0.73 0.74
$^{87}Sr / ^{86}Sr$
(b)

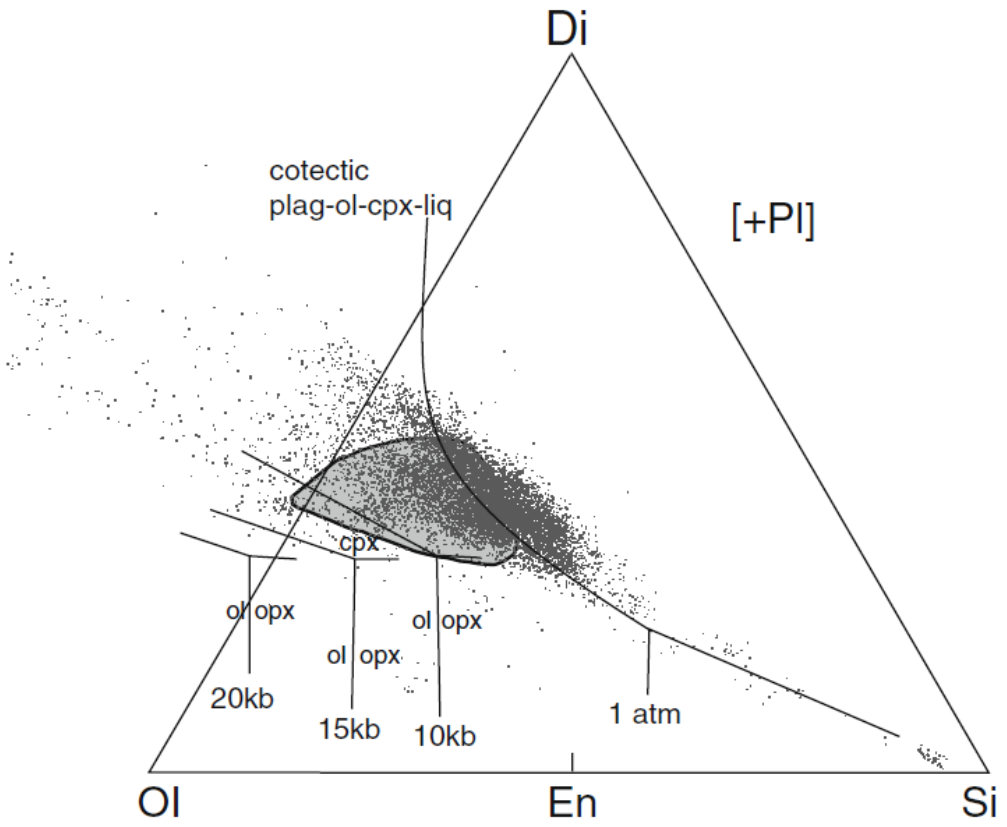

Fig. 1 A comparison of MORB compositions with the phase boundaries in a peridotite at 1 atm, 1, 1.5, and 2 GPa in the olivine–diopside–silica–plagioclase normative tetrahedron (liquid compositions are projected from plagioclase onto olivine–diopside–silica plane). Small dots correspond to 9,035 MORB glass analyses from the Smithsonian Institution catalogue (Melson and O'Hearn 2003: http://www.petdb.org/petdbWeb/index.jsp). The *shaded field* represents the range of primitive MORBs and corresponds to the 61 most primitive MORB glasses from the database with Mg# $\geq$ 67 (total Fe calculated as FeO). From Stolper (1980), with modifications; the algorithm used to calculate the projection is given in Walker et al. (1979)

Lambard 2009

Composition des MORB =

Composition de la source
+
Processus de fusion
+
Processus de transfert
+
Processus de cristallisation

Tout est interdépendant !!

MORB: Pétrogenèse

- Crystallisation fractionee polybarique
- Fusion fractionnee polybarique
- Reaction de fusion / composition du residu
- Fusion, aggregation, cristallisation: MORB
- Influence de la compo du manteau
- Mode de transfert

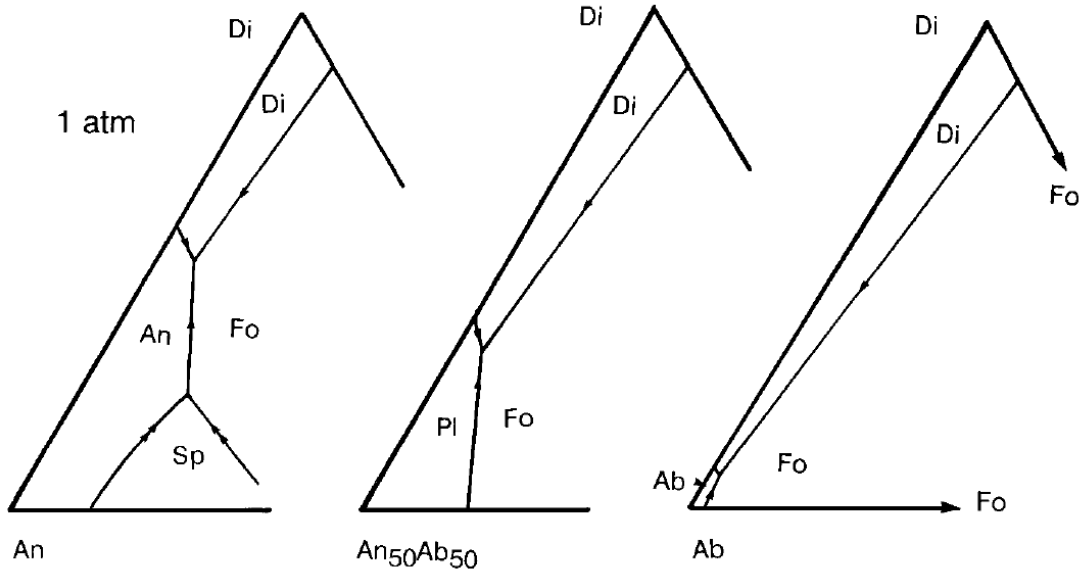

Fig. 2. Phase diagrams at 0.001 kbar for the systems Fo - Di - $Plag_{ss}$ from Biggar and Humphries [1981]. The ternary diagrams show the effect of varying Anorthite (An, $CaAl_2Si_2O_8$) and Albite (Ab, $NaAlSi_3O_8$) components on the composition of a liquid multiply saturated with Fo - Di - Plag. The effect of increased Ab content in the system is to move the 4 - phase boundary toward Plag.

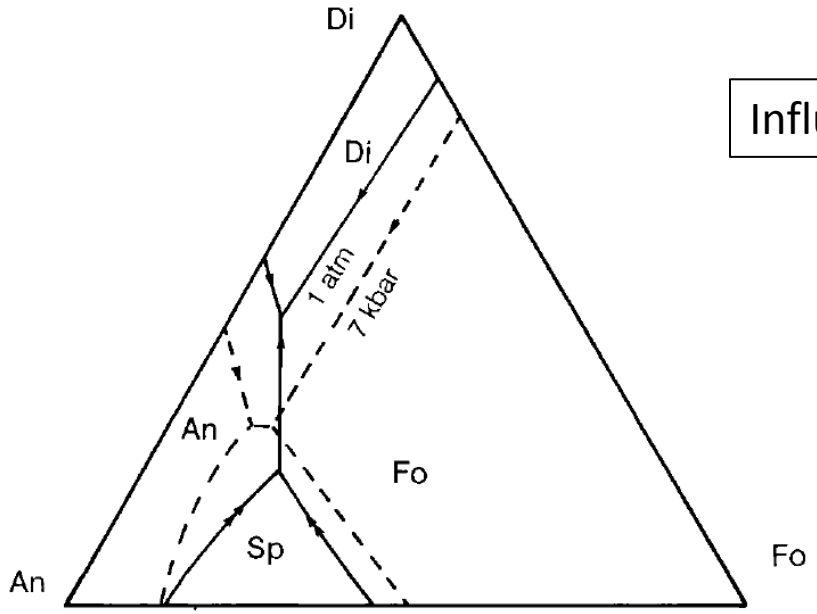

Influence de la composition et de la pression

Fig. 3. The effect of pressure in the system Fo - Di - An on the composition of a liquid saturated with Fo, Di and An is shown in this ternary diagram from Presnall et al. [1978]. Phase relations are shown for 0.001 kbar and 7 kbar. The assemblage Fo - Di - An - Liq is not stable above about 5 kbar, so the influence of pressure must be inferred from the 7-kbar relations. The effect of increased pressure is to move the boundary toward the Fo-An side line.

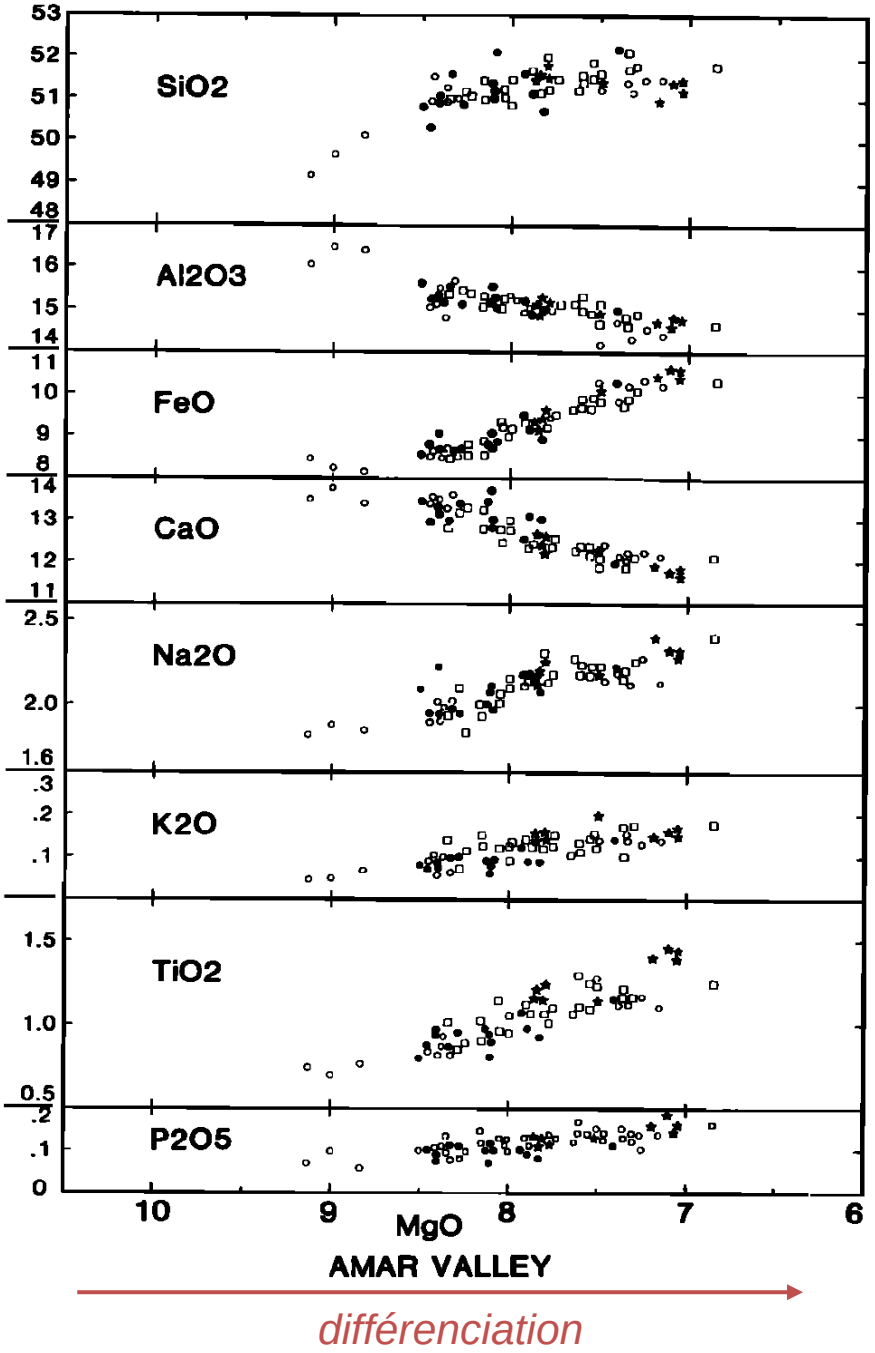

Stakes et al. (1984)

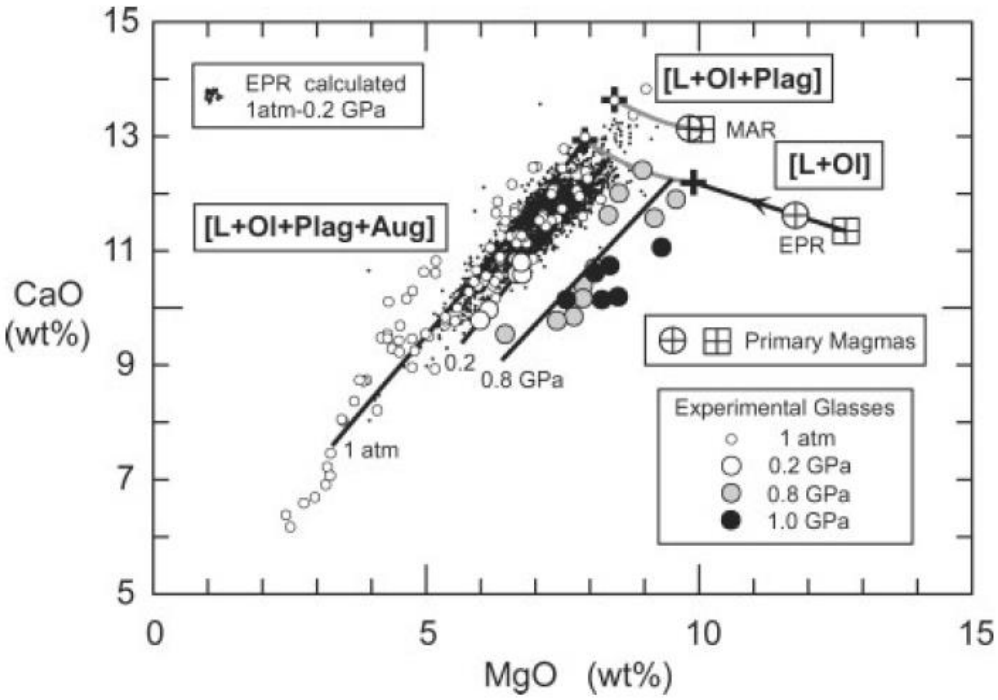

Herzberg, 2004

Fractionnement Polybarique

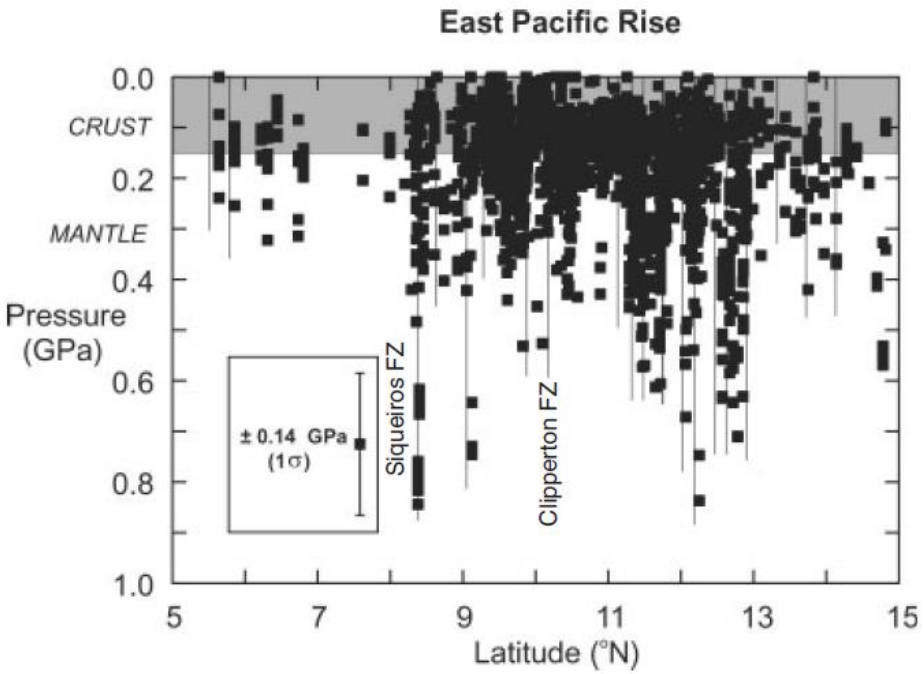

Fig. 8. Pressures of Ol + Plag + Aug fractionation for MORB from the East Pacific Rise between 5°N and 15°N calculated using equation (6). The Siqueiros and Clipperton Fracture Zones are indicated; all others are that are not labelled are overlapping spreading centers and deviations from axial linearity from Langmuir *et al.* (1986). It should be noted that the highest pressures are usually observed for MORB associated with ridge segment terminations, especially the Siqueiros Fracture Zone and the group of terminations at 11–13°N. Glasses for which Ol + Plag fractionation was likely have been filtered out as discussed in the text; these have CaO > −0·3MgO + 14·5. If this window of filtering is widened further by lowering CaO another 1%, then 65% of the total glass population would be excluded, and it would have the undesirable effect of excluding glasses that had fractionated Ol + Plag + Aug. Nevertheless, it can be shown that there is no change in the correlation of high pressures of crystallization with ridge segment terminations.

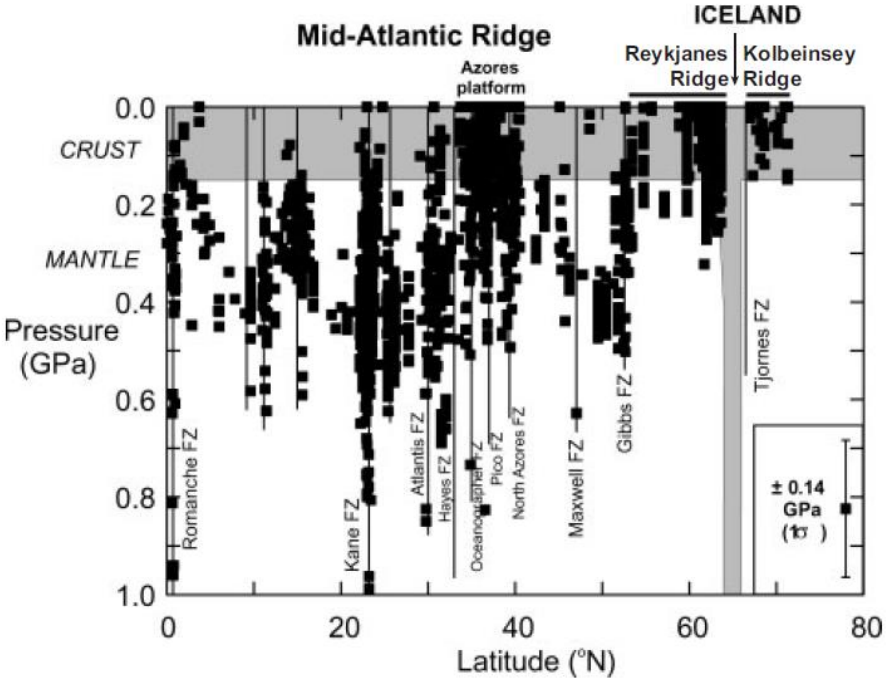

Fig. 9. Pressures of Ol + Plag + Aug fractionation for MORB from the Mid-Atlantic, Reykjanes, and Kolbeinsey Ridges calculated using equation (6). Glasses for which Ol + Plag fractionation was likely have been filtered out as discussed in the text. It should be noted that the highest pressures are usually observed for MORB associated with fracture zones. This figure is very similar to one shown by Dmitriev (1998), who computed pressures using a modified method of Danyushevsky *et al.* (1996).

Herzberg, 2004

Influence du taux d'expansion de la ride sur la teneur en MgO ⇒ les basaltes de rides lentes sont moins différenciés que les basaltes de dorsales rapides

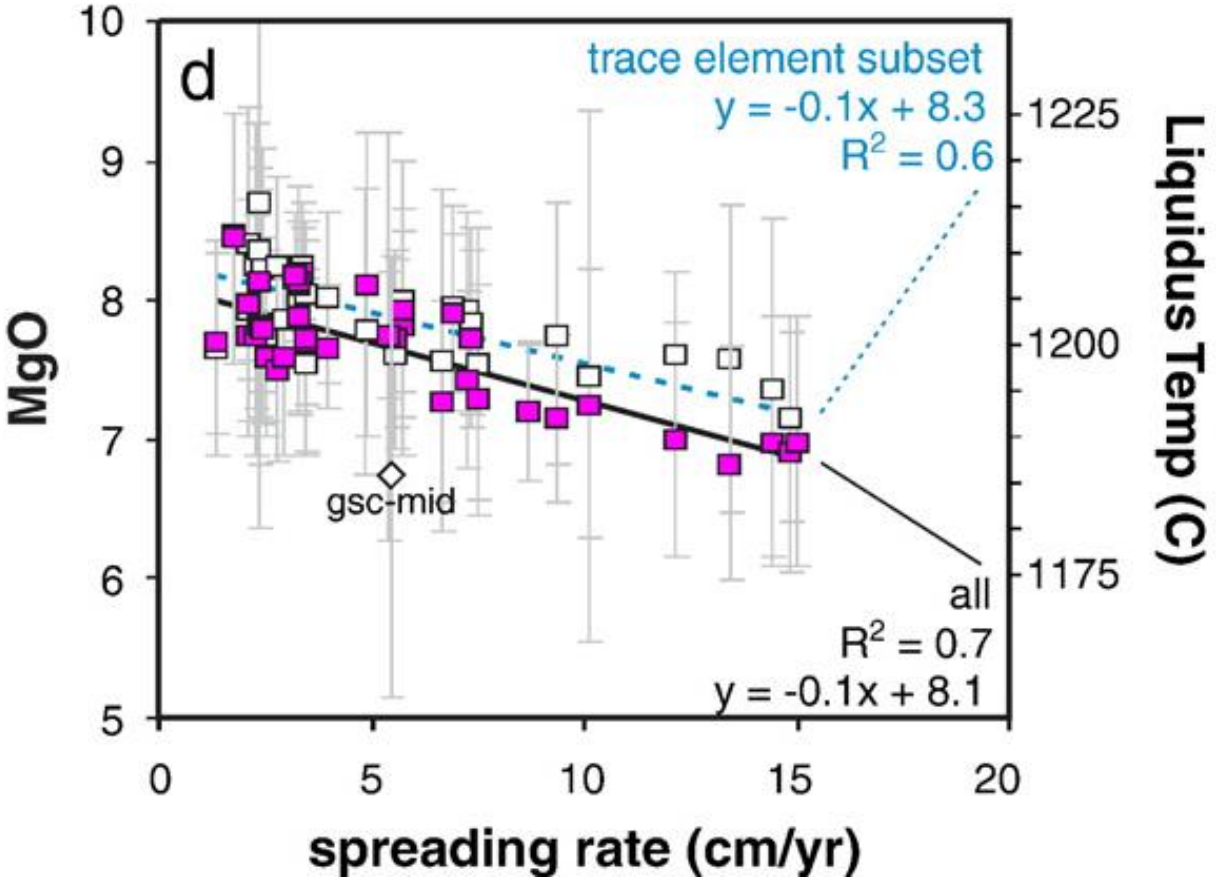

Rubin and Sinton (2007)

Les basaltes de rides lentes conservent la signature de la variabilité des magmas parents, ce qui est cohérent avec un fonctionnement plus épisodique des chambres magmatiques.

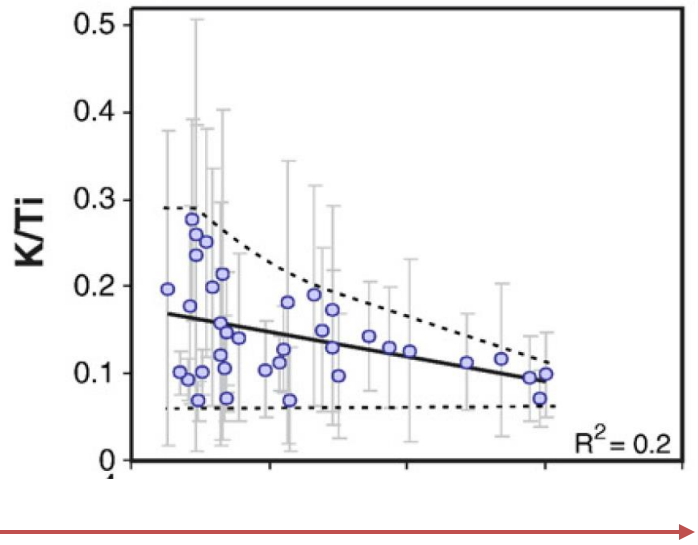

Spreading rate (cm/year)

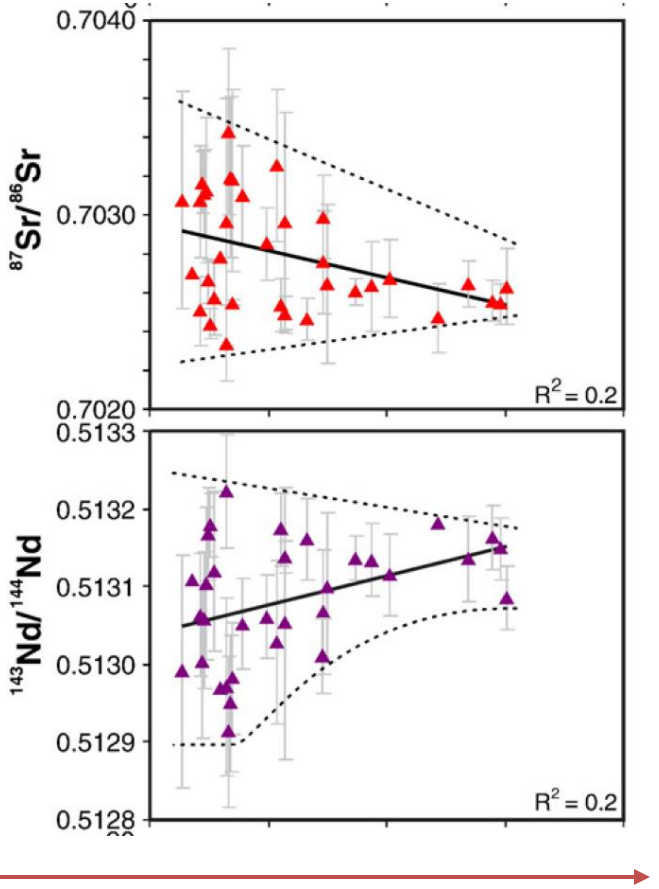

Spreading rate (cm/year)

Rubin and Sinton (2007)

Manteau plus chaud = taux de fusion plus élevés = croûte océanique plus épaisse

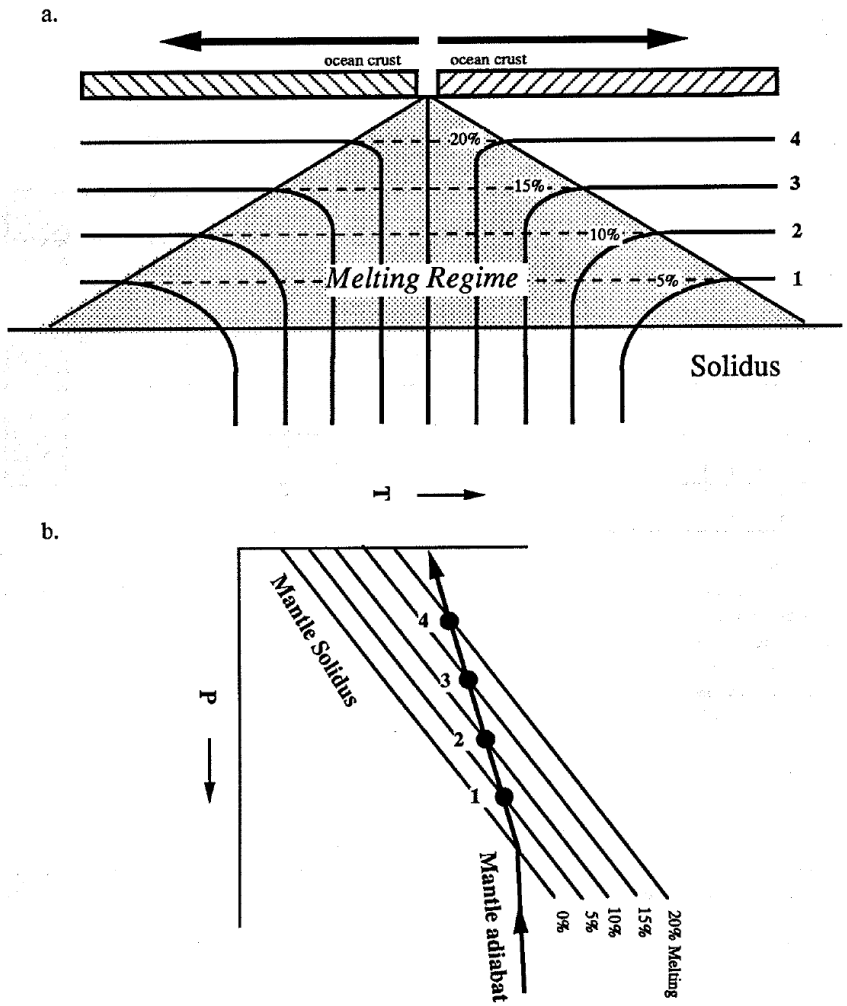

Fig. 33. *a*) Schematic view of the melting regime for simple corner flow circulation beneath the ridge resulting from passive upwelling as a result of spreading. Solid lines (without arrows) are mantle flow lines; the shaded region is the melting regime, contoured for the extent of melting (labelled dashed lines). *b*) Schematic pressure-temperature path for adiabatic melting resulting from upwelling and intersection of the mantle solidus. The region above the solidus is contoured for the extent of melting. The numbered dots (1-4) correspond to the maximum extent of melting that each numbered flow line in Panel (a) undergoes. Thus, the single melting path in (b) is a representation of the melting systematics that occur in the two-dimensional melting regime shown in Panel (a).

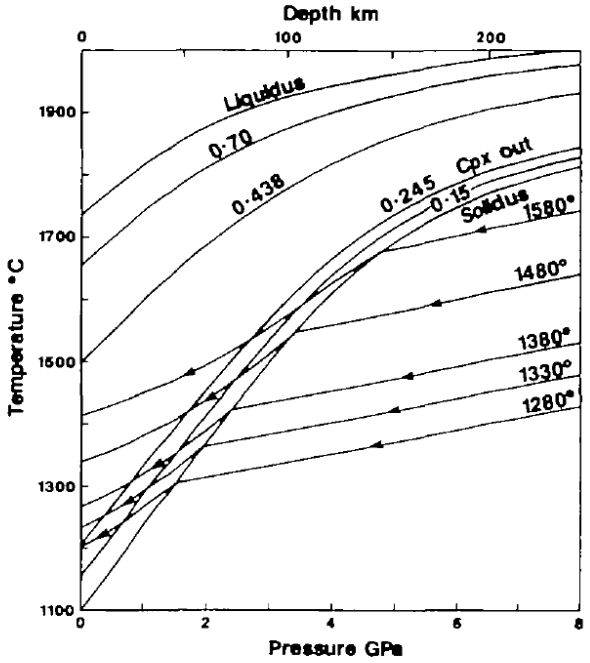

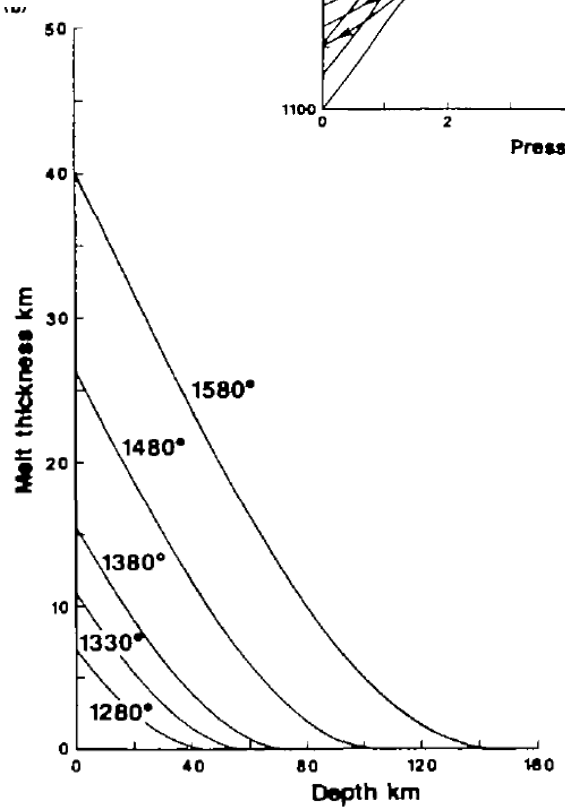

TOUS les MORB ont subis une évolution
Magmas primitifs ?

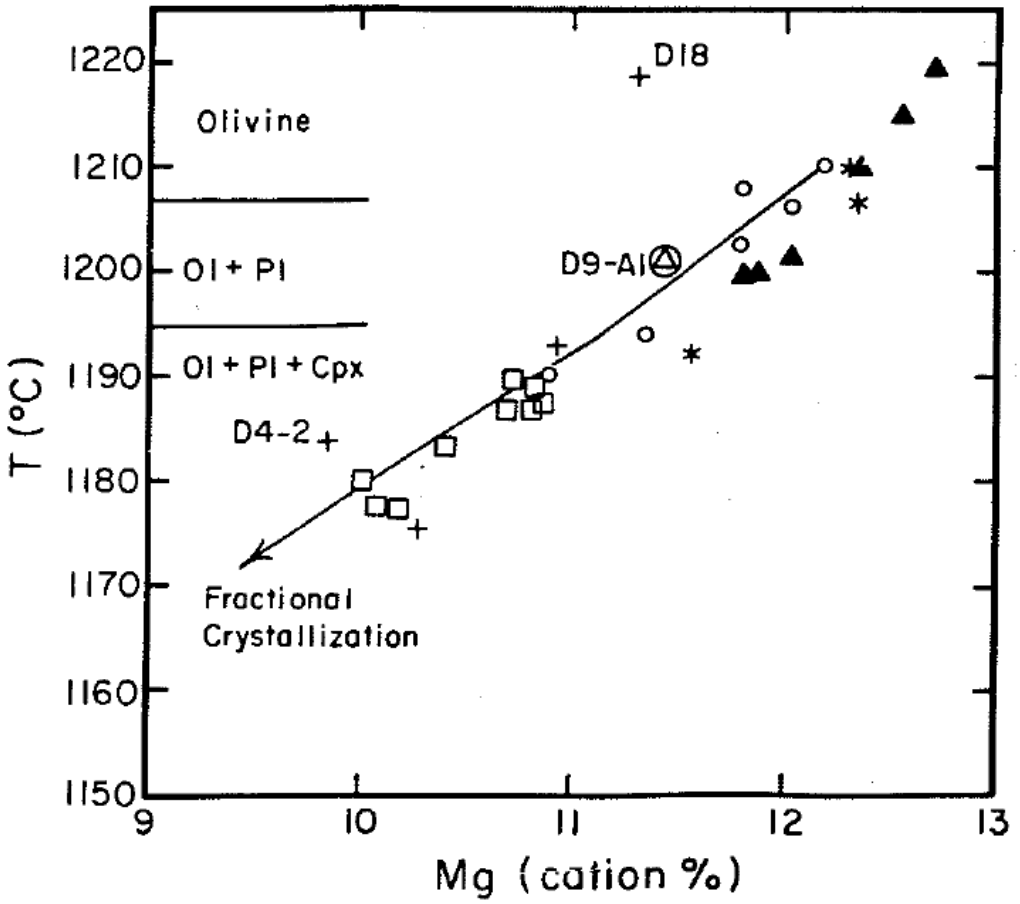

Fig. 10. Calculated liquidus temperatures for basalt glasses from the Tamayo region of the East Pacific Rise vs. MgO. The LLD for one of the samples is shown for reference. LLD, liquidus temperatures, and phase appearances are calculated from the method of *Weaver and Langmuir* [1990]. Figure is from *Bender et al.* [1984].

Langmuir 92

MORB: Pétrogenèse

- Crystallisation fractionee polybarique
- Fusion fractionnee polybarique
- Reaction de fusion / composition du residu
- Fusion, aggregation, cristallisation: MORB
- Influence de la compo du manteau
- Mode de transfert

MgO = 8 wt. %

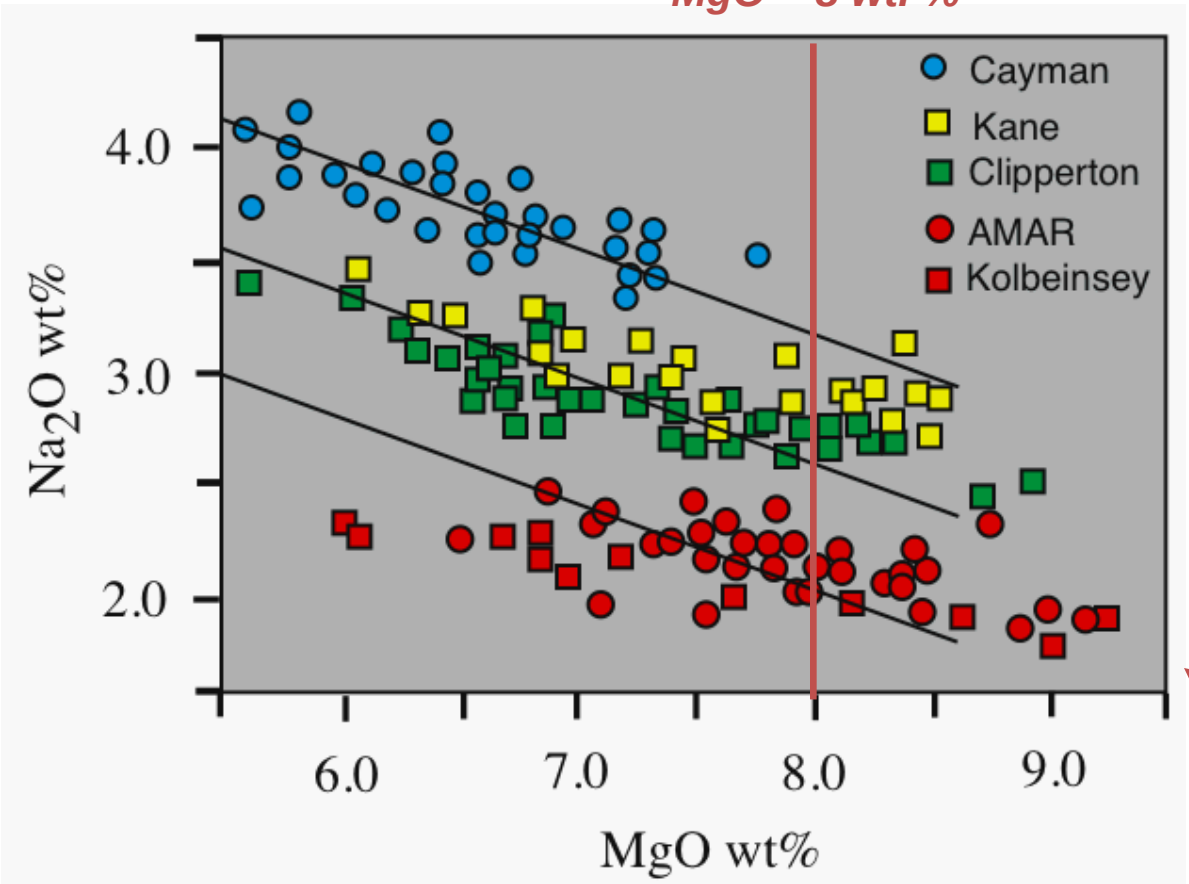

Langmuir (1992)

Magma primitif

Cristallisation fractionnée

Afin de comparer les liquides basaltiques, ⇒ ***normalisation à MgO 8 wt. %***

• *Taux de fusion* : teneur en Na_2O (présent uniquement dans les cpx) diminue avec le taux de fusion)
• *Pression de la fusion* : teneur en FeO augmente avec la pression

Augmenation taux de fusion

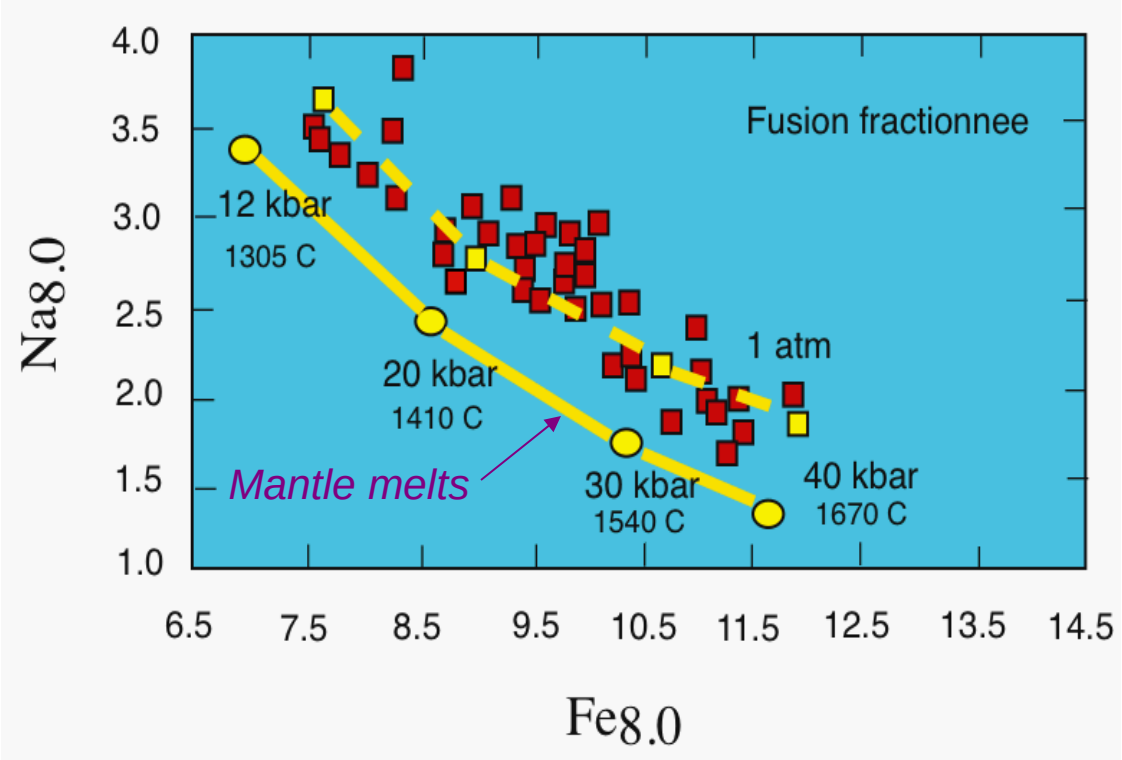

Langmuir (1992)

Augmentation pression

Exemple de la SWIR (Ride Sud-Ouest Indienne)

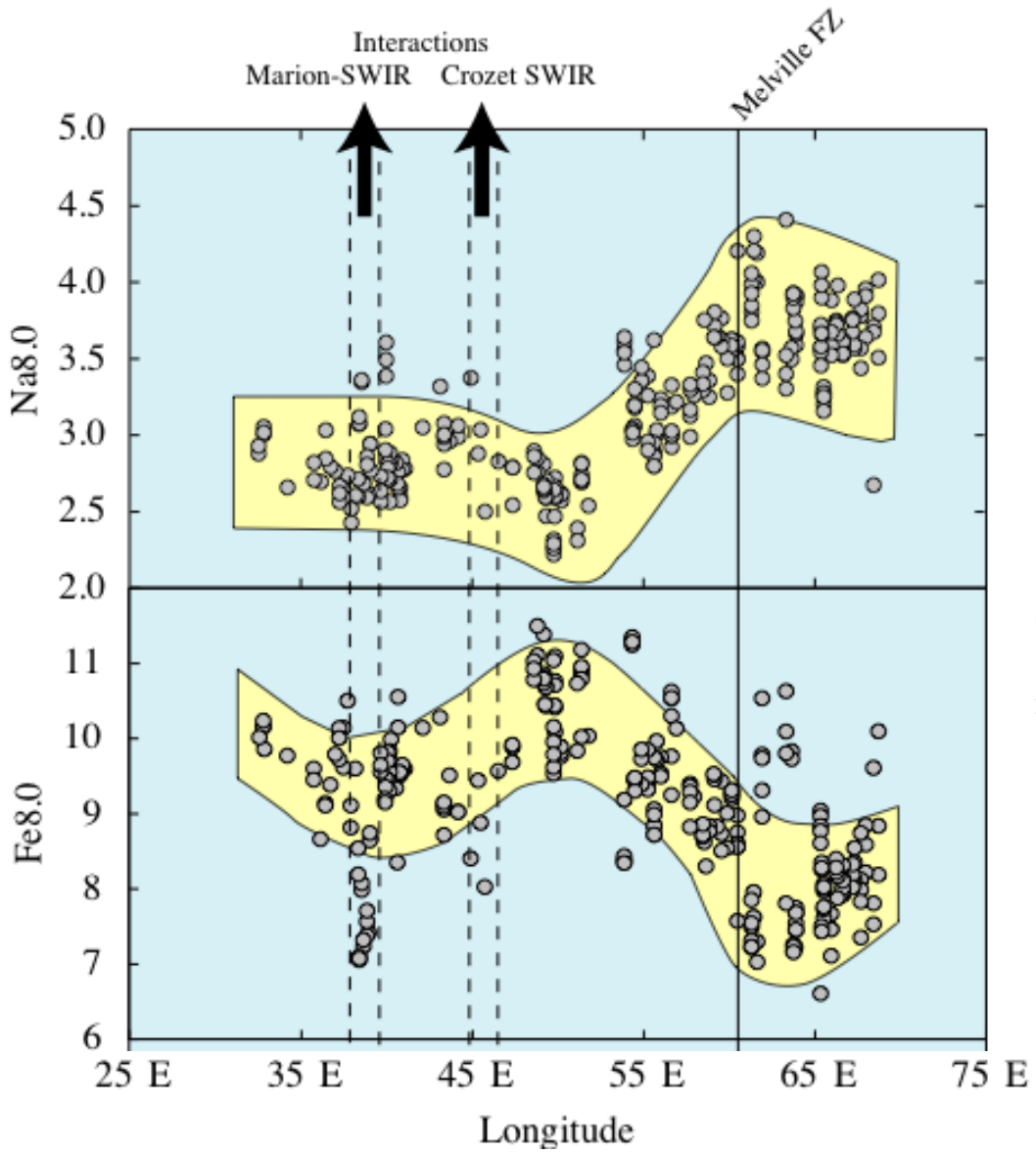

Le taux de fusion est plus faible à l'Est

Cependant, la réalité est plus complexe

⇒ Hétérogénéité du manteau

Seyler et al. (2003)

Polybaric (near) fractionnal melting
Auto-entretenue (FeO loss -- > densité…)

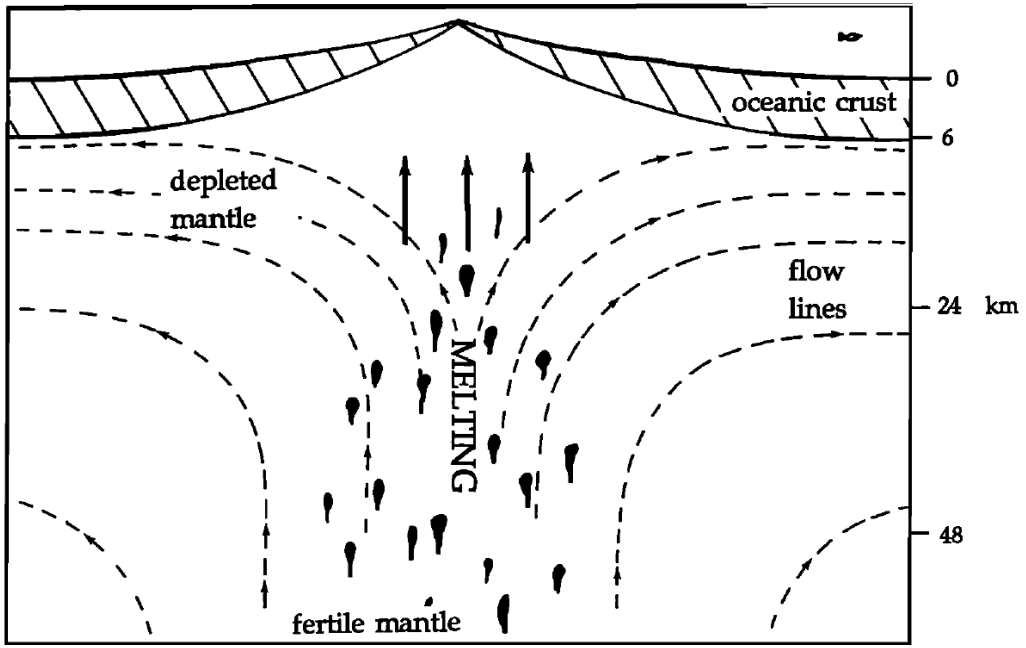

Fig. 1. Schematic diagram of decompression melting in the upper oceanic mantle (not to scale).

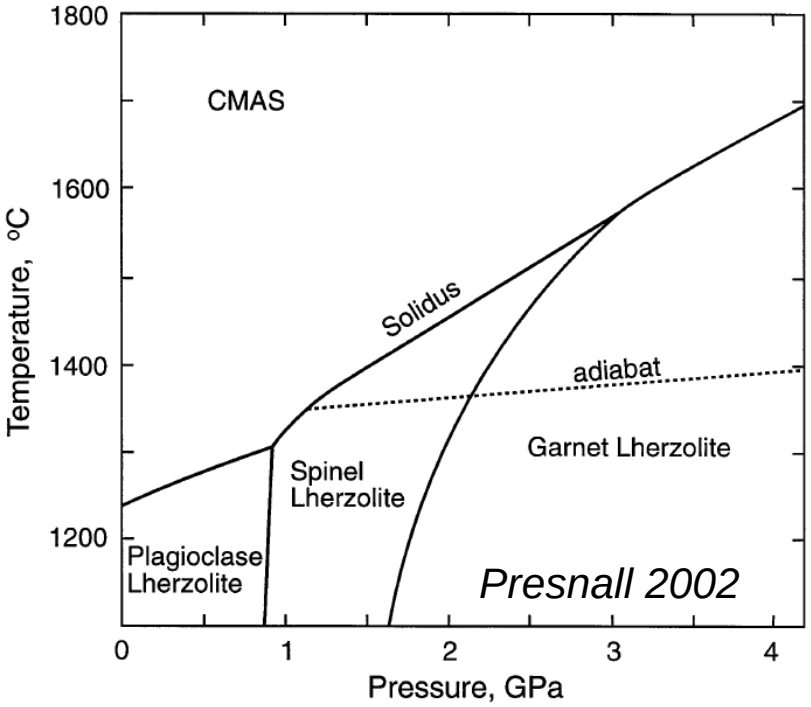

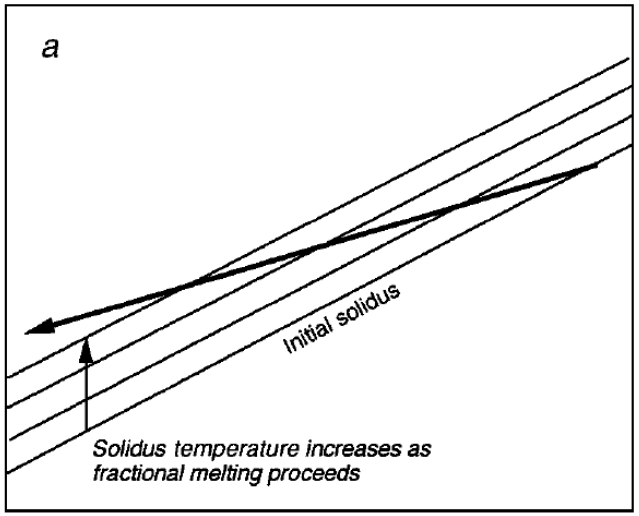

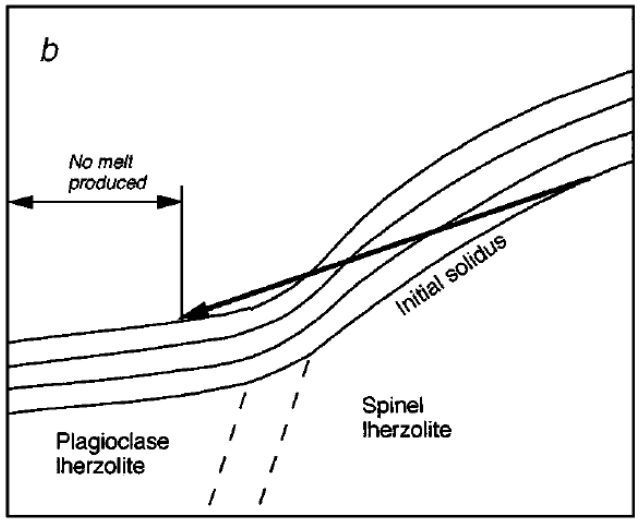

Kushiro 2001

MORB: Pétrogenèse

- Crystallisation fractionee polybarique
- Fusion fractionnee polybarique
- Reaction de fusion / composition du residu
- Fusion, aggregation, cristallisation: MORB
- Influence de la compo du manteau
- Mode de transfert

Relation de phases à différentes pression

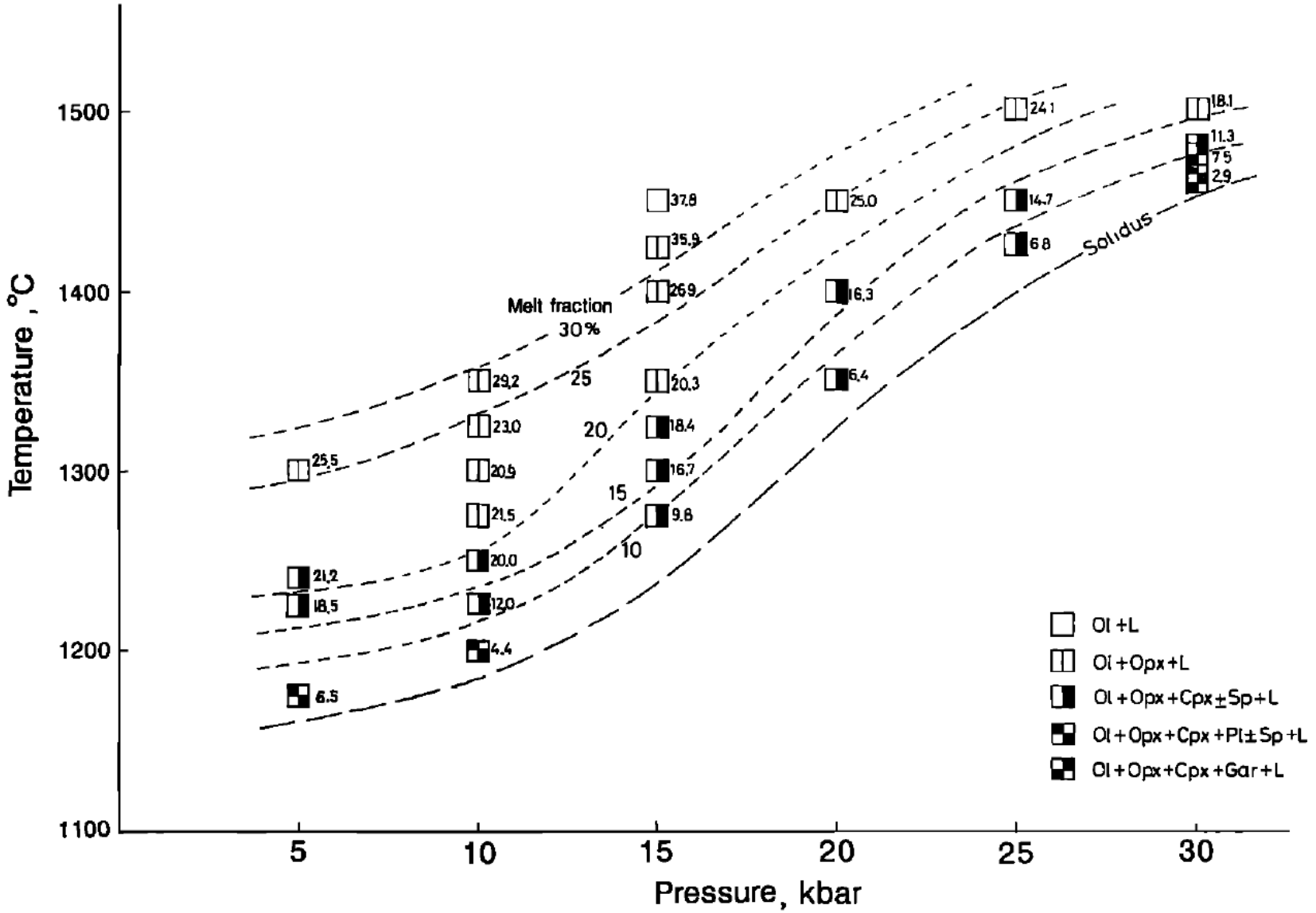

Fig. 2. Pressure-temperature diagram showing conditions of runs and isopleths (dashed lines) of melt fractions. Solidus was estimated by extrapolating the temperature-melt fraction curves given in Fig. 3.

Kushiro 96

Relation de phases a différentes pression

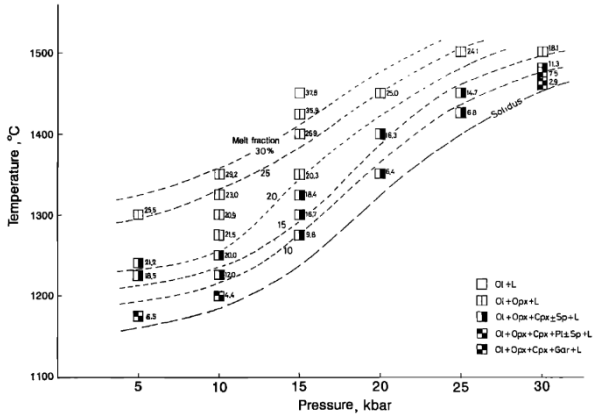

Fig. 2. Pressure-temperature diagram showing conditions of runs and isopleths (dashed lines) of melt fractions. Solidus was estimated by extrapolating the temperature-melt fraction curves given in Fig. 3.

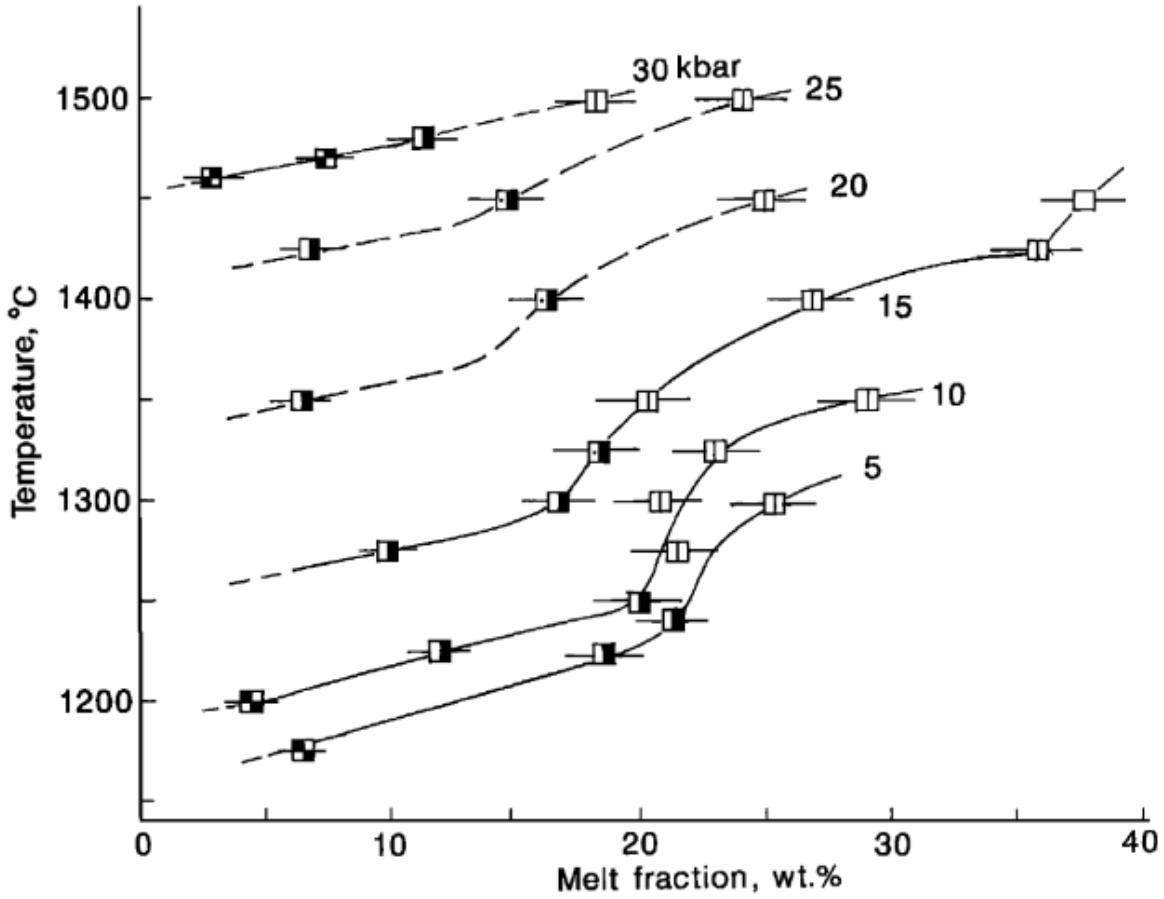

Kushiro 96

. 3. Temperature-melt fraction curves at 5, 10, 15, 20, 25 and 30 kbar. Bars indicate 10 % uncertainties in melt fraction.

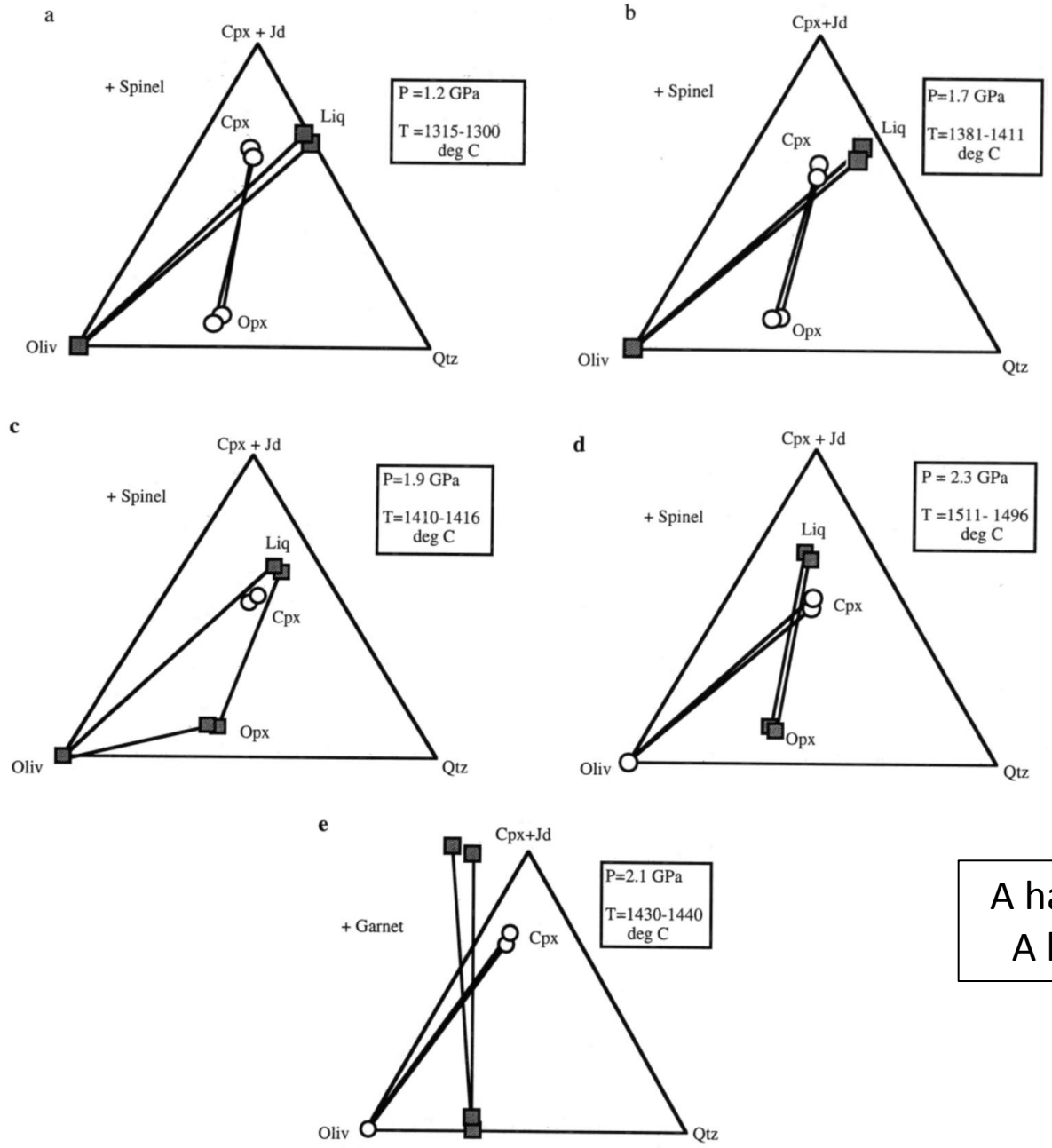

Figure 3. Oxygen normalized mineral component projection through spinel (in the case of Figures 3a-3d) and through garnet (in the case of Figure 3e) onto the pseudo-ternary defined by ol (olivine), qtz (quartz) and the sum cpx+jd (clinopyroxene + jadeite). See text for discussion.

Kinzler 97

A haute pression résidu enrichi en Opx,
A basse pression résidu enrichi en Ol

EVOLUTION DE LA Composition des minéraux de la péridotite résiduelle

La composition chimique des minéraux varie en fonction du taux de fusion.

⇒ Conséquence de l'(in)compatibilité des éléments chimiques (Fe, Al, Mg, …)

⇒ *Spinelle chromifère* sensible à la fusion partielle (Cr, Mg dans solide et Al dans liquide)

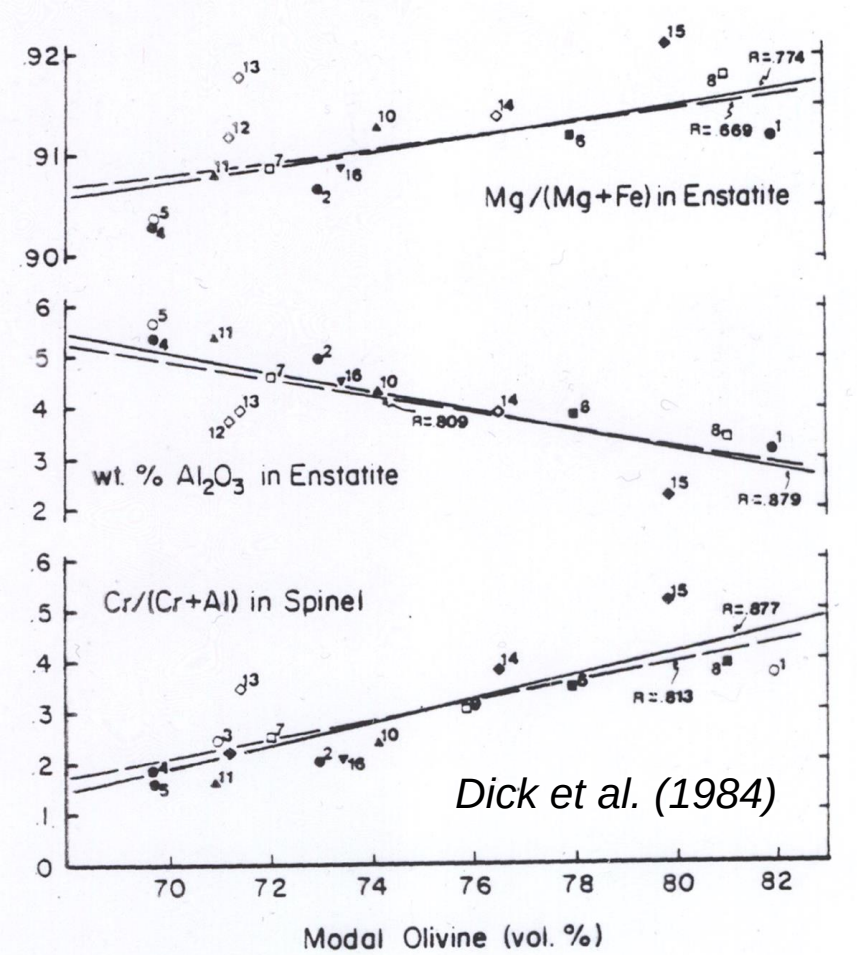

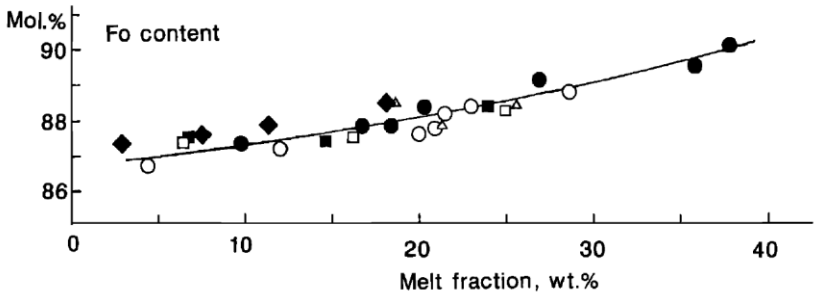

Fig 7. Compositional variations of olivine as a function of degree of melting. Symbols are the same as those in Fig. 5.

Kushiro 96

Arai (1994)

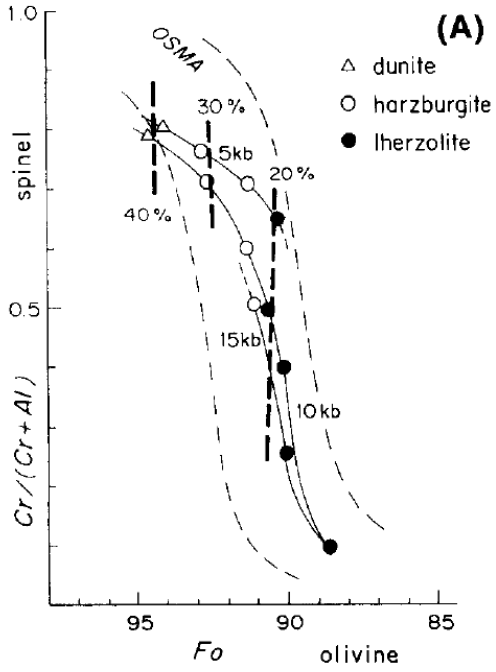

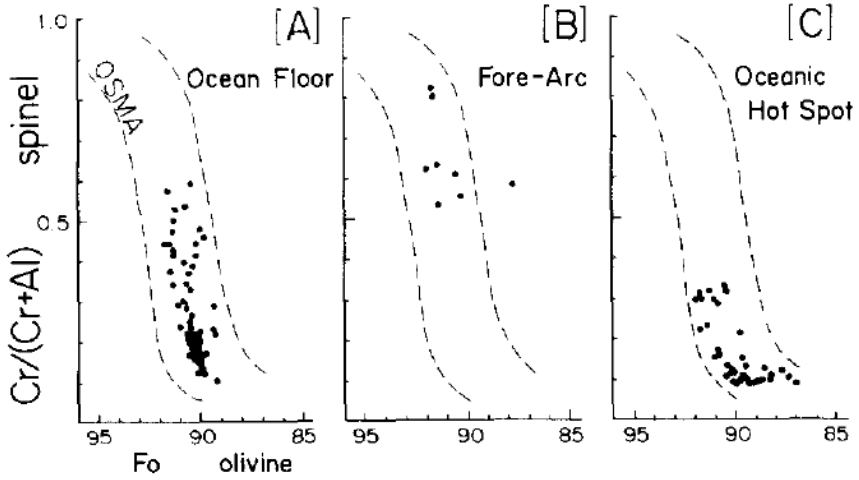

a. subsolidus formation of Al-rich phase

b. metasomatism

c. fractional crystallization

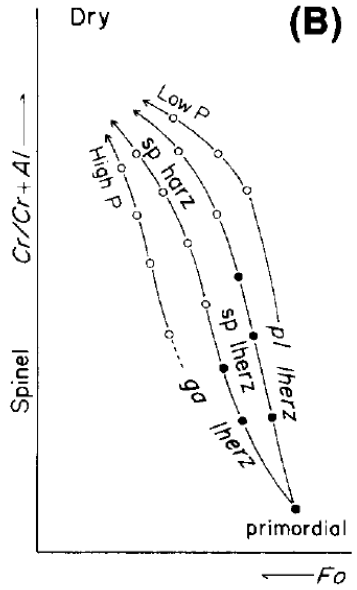

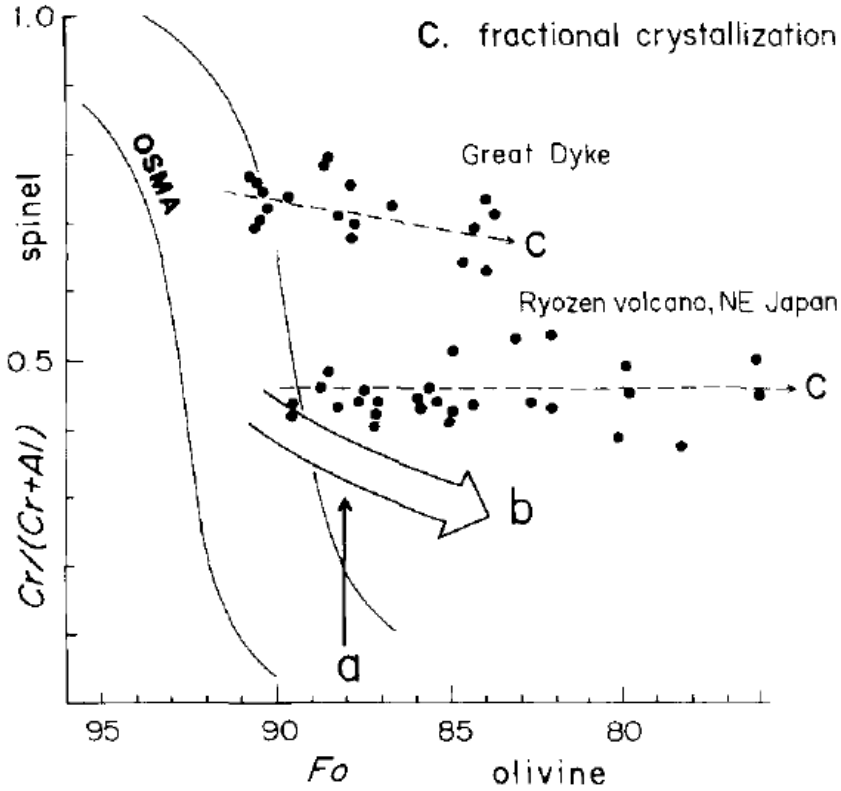

MORB: Pétrogenèse

- Crystallisation fractionee polybarique
- Fusion fractionnee polybarique
- Reaction de fusion / composition du residu
- Fusion, aggregation, cristallisation: MORB
- Influence de la compo du manteau
- Mode de transfert

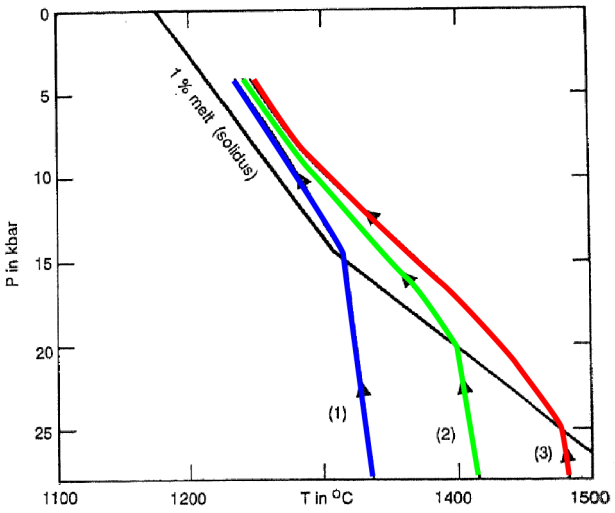

Fig. 7. Diagram showing three pressure-temperature paths (solid curves with arrows) of mantle peridotite (H&Z dep 1 composition) undergoing polybaric, incremental batch melting with incomplete melt withdrawal (model 3 melting process). The "1% solidus" (solid curve) is also shown. The "potential temperatures" (the temperature at which adiabatically upwelling mantle begins to melt [*McKenzie and Bickle*, 1988]) of the mantle peridotite are 1315, 1395, and 1475 °C for melting paths 1, 2, and 3, respectively (the numbers are the reverse of the models in Table 4). The mantle peridotite adiabat is assumed to be 0.6°C/kbar [*McKenzie*, 1984]. Note the shift in the inflection or break in slope of the melting paths to shallower pressures as the extent of depletion of the mantle peridotite source increases from path 1 to path 3, which indicates the diminishing pressure range over which plagioclase is stable in the upper mantle with decreasing Na_2O in the more depleted peridotite source.

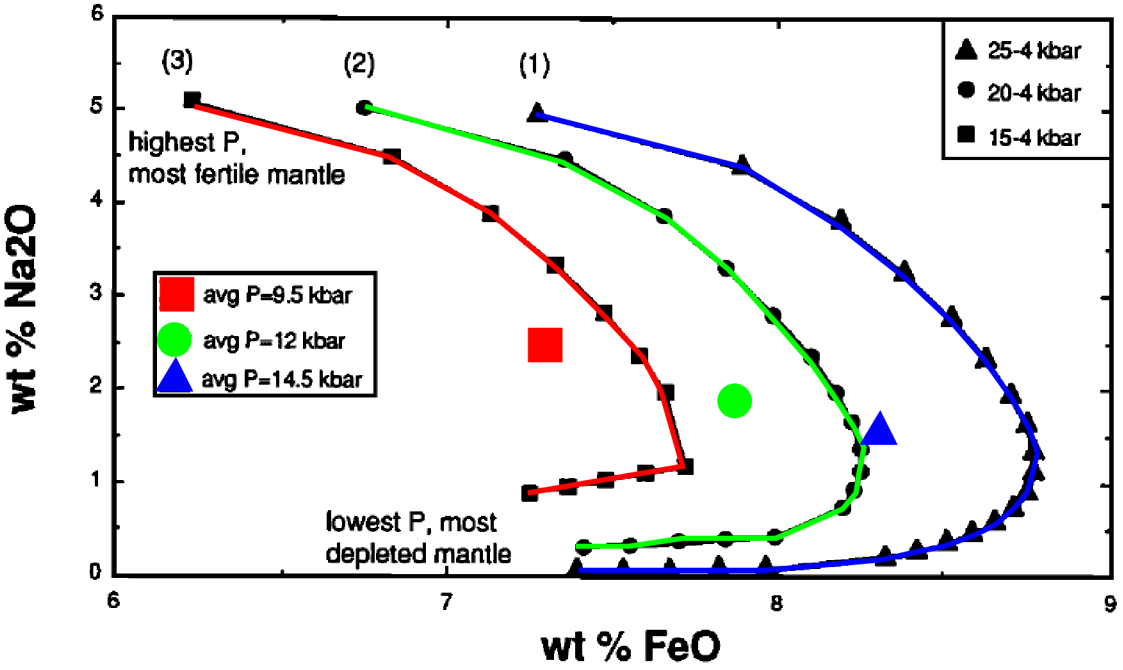

Fig. 6. Weight percent Na_2O versus weight percent FeO for model 3 melting paths (examples 1, 2, and 3, Table 4). Each solid symbol along a given curve shows the composition of a 1% increment of melt produced as H&Z dep 1 mantle rises and undergoes polybaric, incremental batch melting, in response to adiabatic decompression. Similar symbols represent increments of melt produced continuously from the same initial starting mantle. The high-Na_2O melts are the first melts produced, at the greatest pressure. The low-Na_2O melts are the last melts produced, at the shallowest pressure. The averages of all the increments produced along each of the melting paths, respectively, are shown as open symbols.

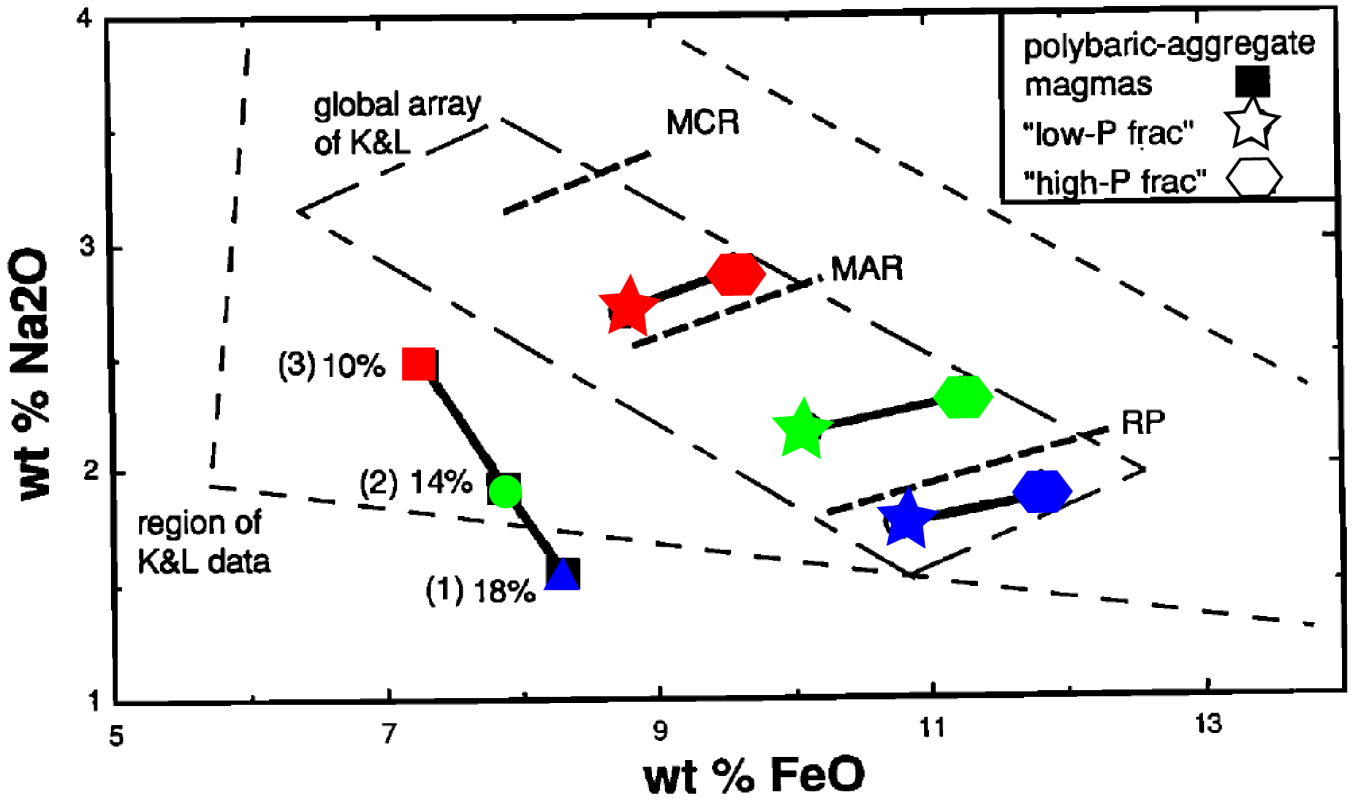

Fig. 8*a*. Weight percent Na_2O versus weight percent FeO comparing the main trend of *Klein and Langmuir* [1989, Figure 5*a*] for the global MORB data set corrected to 8.0 wt % MgO (enclosed within the dash-dotted curve) to the trend defined by the polybaric, aggregate primary magmas estimated in this study (solid curve connecting solid squares). Note that the estimated primary magmas (solid squares) are not evolved to 8.0 wt % MgO. The dashed curves contain nearly all of the global MORB data of *Klein and Langmuir* [1989]. The labels 10, 14, and 18% associated with the solid squares indicate the extent of depletion of the mantle source achieved during the polybaric, near-fractional melting process. The polybaric, aggregate primary magmas are evolved down temperature to 8.0 wt % MgO by fractionally crystallizing them at 0.001 kbar (low-*P* frac, shown by solid curve connecting open circles) and at 4 kbar (high-*P* frac, shown by solid curve connecting open triangles). The heavy dashed curves labelled MCR (mid-Cayman Rise), MAR (11.4°N-11.97°N on the Mid-Atlantic Ridge), and RP (Reykjanes Peninsula) indicate the position and slope of the local trends observed at these locations by *Klein and Langmuir* [1989, Figure 5*b*]. The heavy solid curves connecting the low-*P* frac and high-*P* frac derivative magmas yielded from each of the aggregate primary magmas indicate the potential local trend that would be produced by fractionating the same parental, aggregate primary magma over a range of pressures between 4 and 0.001 kbar.

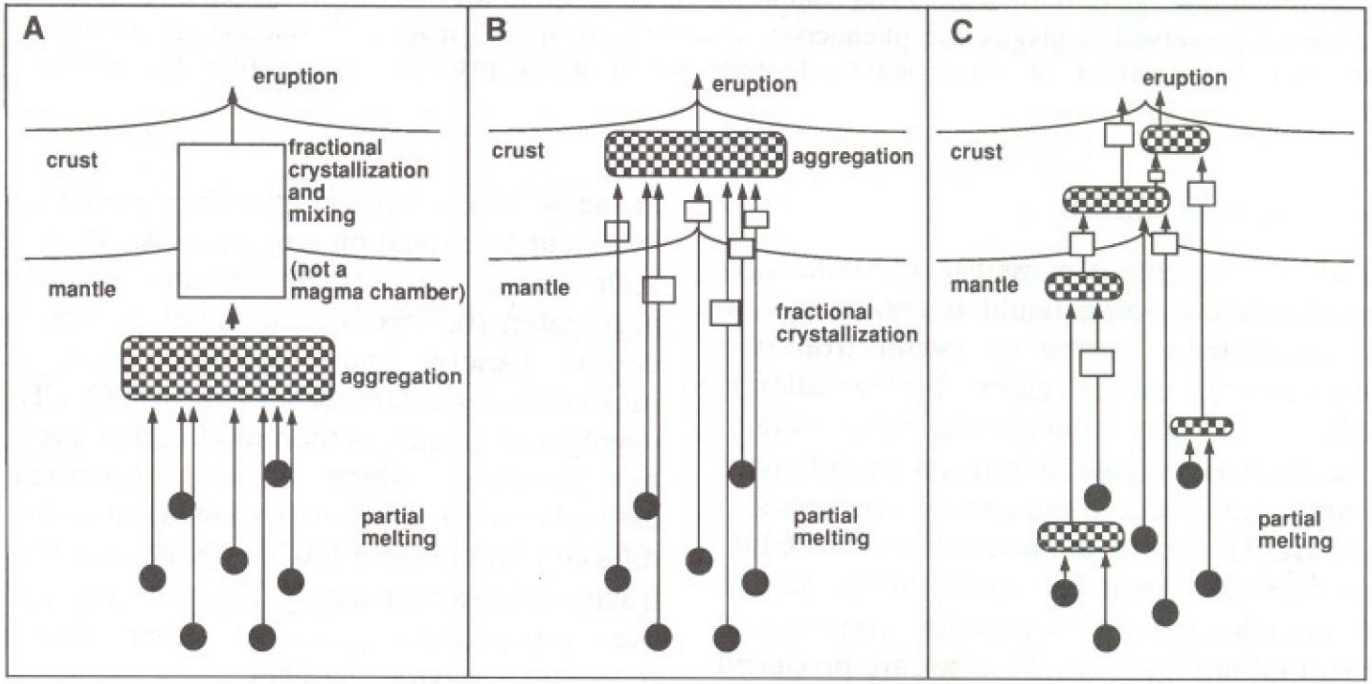

Fig. 1. Possible processes for MORB magma production and evolution. *a*) A view of MORB genesis in which melting and differentiation events are separated by an aggregation step. *b*) An extreme view in which fractional melts are produced during adiabatic ascent, the melts are segregated, moved to shallower, cooler mantle, where they are modified by differentiation before aggregation/mixing beneath the spreading center. *c*) Our preferred view of MORB genesis in which fractional melting, aggregation and differentiation occur throughout the upper mantle and the depth ranges of aggregation/mixing and differentiation overlap.

Grove (1992)

MORB: Pétrogenèse

- Crystallisation fractionee polybarique
- Fusion fractionnee polybarique
- Reaction de fusion / composition du residu
- Fusion, aggregation, cristallisation: MORB
- Influence de la compo du manteau
- Mode de transfert

La variabilité de la composition chimique des MORB influencé par la proximité des hot spots

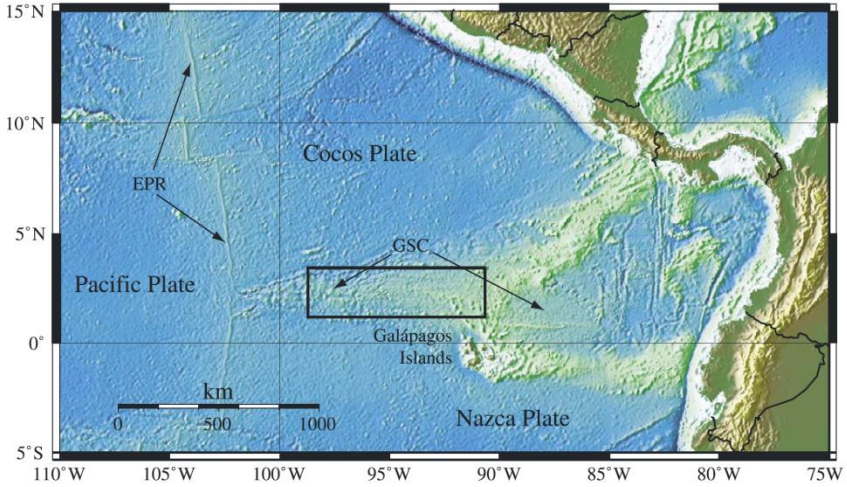

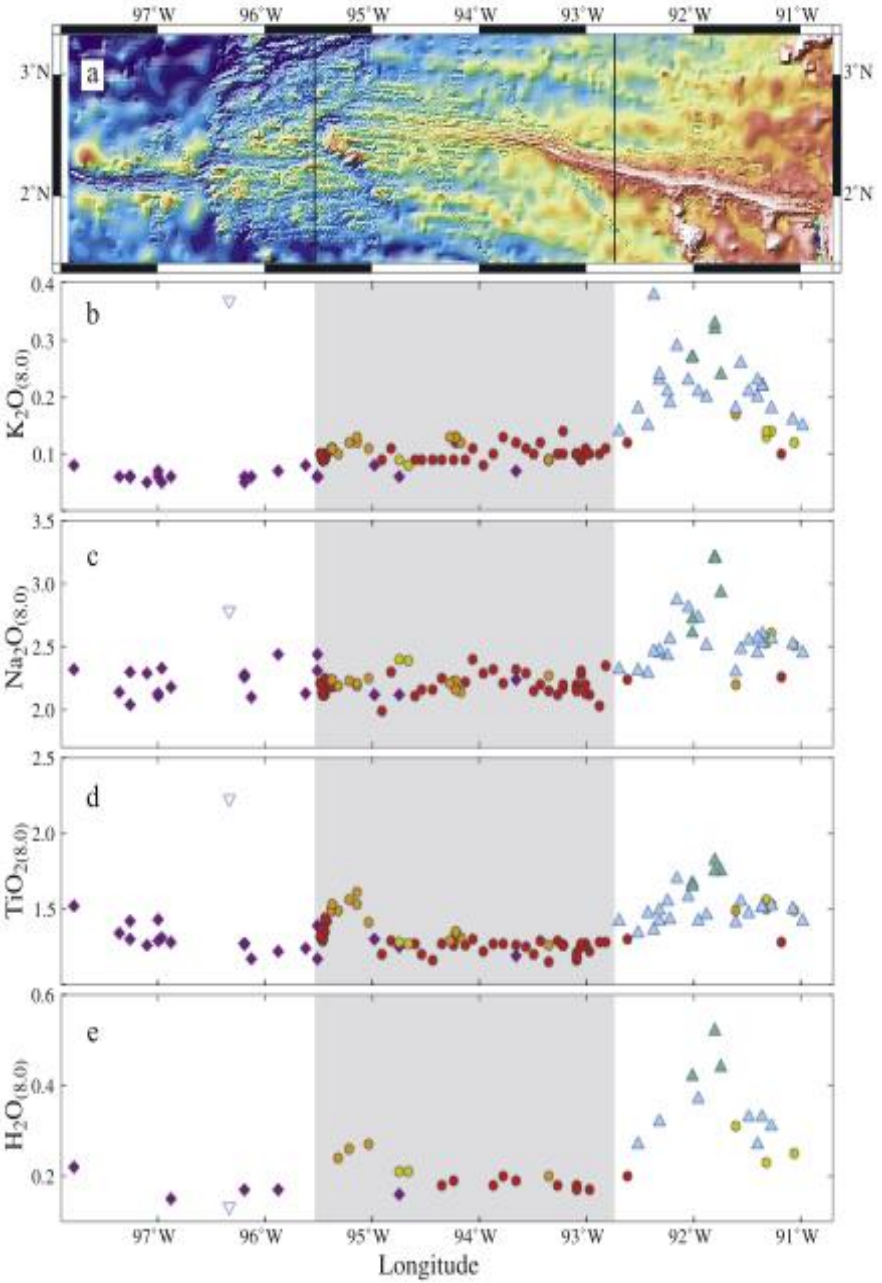

Cushman et al. (2004)

Langmuir (1992)

Composition des liquides

Fusion à 10 Kb
Différente composition

Fusion Pyrolite
Différente pression

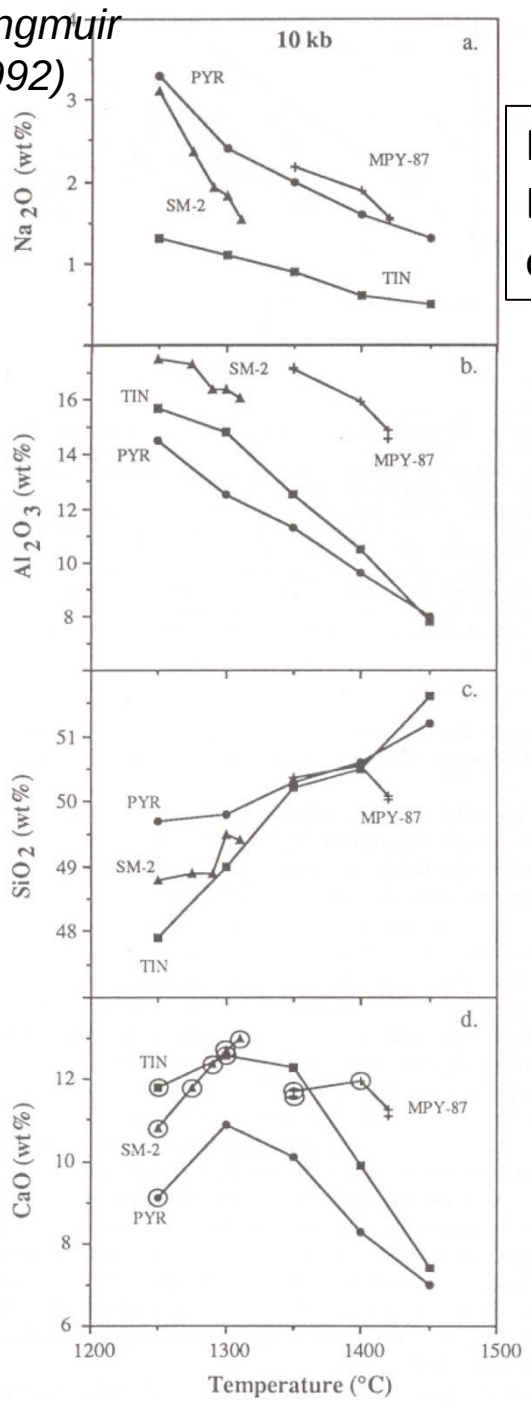

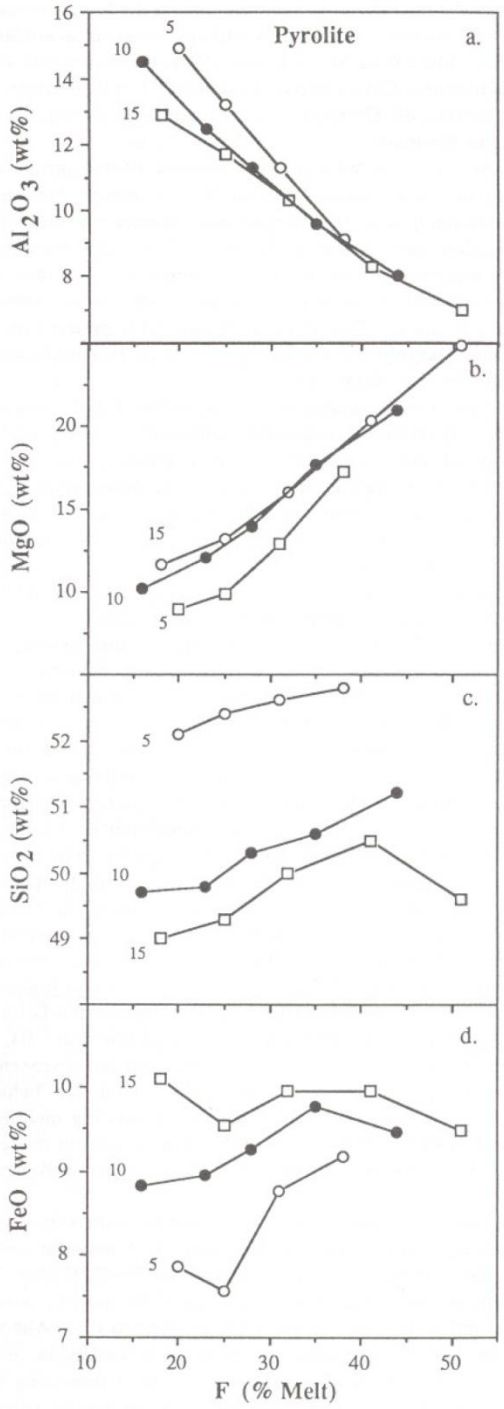

La composition des péridotites du manteau peut être modifiée par des processus de refertilisation, melt impregnation, ….

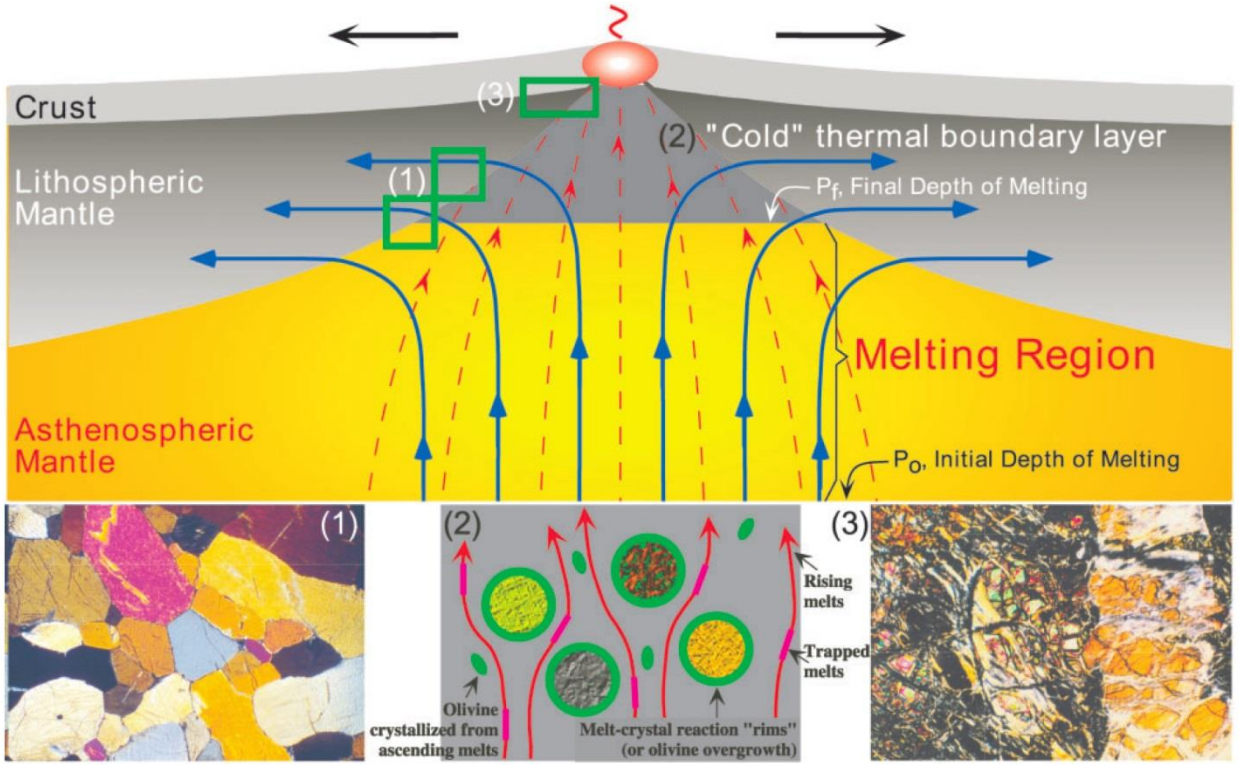

Fig. 1. A working framework for interpreting the geochemical characteristics of abyssal peridotites in the context of mantle melting, melt extraction and post-melting processes beneath mid-ocean ridges (modified from Niu, 1997). The mantle beneath an ocean ridge is conveniently considered as having two regions: the melting region between the solidus (P_o) and the depth of melting cessation (P_f) as a result of conductive cooling to the seafloor, and the cold thermal boundary layer (TBL, labeled '2') between the base of the crust and P_f. No melting occurs in the TBL, but the advanced residues continue to rise and flow laterally away from the ridge (thick arrowed lines). The newly formed melts at depth ascend, migrate through and interact with advanced residues in the TBL, including cooling-induced olivine crystallization, entrapment of melt, and complex 'chromatographic' processes. The advanced residues so processed, particularly in the central column of the TBL, continue to rise to shallow levels and are variably serpentinized (labeled '3') before they are tectonically exposed and sampled on the seafloor as abyssal peridotites. On the other hand, melting residues at deep levels (labeled '1') that turn laterally will not experience the TBL processes, never be serpentinized, and never be sampled as abyssal peridotites, but may be sampled as fresh ophiolitic or massif peridotites in the geological record (e.g. Frey *et al.*, 1985; Godard *et al.*, 2000; Griselin & Davies, 2003).

Niu (2004)

MORB: Pétrogenèse

- Crystallisation fractionee polybarique
- Fusion fractionnee polybarique
- Reaction de fusion / composition du residu
- Fusion, aggregation, cristallisation: MORB
- Influence de la compo du manteau
- Mode de transfert

Kelemen, 1995, Nature

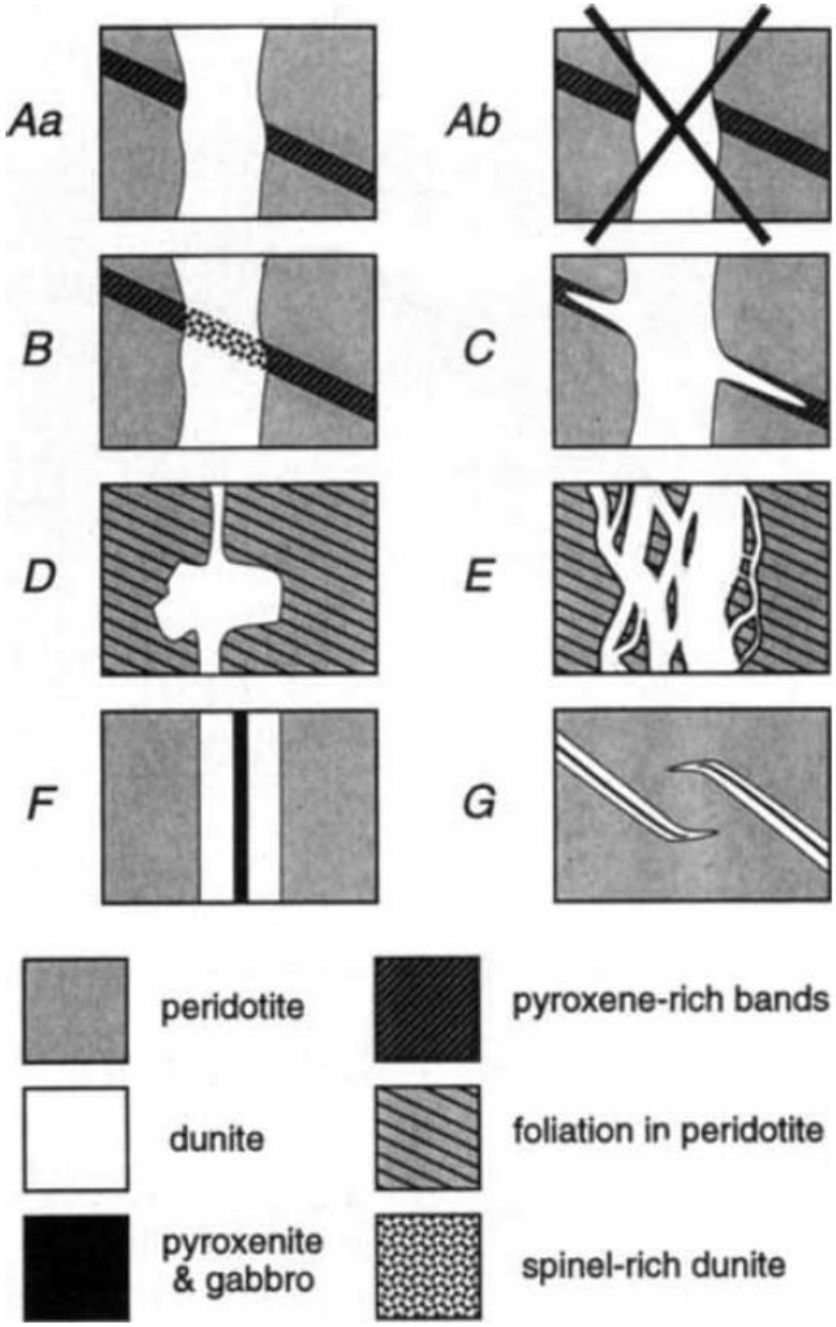

FIG. 2 Summary of contact relationships of dunites in the mantle section of ophiolites. For specific examples and additional references, see refs 11, 12, 15, 17–26, 31–34, 46, 50, 52 and 53. We interpret the relations illustrated in *A–E* to indicate a replacive origin for dunites, involving dissolution of pyroxene and precipitation of olivine (±spinel) by liquid migrating by porous flow. Dunites with contact relations as illustrated in *F* and *G* are probably replacive, but may have formed in porous reaction zones around melt-filled fractures. *A*, Dunite that cross-cuts pyroxene-rich bands in peridotite does not displace the bands, as in *Aa*. If dunites were dykes filled with olivine, bands in the wall rock would be displaced, as in *Ab*. *B*, Relict trains of spinel where dunite cross-cuts pyroxene-rich bands. Some spinel is present in the original bands; additional spinel may be precipitated during incongruent dissolution of pyroxene. *C*, Locally, pyroxene-rich bands are selectively replaced by dunite without evidence for dilation by dyke injection. *D*, Widening features, where narrow dunites enter and leave a larger, rounded region, do not show dilation of foliation in surrounding peridotite. *E*, Anastamosing dunite includes 'islands' of relict peridotite which have not been rotated or displaced relative to the surrounding peridotite. *F*, Medial pyroxenite and/or gabbro is observed in some tabular dunite bodies. *G*, Curving tips in tabular dunite with medial pyroxenite, observed in the Trinity peridotite (A. Rubin, personal communication), suggest that these dunites formed in a porous reaction zone around and ahead of propagating fractures.

Transport ?

Nicolas, 1986

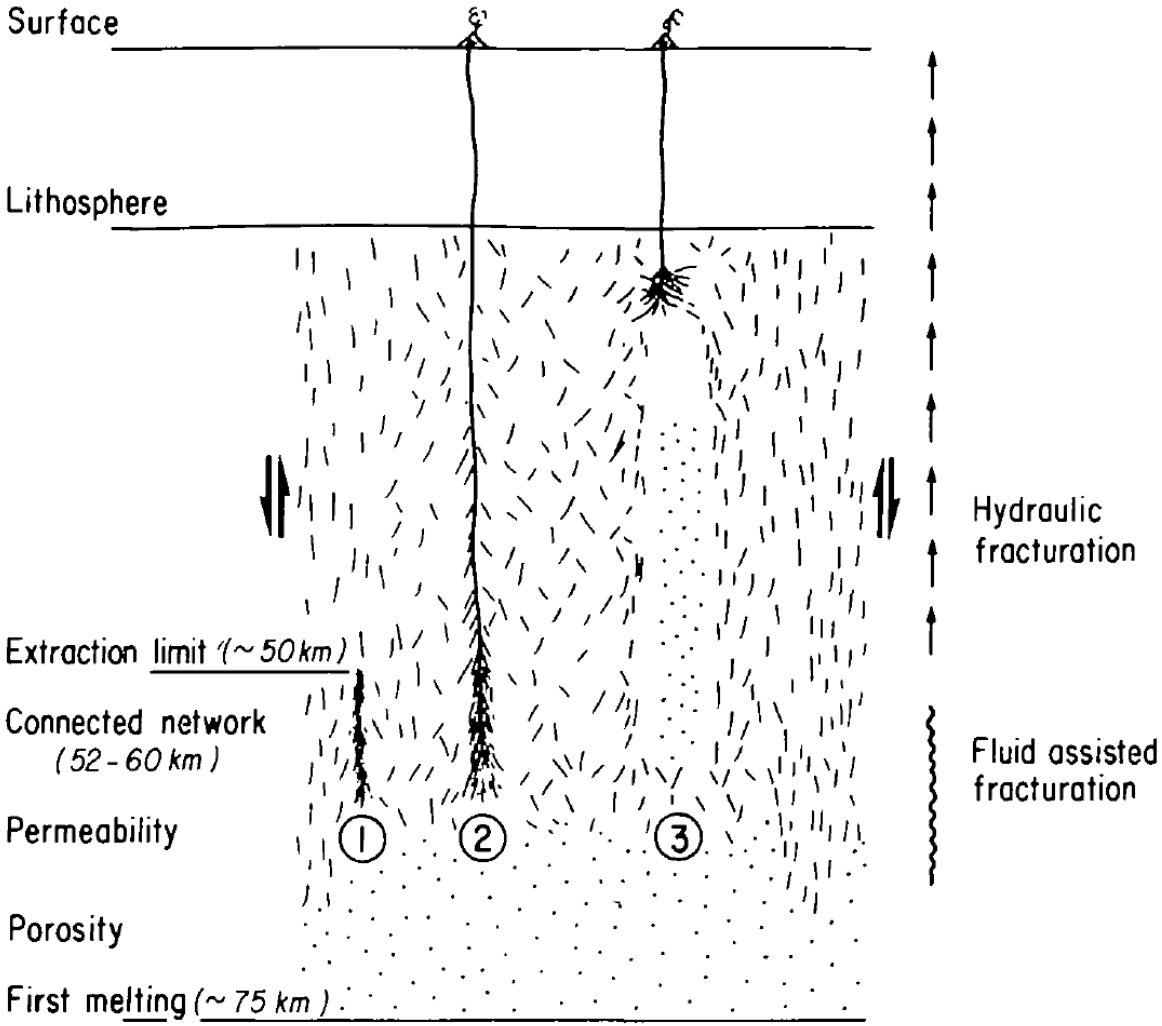

FIG. 5. Model of melt extraction in a mantle diapir. Dots: isolated melt drops; dashes: melt veins and gashes. The melt conduits (full lines) follow the $\sigma 1$ trajectories which are not necessarily vertical. (1), (2) and (3): successive stages of melt extraction. (1) creation of a connected melt network on the critical vertical extension; (2) newly formed melt conduit, draining melts mainly from deep horizons; (3) dying melt conduit draining shallow melts and leaving a wake of depleted peridotites. The (1), (2), (3) sequence is periodically achieved in the various parts of the diapir.

Nicolas, 1986

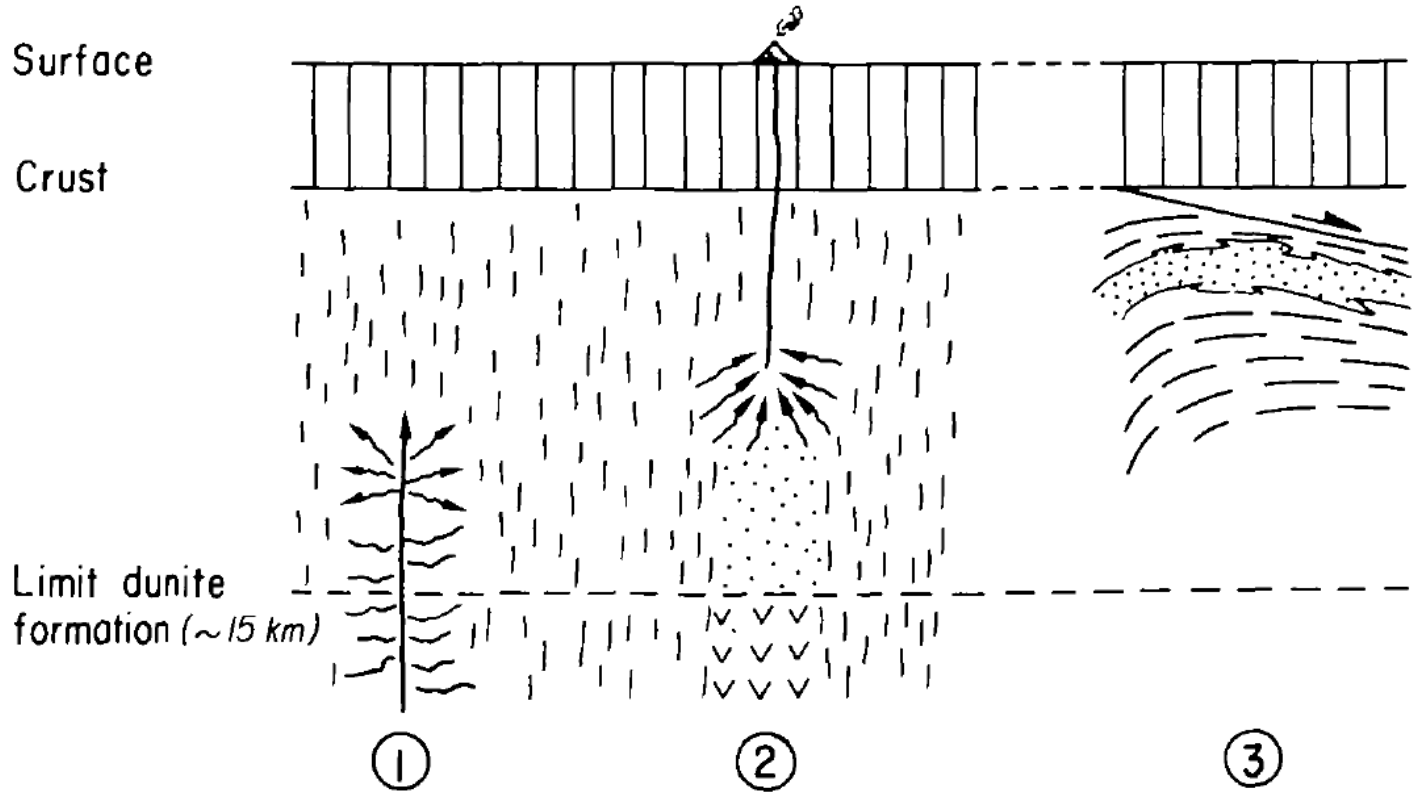

FIG. 7. Dunite origin. (1) Incoming in the opx-incongruent melting field of a melt conduit, opening its way by hydrofracturing and whose melt impregnates the local connected melt network. (2) Melt drainage in the zone of melt impregnation, leaving harzburgites and dunites (respectively, vs. and dots) as residue. (3) Drifting away from the ridge of a tectonically rotating dunite lens. The vertical orientation of the melt conduit is arbitrary; it should follow the $\sigma 1$ trajectory which may be inclined; the dunite bodies are not at the scale.

Braun & Kelemen 2002

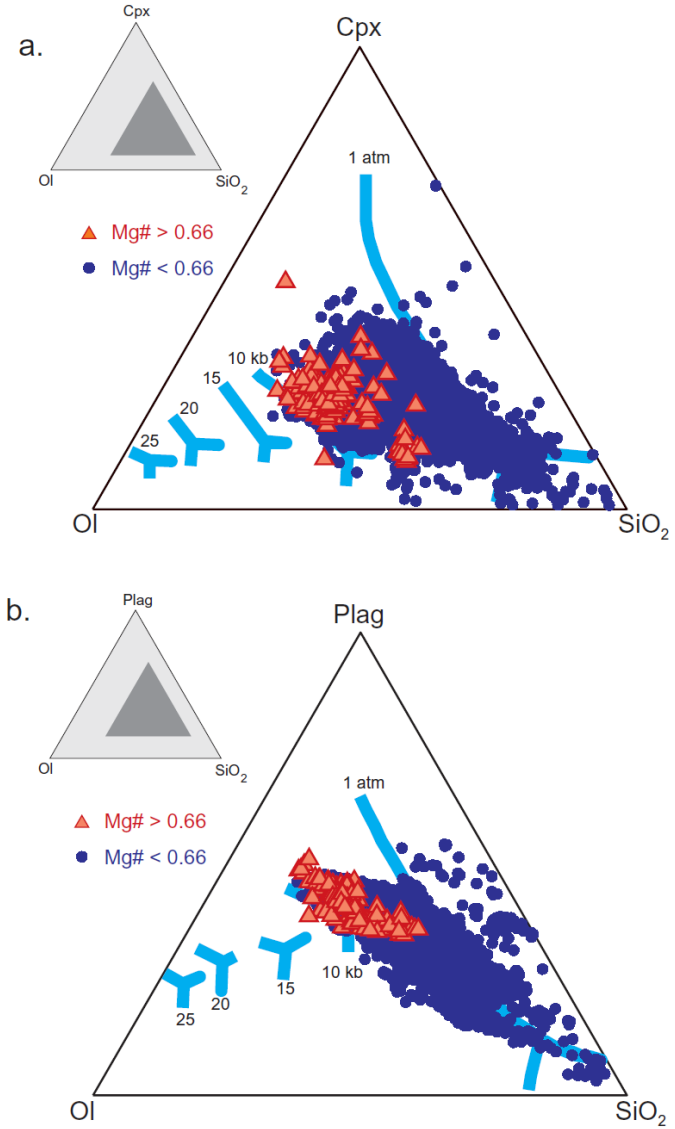

Figure 1. Pressures of equilibration of ~10,000 MORB glasses (circles) as inferred from pseudo-ternary phase diagrams projected from (a) plagioclase and (b) clinopyroxene [after *Elthon*, 1983]. Primitive MORB liquids (triangles), defined by Mg# (Mg/Mg + Fe) in excess of 0.66, were last saturated in orthopyroxene at pressures greater than 10 kb, suggesting these liquids passed through the upper 25–30 km of the mantle without reacting with the surrounding harzburgite. Glass compositions for this global compilation are from the RIDGE PetDB database (http://petdb.ldeo.columbia.edu). The positions of the cotectic lines at all pressures (1 bar - 25kb) are taken from *Elthon* [1983].

Kelemen, 1995, Nature

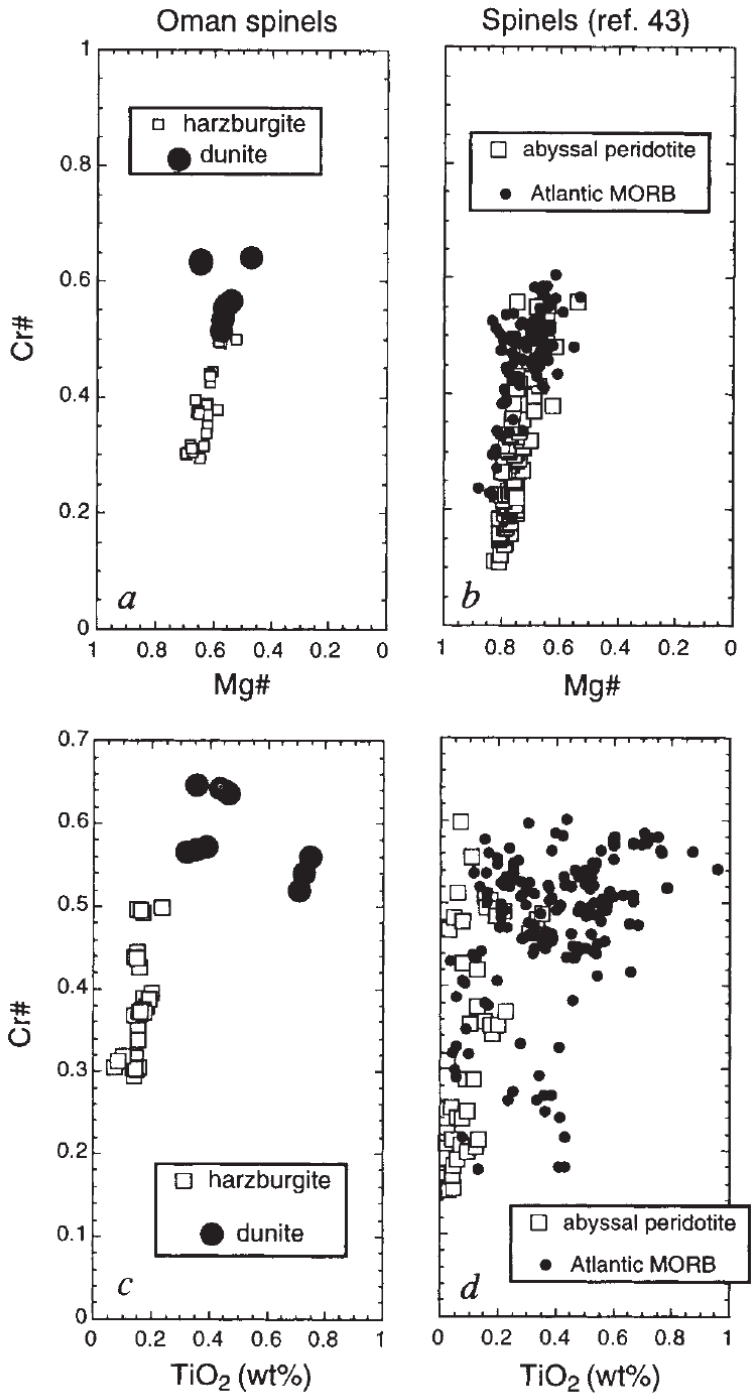

Evidence cogenetique spinels de dunite et spinels de MORB

Theorie d'un système ouvert

Kelemen, 1995, JGR

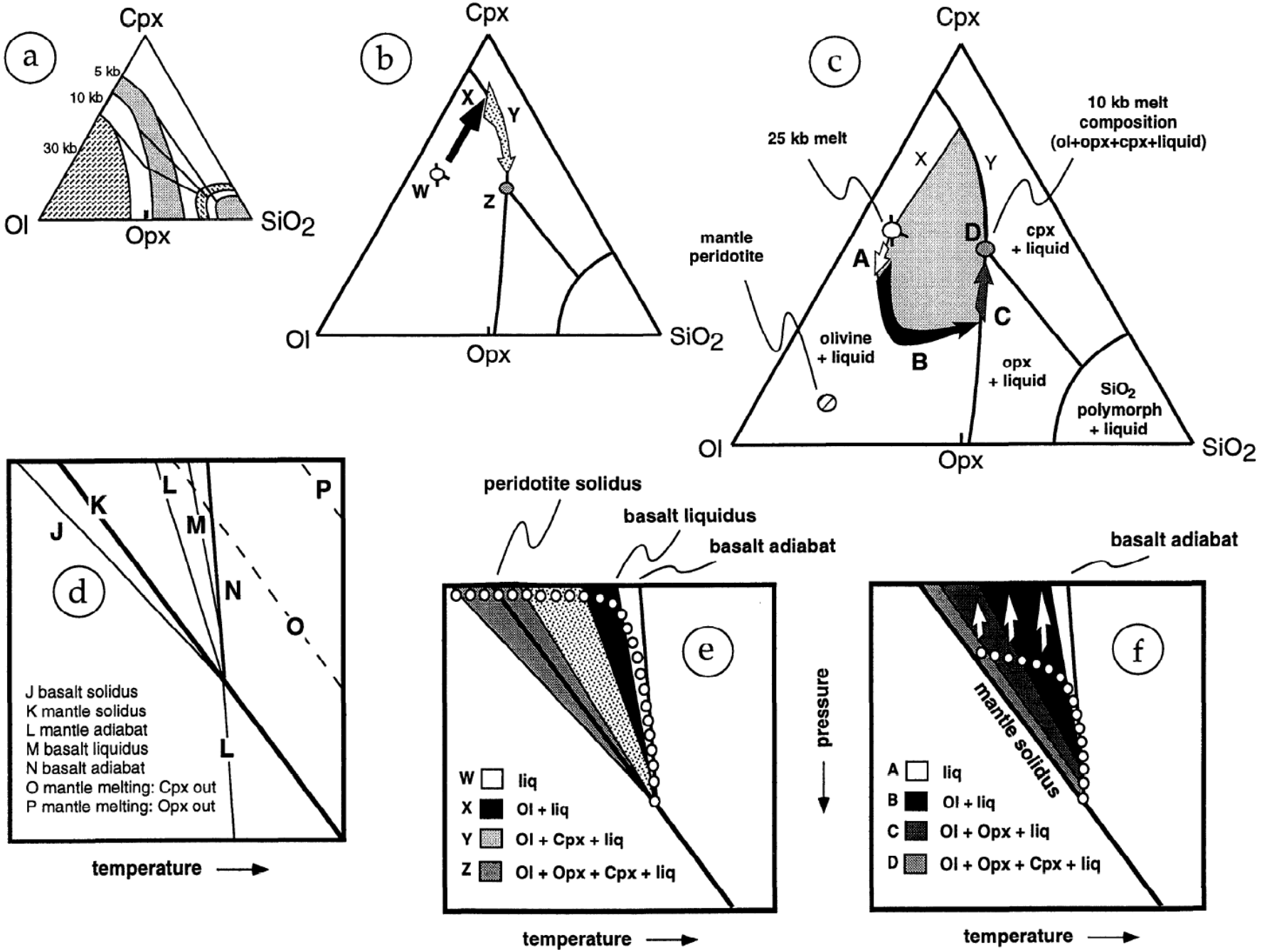

Figure 2. Liquid and solid products of reaction between ascending melts and surrounding upper mantle wall rocks are illustrated in these diagrams. At the top are three schematic, pseudo-ternary phase diagrams on the plane olivine (Ol) - clinopyroxene (Cpx) - silica (SiO_2), projected from spinel, for hydrous silicate liquids at upper mantle pressures [*Kelemen et al.*, 1992]. (a) The effect of pressure in this system. Decreasing pressure leads to increased stability of Ol relative to pyroxenes, so that liquids in equilibrium with Ol, Cpx, and Opx at a high pressure will be saturated only in Ol during cooling at a lower pressure. (b) The effect of decompression from 2 to 0.5 GPa, cooling, and closed-system, crystal fractionation upon a picritic (high Mg basalt) liquid formed by a small degree of partial melting of mantle lherzolite at 2 GPa. The adiabatically ascending liquid at point W is initially undersaturated in solids. As it cools and diverges from an adiabatic PT path, it saturates first in Ol. Fractionation of Ol drives the liquid to saturation in Cpx along the vector labeled X, after which coprecipitation of Ol + Cpx, and reaction between liquid and Ol producing Cpx, drives the liquid along the vector labeled Y. Finally, saturation in Opx is reached at point Z. The liquid composition at Z will be substantially different from a partial melt of lherzolite at 0.5 GPa, having a lower Mg/Fe ratio and lower Ni and Cr contents than a mantle melt. (c) Reaction at 2 to 0.5 GPa between mantle lherzolite and the same picritic liquid as in Figure 2b. The peridotite reactant is just at its solidus temperature at 0.5 GPa. Liquid rising adiabatically is above its liquidus temperature. For this reason, along path A, the melt initially dissolves peridotite. This leads to olivine saturation in the liquid, which will crystallize Ol, and continue to dissolve pyroxene. One possible liquid path is shown as the vector labeled B; this is for relatively rapid reaction and slow cooling, during which liquid mass increases. More rapid cooling, or slower pyroxene dissolution, would produce derivative liquid compositions within the shaded region bounded by B, C, X, and Y. Eventually, path B leads to saturation of the melt in Opx as well as Ol. Continued reaction and cooling will consume Cpx and a small amount of Ol from peridotite reactants, producing decreasing liquid mass, Opx + Ol solid assemblages, and derivative liquids along path C. Finally, at D, the liquid will become saturated in Cpx. The liquid composition at point D will be similar in major element composition(Mg/Fe, Ni, Cr, SiO_2) to a small degree melt of mantle lherzolite at 0.5 GPa, although its trace element characteristics may preserve a "memory" of its open system provenance. At bottom are PT plots summarizing the composition of liquid and solid products of the polybaric crystallization and reaction processes illustrated above. (d) General features of adiabatic ascent paths for solids and liquids in the mantle, relative to the slope of the mantle solidus and the saturation surface for olivine in mantle-derived liquids [e.g., *Yoder*, 1976; *McKenzie and Bickle*, 1988]. If liquid ascends to the surface along an adiabatic PT path in a closed system, it will remain undersaturated in solids, retaining the composition of a partial melt of mantle peridotite at high pressure. If it ascends in an open system, it will be capable of dissolving solid phases from surrounding peridotite, resulting in a net increase in liquid mass. Where it cools to temperatures lower than along the adiabatic ascent path, it will saturate first in Ol. Adiabatically ascending mantle peridotite follows a less steep PT path, due to the energy requirements of fusion during ascent. The lherzolite solidus has a much shallower PT slope than adiabatic ascent paths. Ascending mantle lherzolite will gradually generate partial melt, consuming pyroxene as it does so. Cpx is generally not completely consumed by closed system partial melting during adiabatic ascent beneath mid-ocean ridges [e.g., *Dick et al.*, 1984]. By contrast, reaction with ascending liquid can completely dissolve all pyroxene from lherzolite. (e) Products of the polybaric, closed system crystal fractionation path illustrated in Figure 2b. Liquid mass remains constant over the adiabatic portion of the ascent path, then decreases during conductive cooling. (f) Products of the polybaric reaction process illustrated in Figure 2c. Liquid mass increases during the initial portion of the ascent path in which the liquid is under-saturated in solids and also over part of the path in which the liquid is saturated only in olivine. As the liquid continues to cool, liquid mass begins to decrease, and the liquid becomes saturated in pyroxene as well as olivine.

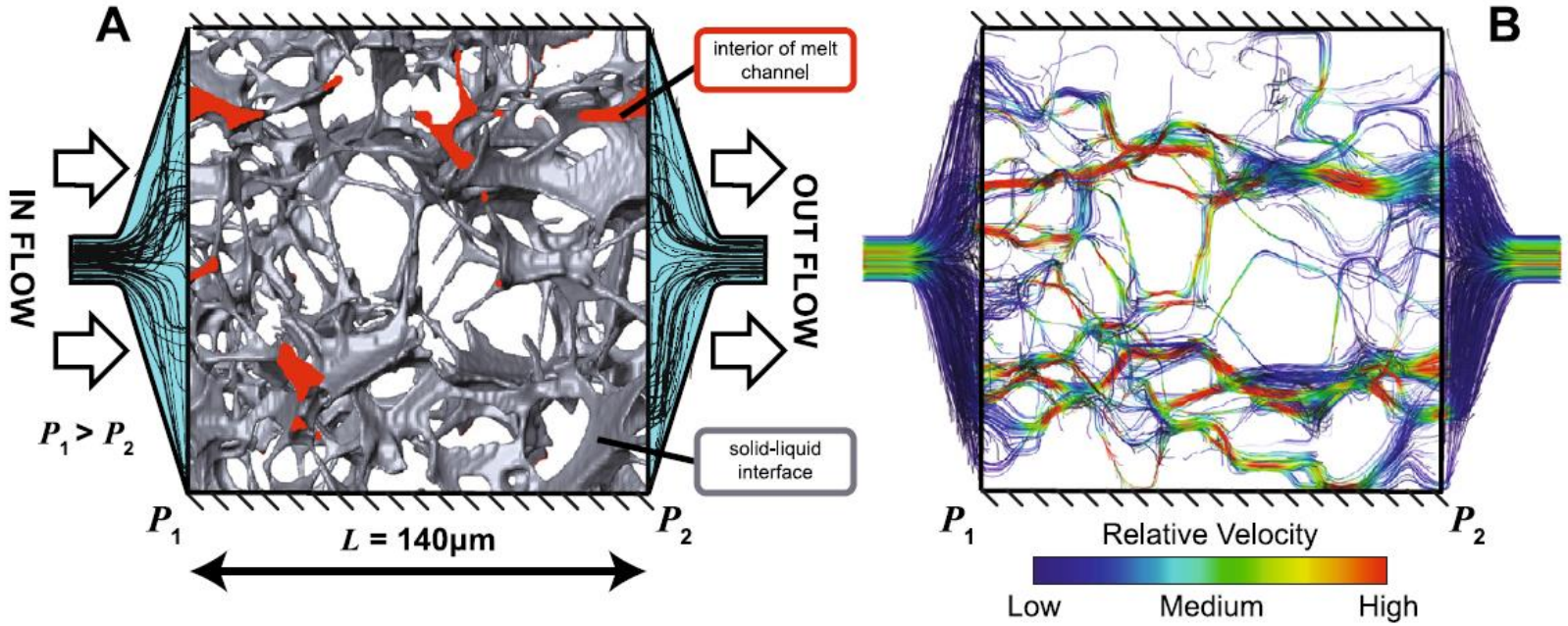

Les liquides formés sont extraits pour un seuil de perméabilité de ~ 3-7%

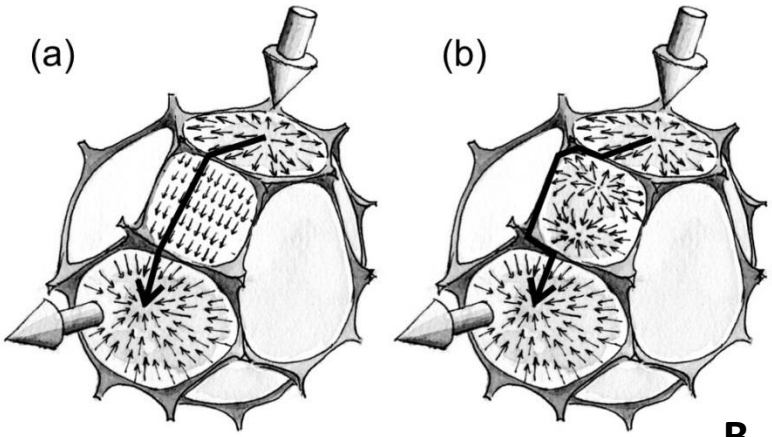

B. Holtzman

Hypotheses for Dunite Formation

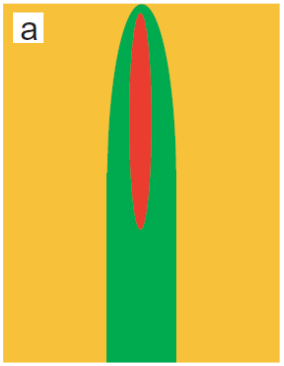

Reaction Zones around
Melt Filled Hydrofractures

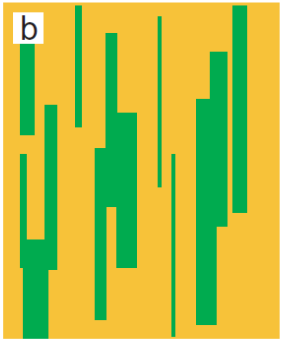

Random Merging of
Growing Reaction Zones

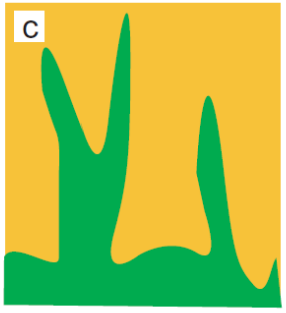

Porous Flow Channels
Formed by Dissolution Instability

Braun & Kelemen 2002

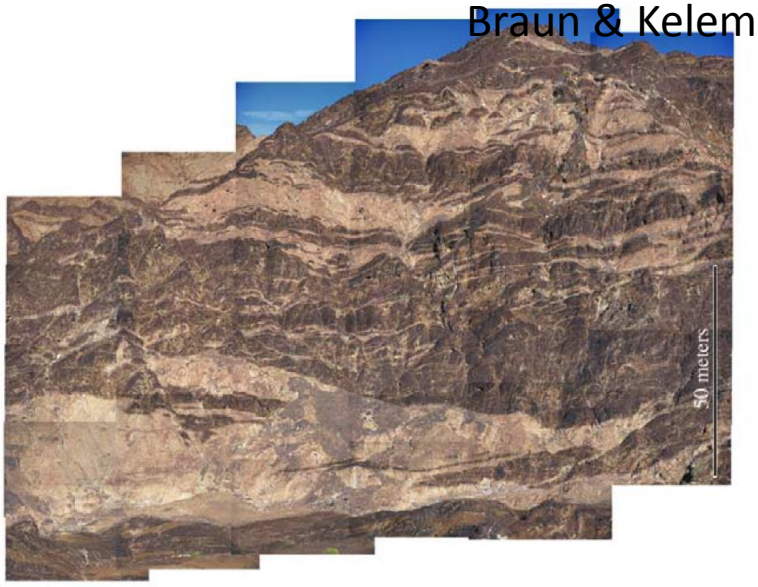

Figure 5. Photomosaic of a mountainside in the Muscat Massif. As at all scales, dunite orientations measured across the image area are used to correct dunite widths as measured from the image mosaic. The lighter rocks are dunite, the darker are harzburgites. The two geologists in the center of the image are standing ~50 m apart.

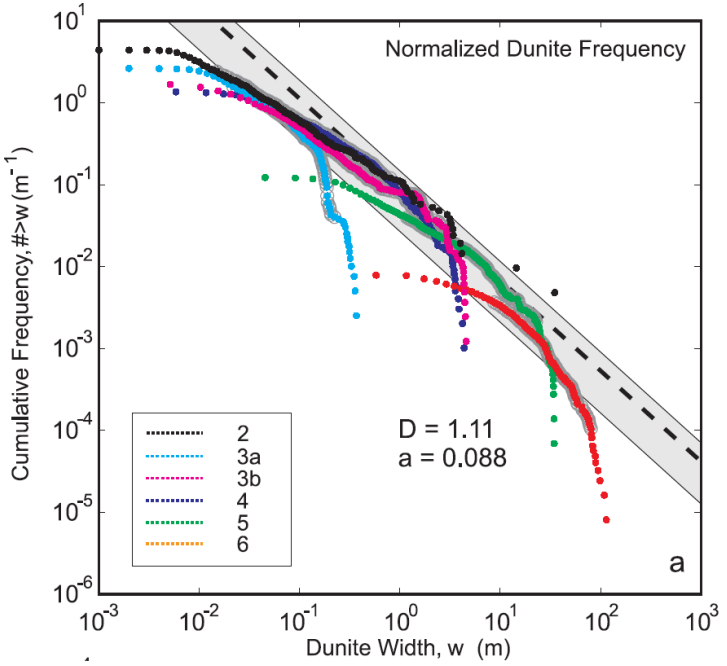

Einat's Castle

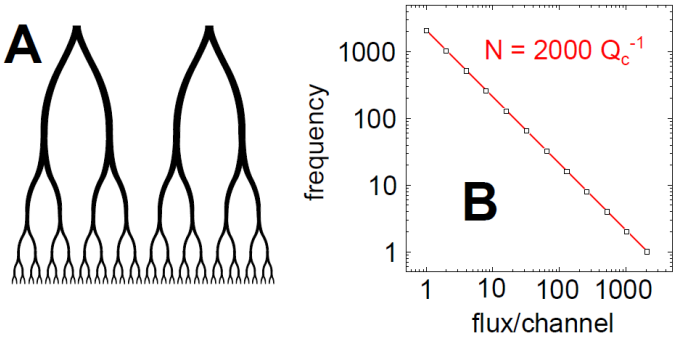

numerical results

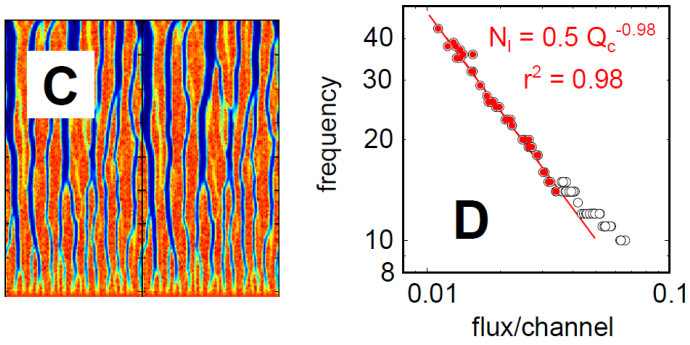

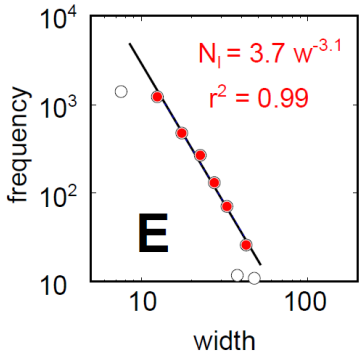

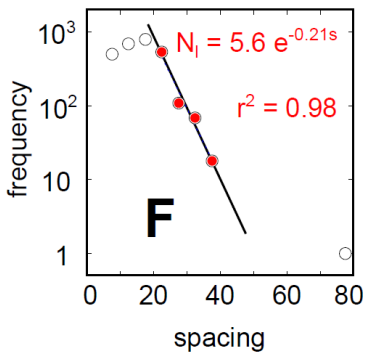

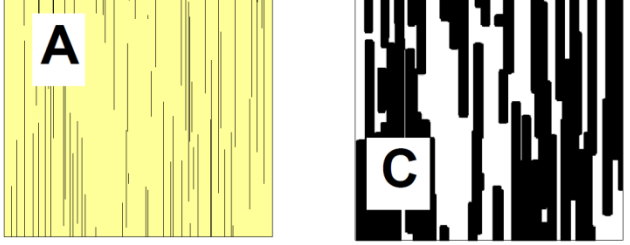

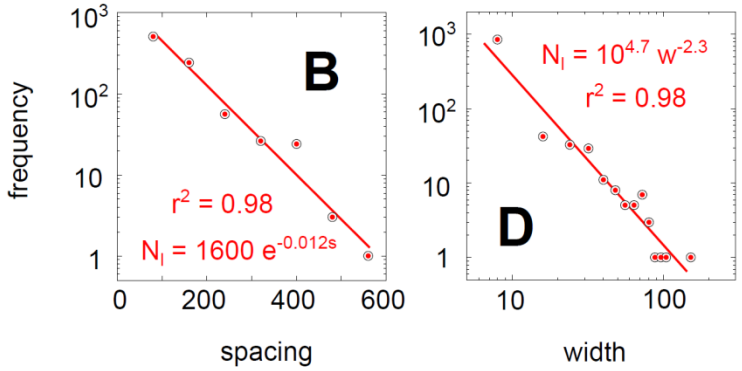

Figure 6. Results of a simple model of reaction zones around parallel cracks. (A and B) Randomly spaced, parallel cracks, and their spacing statistics; (C) reaction zone distribution after 15× widening of initial, 1 pixel wide "reaction zones"; (D) size/frequency statistics when reaction zones occupy 80% of a model space

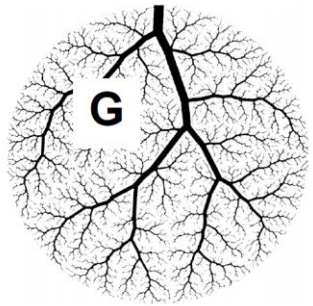

synthetic branching network

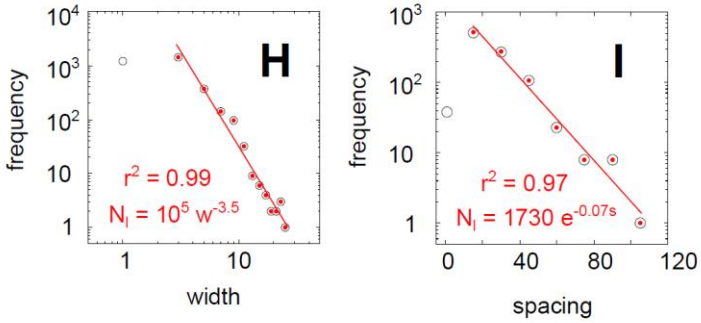

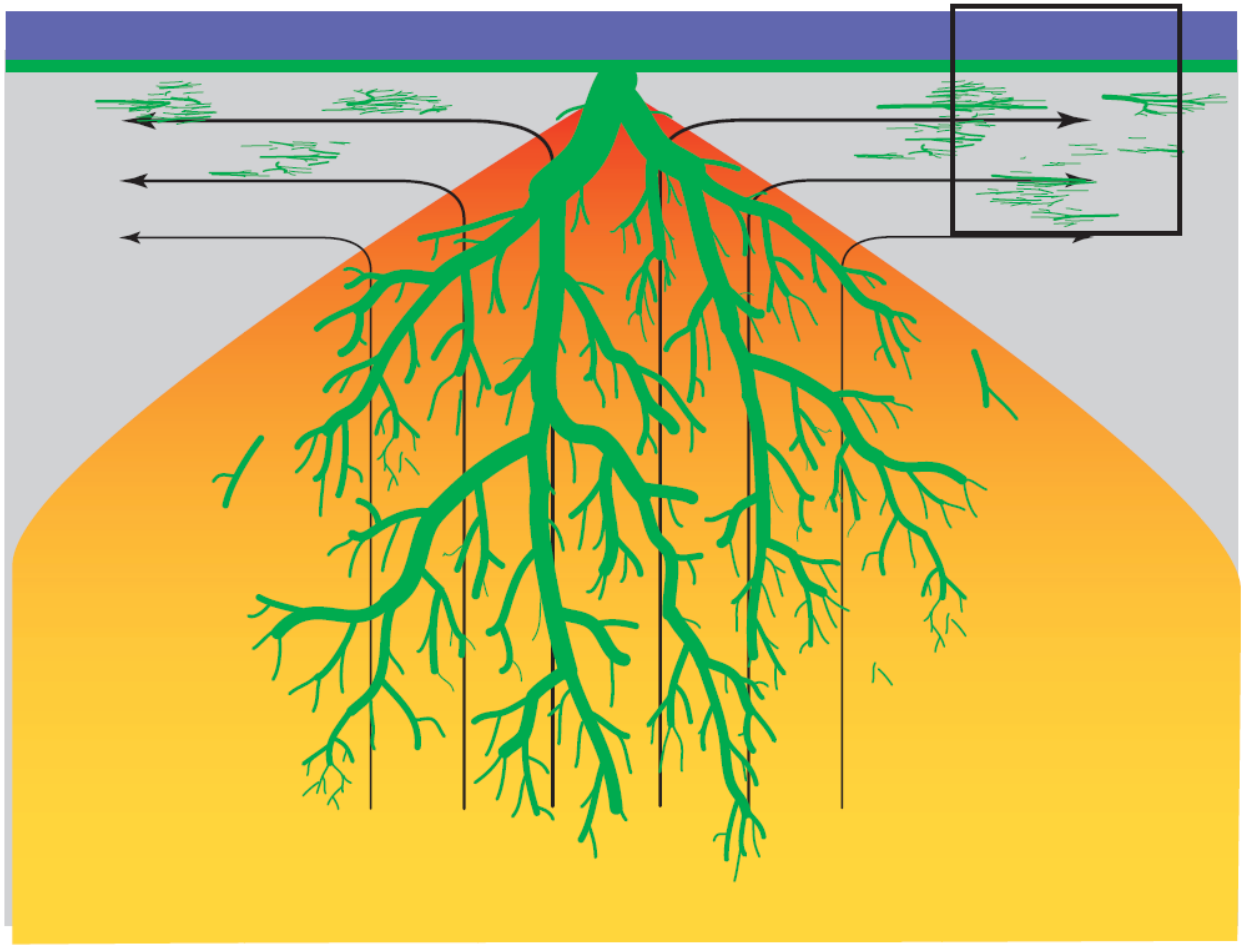

Figure 16. Schematic illustration of a coalescing dunite network beneath an oceanic spreading center based on observations in the Oman Ophiolite. Dunites are shown in green, the crust in blue, and melt is presumed to be present throughout the red and yellow region. The box in the upper right corner indicates the scale of the lithologic section preserved in Oman. The preserved dunites may have been thinned, for example, via simple shear, during transposition resulting from corner flow. We have implicitly assumed that this thinning affected all dunite widths by the same percentage. Thinning in this manner would affect the magnitudes of the dunite widths but not change the ratio of smaller dunites to larger ones. Therefore the power law slope would remain unaffected.

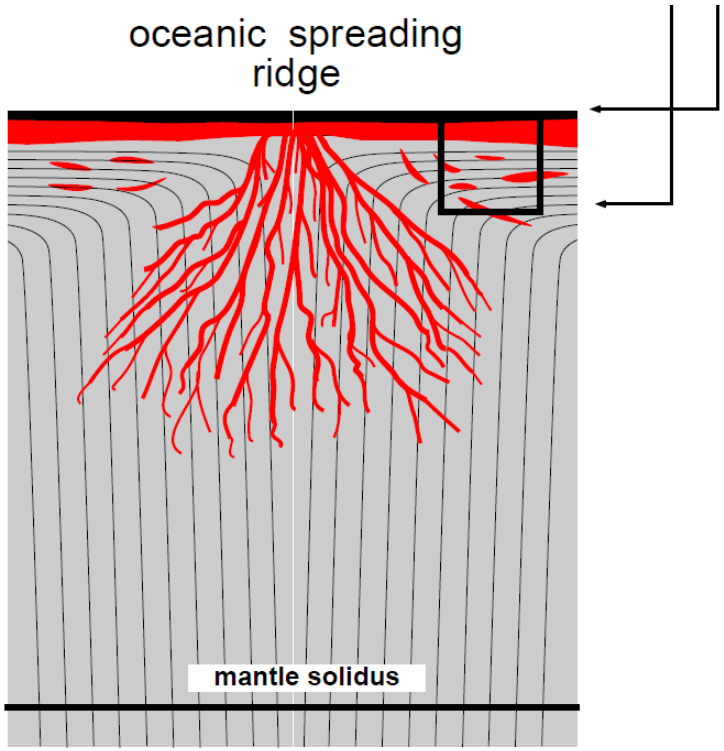
oceanic spreading ridge
mantle solidus

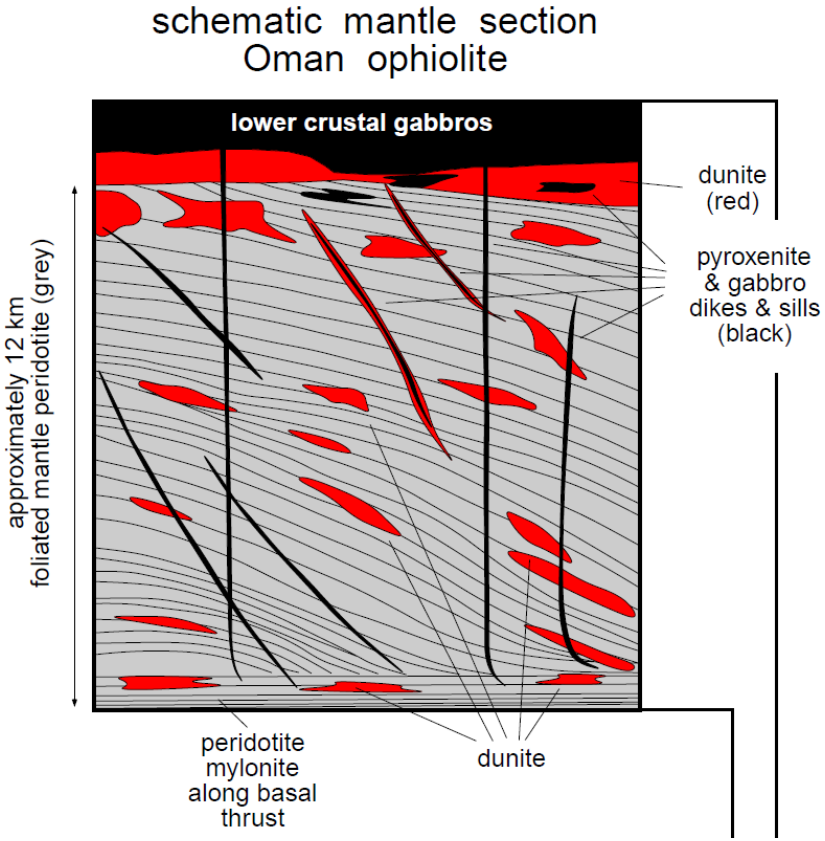
schematic mantle section
Oman ophiolite
lower crustal gabbros
dunite (red)
pyroxenite & gabbro dikes & sills (black)
approximately 12 km foliated mantle peridotite (grey)
peridotite mylonite along basal thrust
dunite

Transport dans la croute

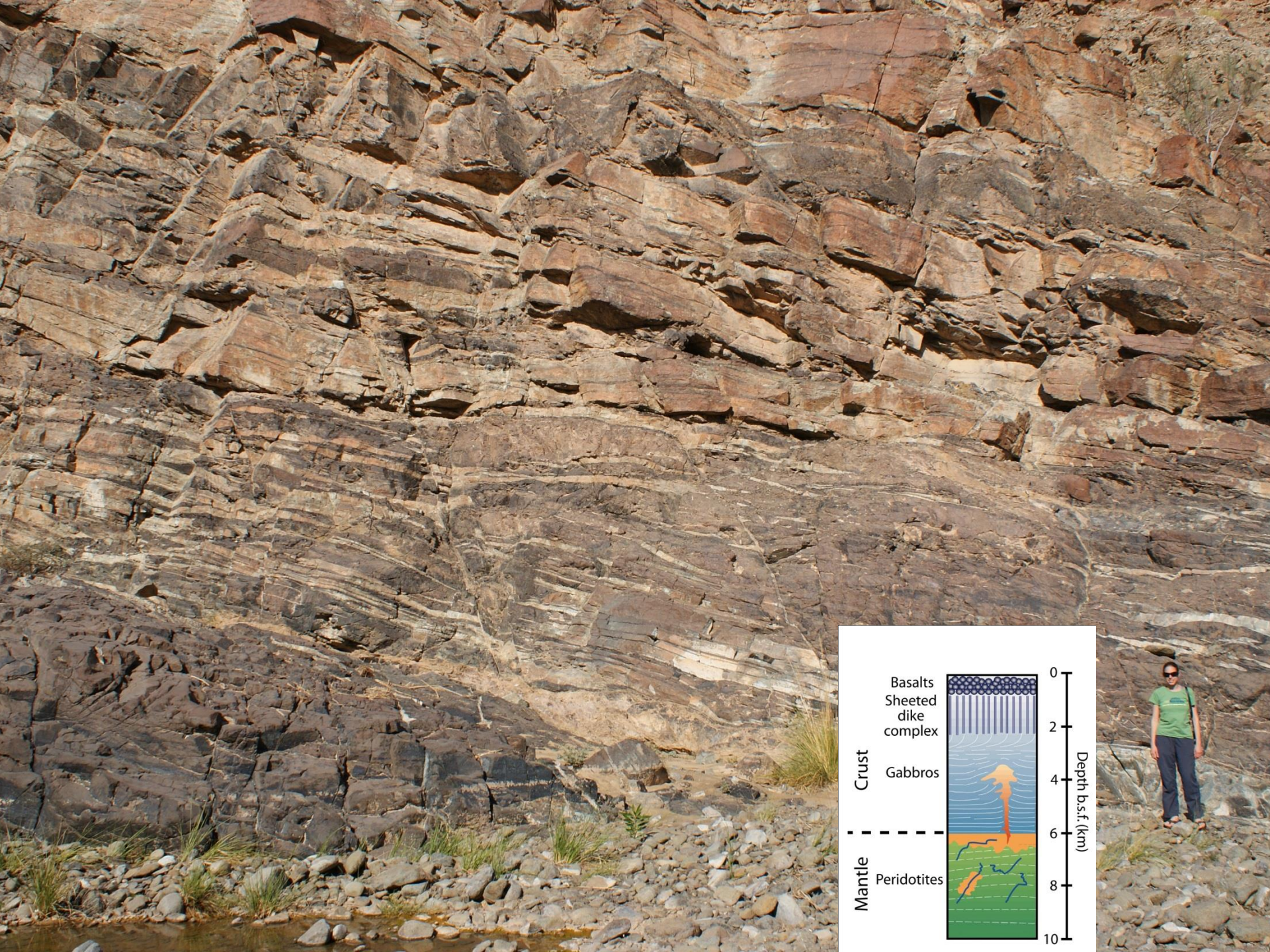
Basalts
Sheeted dike complex
Gabbros
Peridotites
Crust
Mantle
0
2
4
6
8
10
Depth b.s.f. (km)

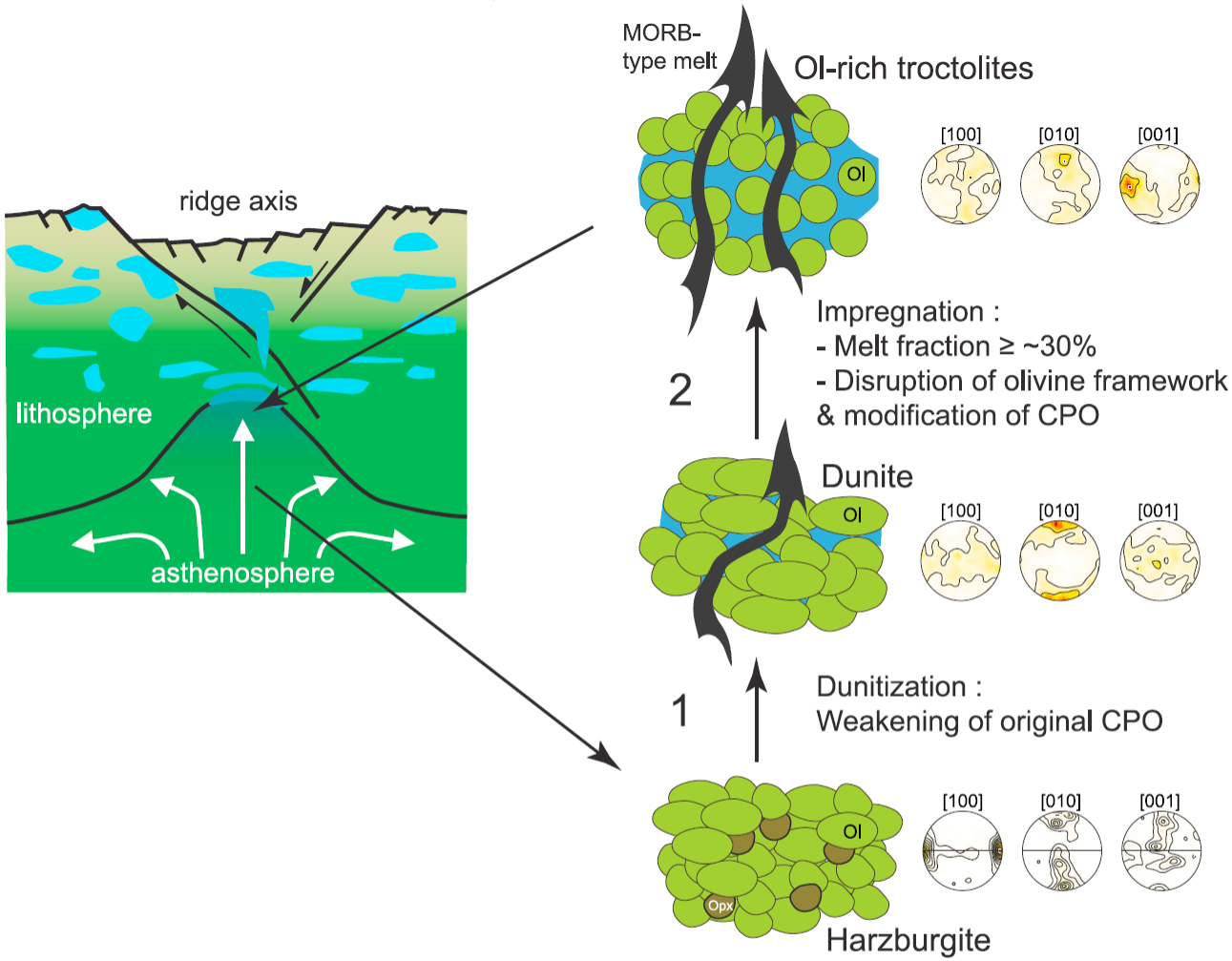

Figure 8. Sketch of the proposed scenario for the formation of Hole U1309D olivine-rich troctolites. Percolation of basaltic melts through depleted mantle peridotite at near solidus temperature results in dunitization (orthopyroxene dissolution, precipitation of olivine, and formation of dunite), with weakening of olivine CPO (indicated by 1), and impregnation when increasing melt fraction (≥30%) locally disrupts the olivine framework and further modifies the olivine CPO (indicated by 2). The dunitization and impregnation are viewed as successive stages of a continuous process. As temperature decreases, melt crystallizes plagioclase and clinopyroxene within the assimilated olivine matrix to form olivine-rich troctolite. The schematic cross section of the ridge axis is modified from *Cannat* [1996]. The examples of original harzburgite and dunite CPOs are from Polynesian xenoliths (RPA18A and UAH280X, respectively [*Tommasi et al.*, 2004]). Note the absence of structural reference frame (no visible foliation in samples) for the dunite and olivine-rich troctolite CPOs.

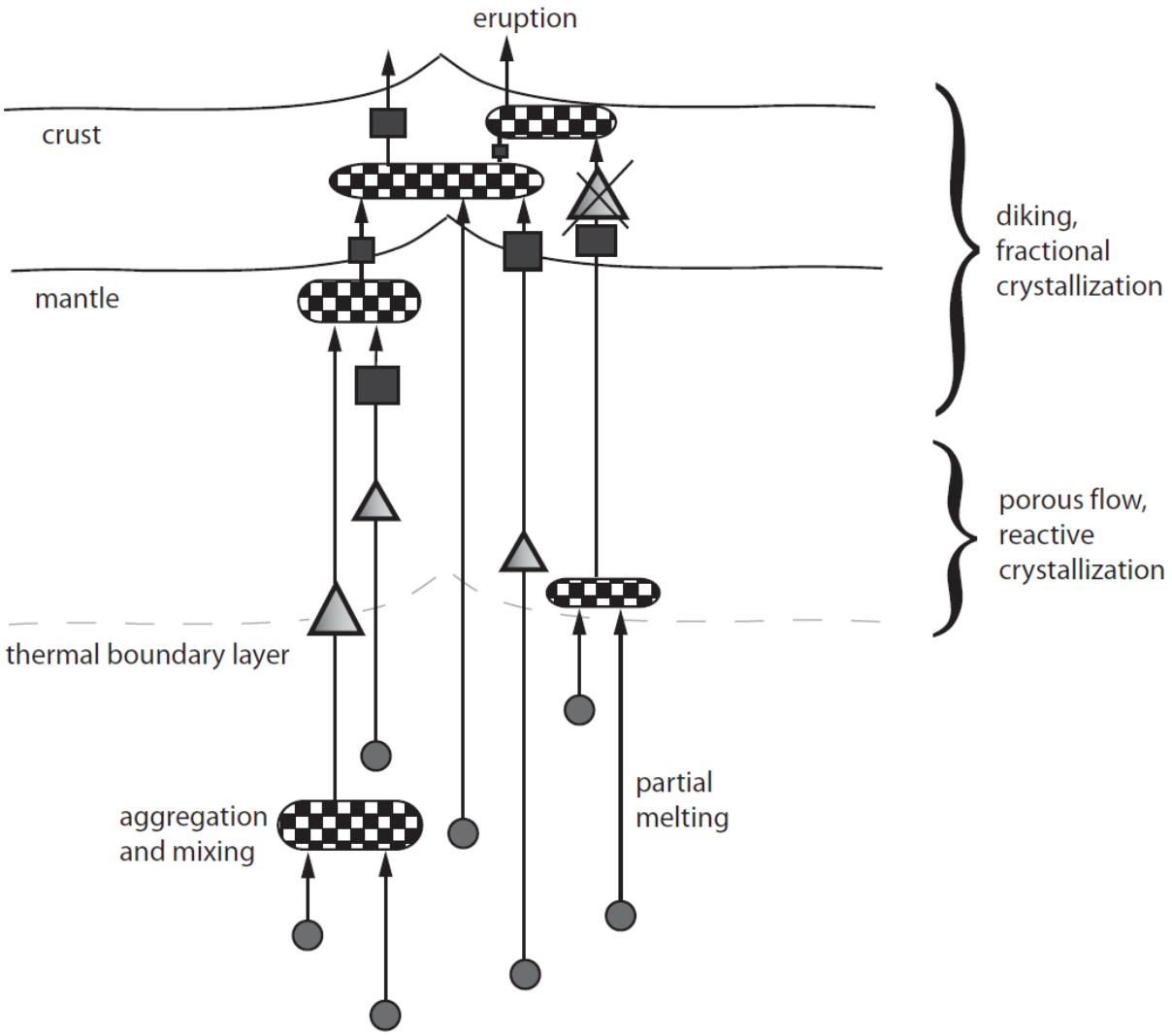

Fig. 14. Summary diagram, modified after Grove *et al.* (1992), illustrating the likely role for reactive crystallization in MORB genesis. Circles represent local fractional melts, checkered fields indicate magma aggregation, triangles symbolize depths of reactive crystallization, and squares represent depths of fractional crystallization. Also shown are the thickness of the thermal boundary layer and the igneous crust above the Moho.


Basalts
Sheeted dike complex
Gabbros
Crust
Mantle
Peridotites
0
2
4
6
8
10
Depth b.s.f. (km)

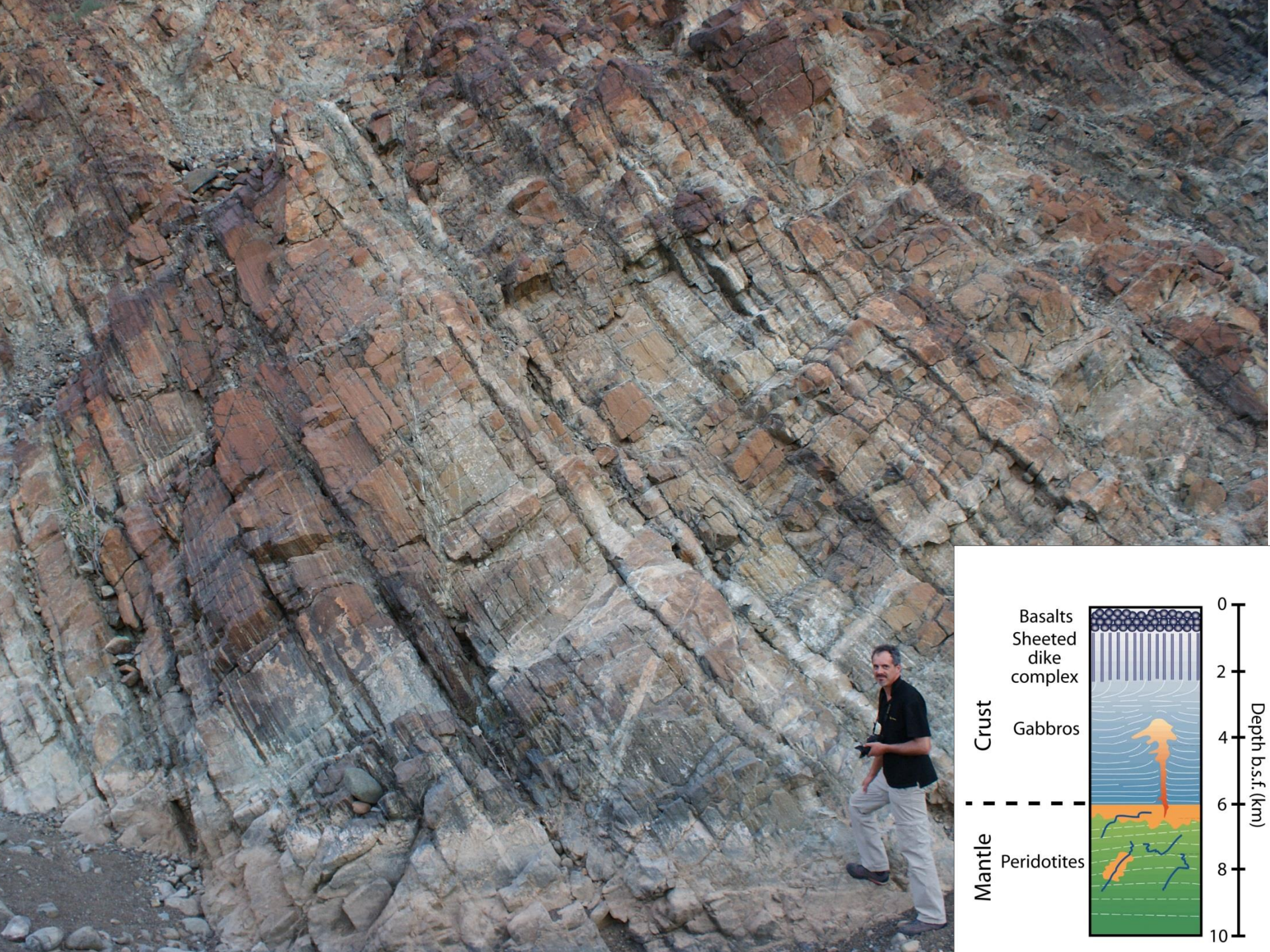
Basalts
Sheeted dike complex
Gabbros
Peridotites
Crust
Mantle
0
2
4
6
8
10
Depth b.s.f. (km)

Boudier 1996

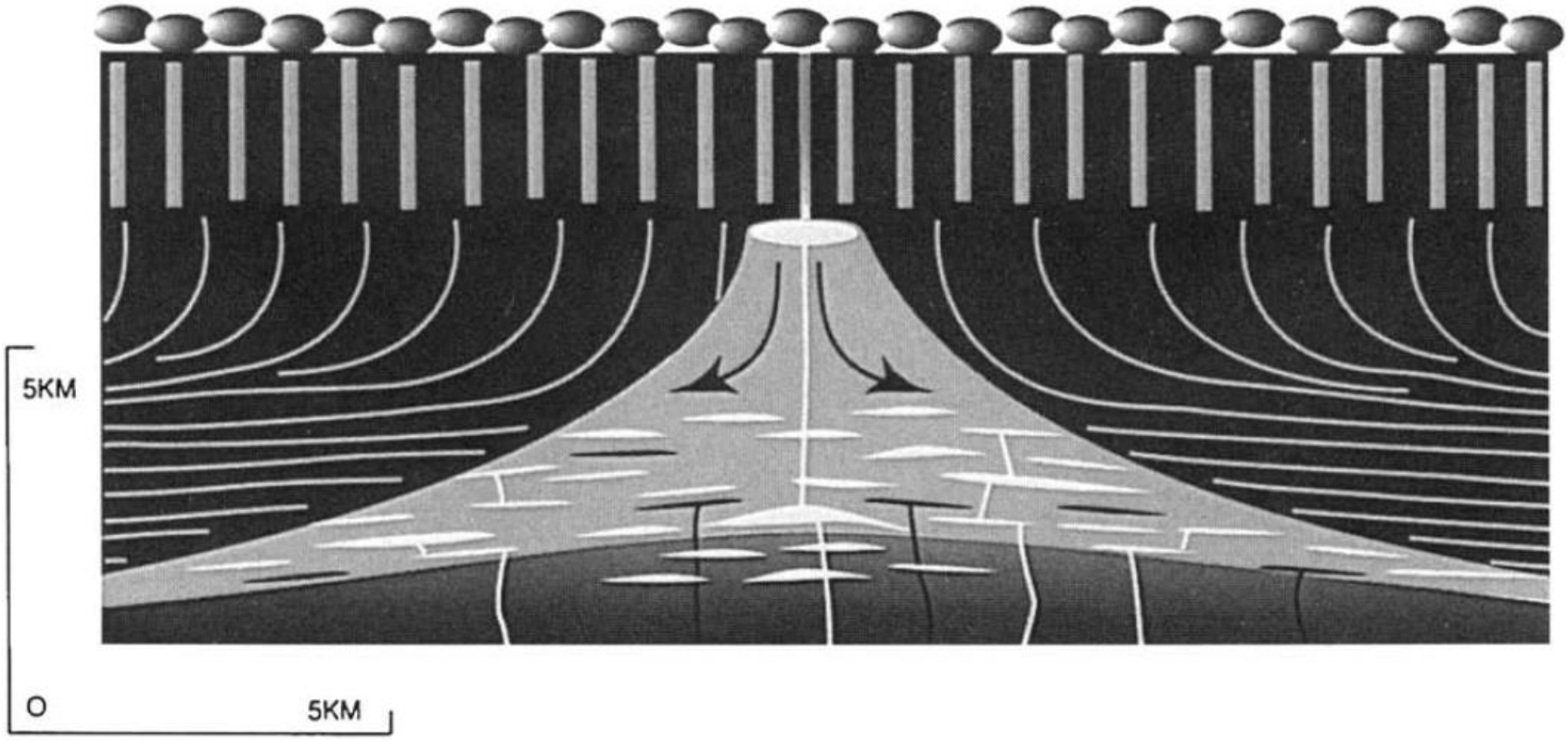

Fig. 7. Dual feeding model for magma chamber model (see text for further discussion).

Kelemen Koga Shimizu 1997 EPSL

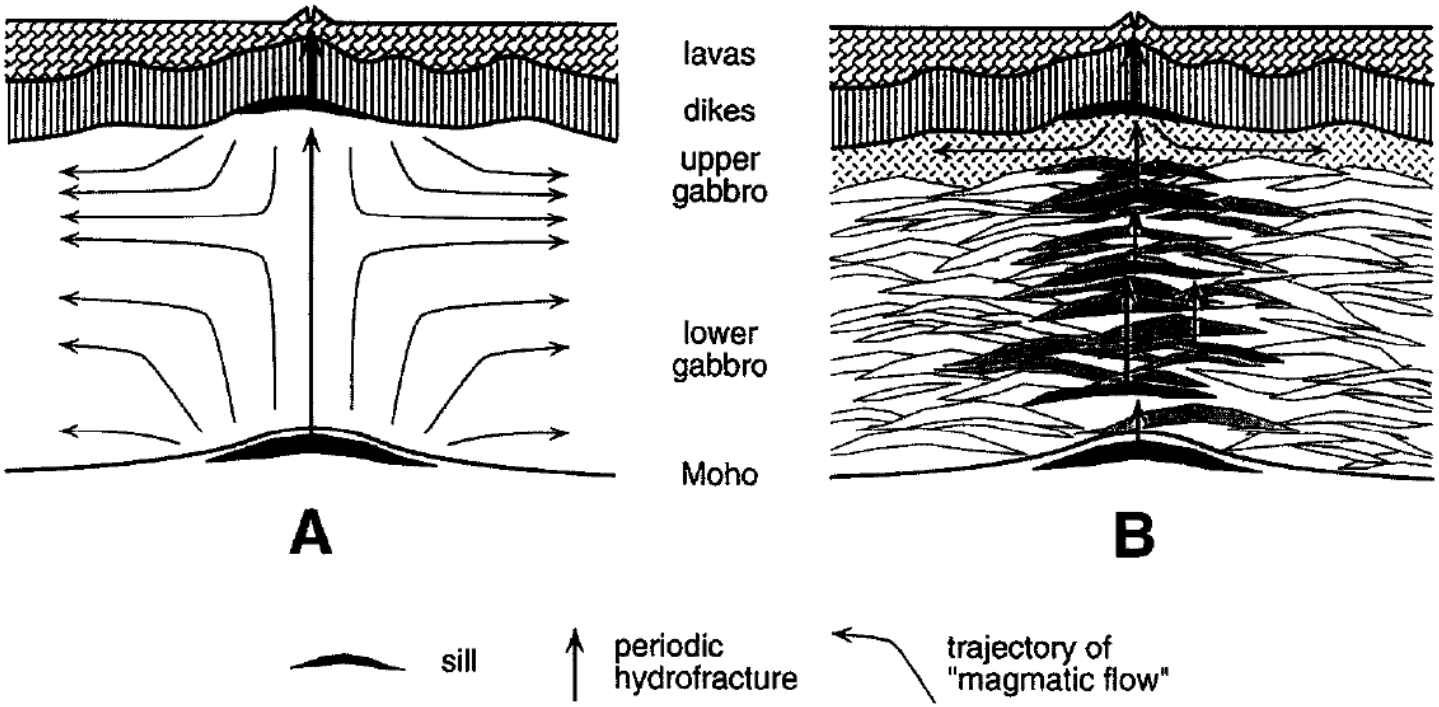

Fig. 6. Schematic illustrations of the role of deep crustal sills in forming lower gabbros in beneath oceanic spreading ridges. (A) More than 90% of the lower crust crystallizes in two sills, one near the MTZ, and the other just below the base of the sheeted dikes. Flow of largely crystalline ''mush'' from the two sills forms the gabbroic lower crust, as modeled kinematically by [75]. Periodic hydrofracture carries evolved liquids out of the lower sill, leaving ''cumulate'' gabbros. Lower gabbros might be expected to be compositionally uniform in this scenario. (B) Lower gabbros form in ''sheeted sills'' that are emplaced and crystallize near their final depth within the crust. In this case, although chemical variation with height above the Moho will be irregular, there should be a general trend toward more evolved compositions upsection, throughout the lower gabbros. Currently available data are insufficient to distinguish between these two possibilities.

Data: Nicolle et al. EPSL 2016
Takazawa et al. G3 2003
Godard et al. G3 2003

	La	*Ce*	*Nd*	*Sm*	*Eu*	*Dy*	*Er*	*Yb*	*Lu*
Harzburgite Cpx	0.002	0.004	0.033	0.138	0.073	1.250	1.030	0.958	0.147
Harzburgite Cpx	0.001	0.005	0.013	0.043	0.033	0.749	0.687	0.727	0.111
Dunite Cpx (Mg#0.92; M.75)	0.096	0.498	0.880	0.450	0.180	1.010	0.720	0.740	0.100
Dunite Cpx (Mg#0.92; M.75)	0.080	0.400	0.750	0.390	0.150	0.820	0.610	0.650	0.090
Chondrite	0.237	0.613	0.457	0.148	0.056	0.246	0.160	0.161	0.025
Kd Conditions manteau									
Cpx/Melt	0.0536	0.0858	0.1873	0.29	0.3	0.38	0.425	0.45	0.433
Kd crystallisation									
Ol / Melt	0.0004	0.0005	0.001	0.0013	0.0016	0.0017	0.0015	0.0015	0.0015
Cpx / Melt	0.054	0.098	0.21	0.26	0.31	0.33	0.3	0.28	0.28
Plsg / Melt	0.27	0.2	0.14	0.11	0.73	0.055	0.041	0.031	0.025
frac: CL/C0=F^(D-1)									
MORB (XMg=0.5)	5.21	14.86	12.03	3.82	1.36	6.08	3.79	3.63	0.53
Lave V1 (XMg~0.3)	4.3	13.52	12.24	4.03	1.58	7.22	4.34	4.12	0.65
Lave V1 (XMg~0.3)	4.57	13.85	12	3.8	1.42	6.65	4.13	4.05	0.63
Lave V1 (XMg~0.3)	3.15	9.99	9.33	3.08	1.22	5.76	3.55	3.37	0.54
Lave V1 (XMg~0.3)	6.29	19.68	16.8	5.38	1.83	9.02	5.66	5.49	0.9
Lave V1 (XMg~0.3)	5.23	15.45	13.82	4.35	1.59	7.47	4.63	4.37	0.72
Lave V1 (XMg~0.3)	4.61	13.35	11.42	3.53	1.26	6.03	3.64	3.56	0.58

Kelemen, 1995, Nature

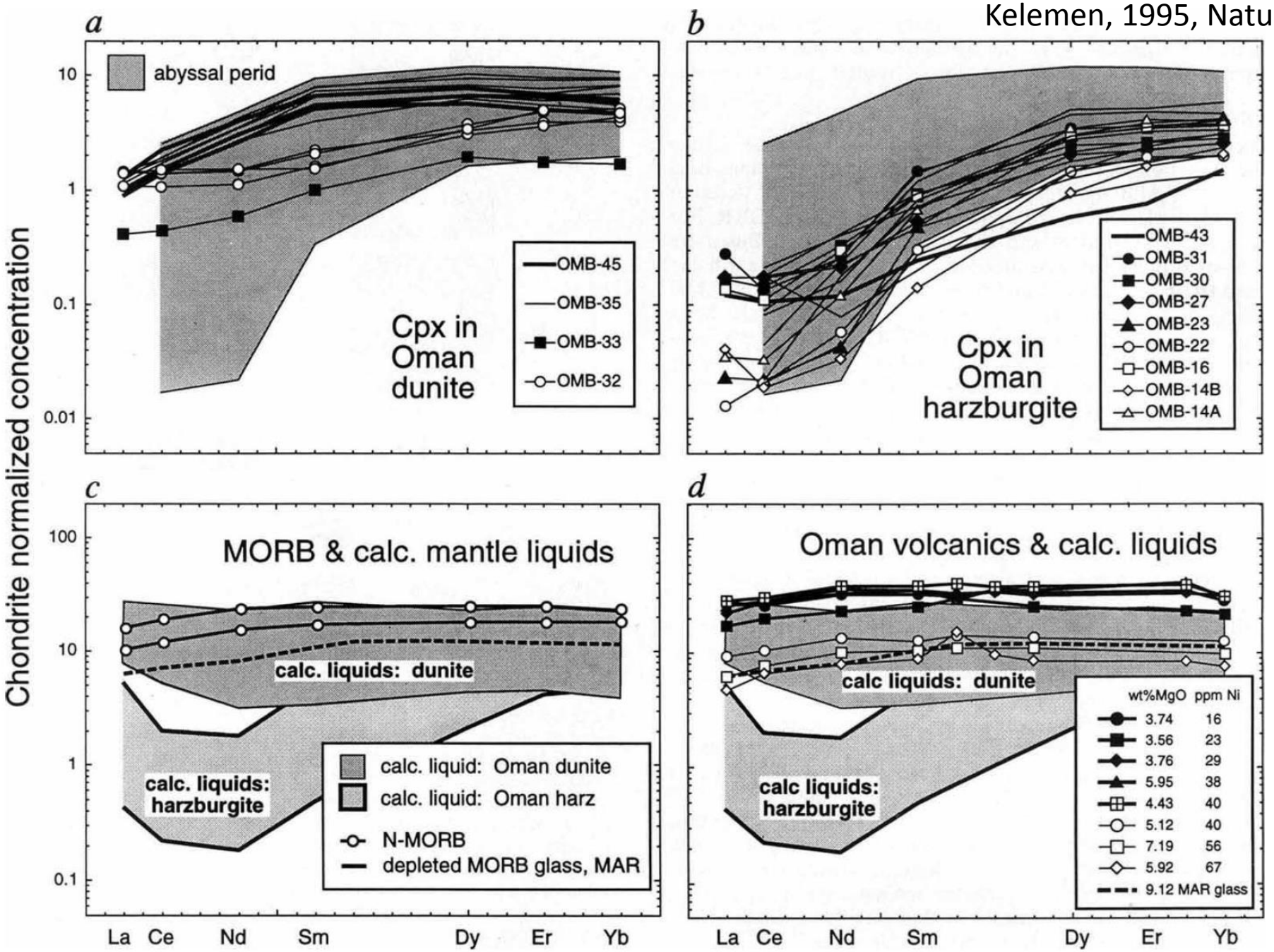

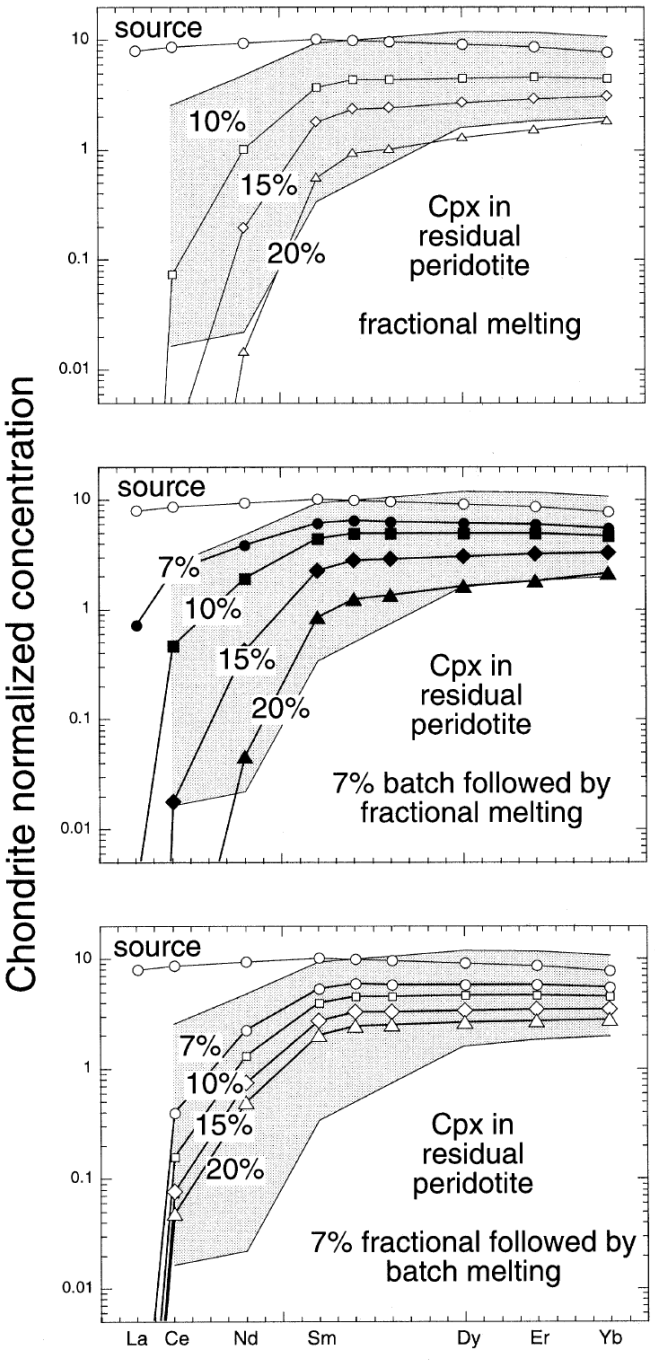

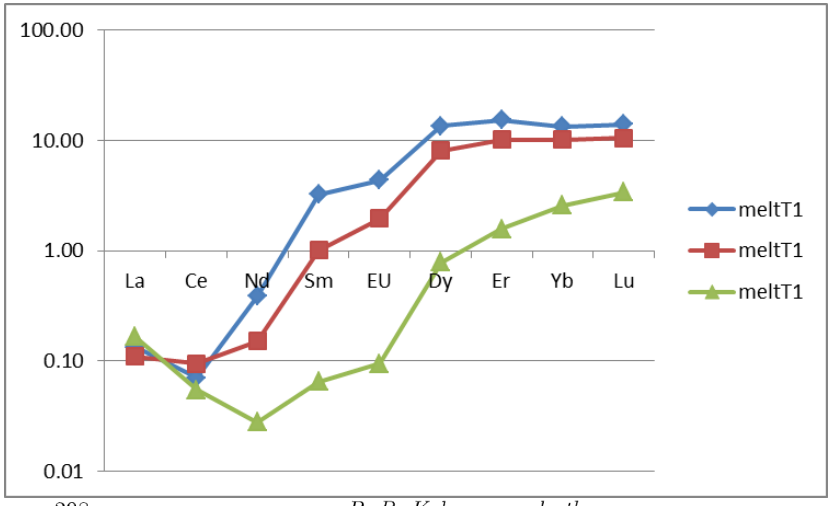

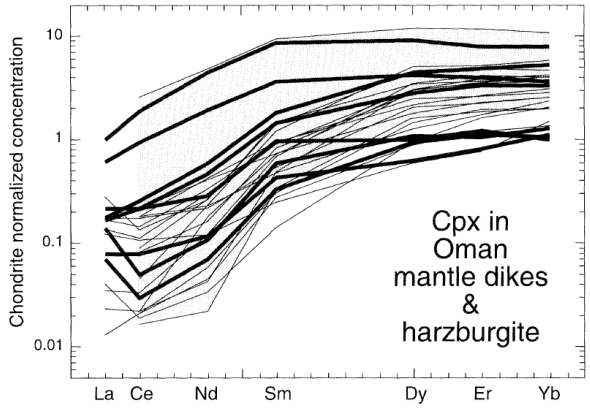

Figure 8. REE contents of Cpx in gabbronorite and websterite dikes from the Wadi Tayin massif of the Oman (bold lines), compared to Cpx in harzburgite from the same massif (light lines) and in abyssal peridotite (shaded field). Six of eight dikes analysed had Cpx REE contents different from Cpx in equilibrium with MORB, and very similar to Cpx in residual peridotites, suggesting that the dikes are formed by crystal fractionation from liquids derived by low pressure partial melting of highly depleted peridotite. Data for dikes from Farrier *et al.* (1997), for Oman peridotite from Kelemen *et al.* (1995*b*), and for abyssal peridotite from Johnson *et al.* (1990) and Johnson & Dick (1992).

Figure 2. Calculated REE in clinopyroxene (Cpx) in residues of partial melting of mantle peridotite in spinel lherzolite facies, with various different combinations of batch and fractional melting. Grey shaded area illustrates the range of REE in Cpx in abyssal peridotites (Johnson *et al.* 1990; Johnson & Dick 1992). No unique combination of batch and fractional melting processes is required to account for the abyssal peridotite data. However, an interval of near-fractional melting, on the order of 3 wt%, is required to produce large light/heavy REE fractionation. Calculations used the methods of Gast (1968) and Shaw (1970), melt and source modes from Kelemen *et al.* (1992), partition coefficients compiled by Kelemen *et al.* (1993), and initial peridotite composition from Shimizu (1997), with Yb = 2× chondritic concentration.

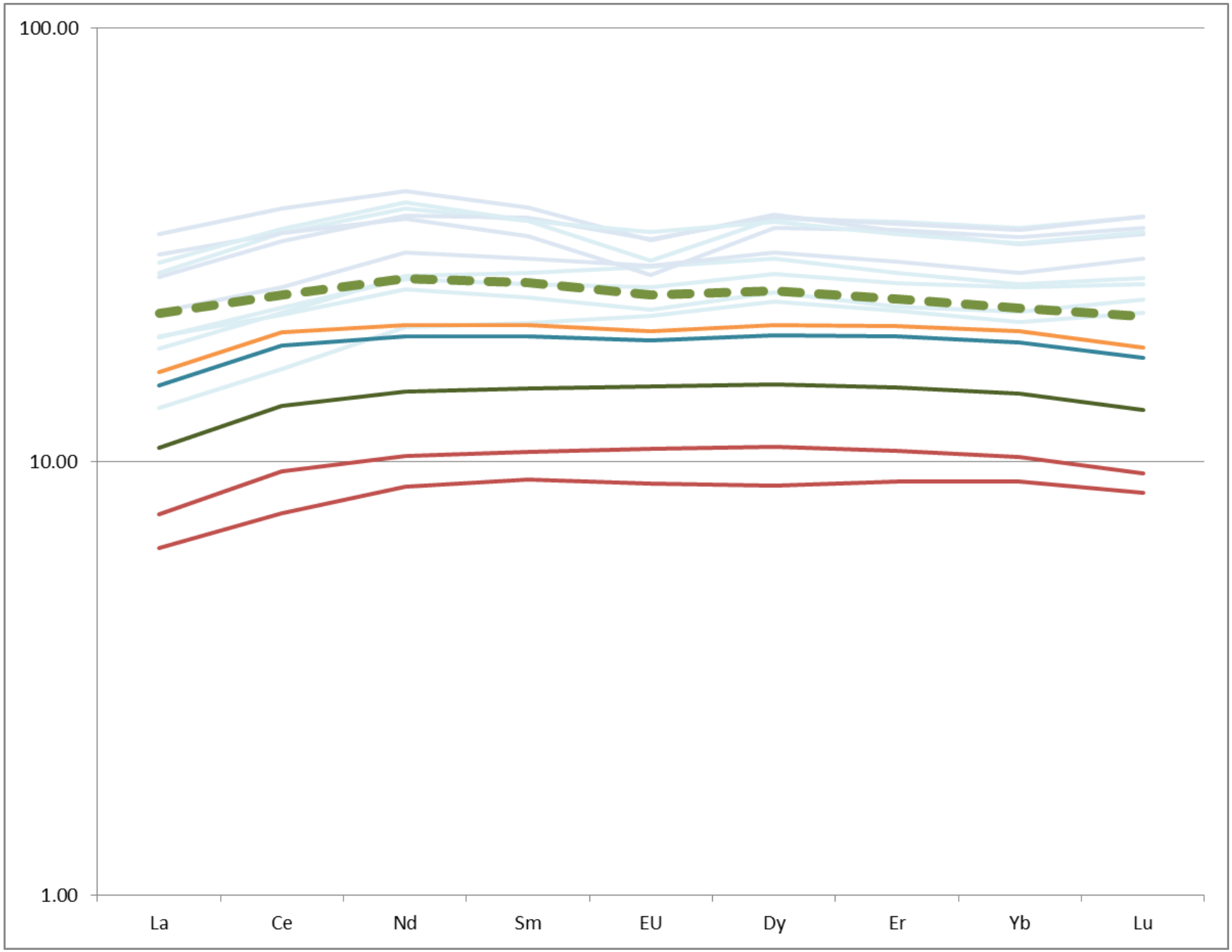
100.00
10.00
1.00
La
Ce
Nd
Sm
EU
Dy
Er
Yb
Lu